Theoretical Investigation of the Decay Processes in Photo-excited Organic Dye Molecules

（有機色素分子の光励起の減衰過程に関する理論的研究）

Naoto Inai

2022.03

Contents

Chapter 1

General Introduction

The use of photochemistry of organic dye molecules has covered a wide range of applications. For example, the energy of photon absorbed can be used for intramolecular reaction of the dye molecules, such as the *cis-trans* isomerization of cinnamate derivatives for UV protection,[1–5] or cyclization/cycloreversion reactions of diarylethenes as photochromic molecules.[6,7] The absorbed energy can also be retained to emit light as fluorescence or phosphorescence. In recent years, the imaging techniques using fluorescence of organic dye molecules have become a powerful tool for visualizing biosystems.[8–12] In other fields, organic molecules with thermally activated delayed fluorescence (TADF) have been extensively studied for their potential use in organic light-emitting diodes (OLEDs) with high electroluminescence efficiency.[13–15] On the other hand, the absorbed energy can be used for catalyzing other reactions.[16–18] These various applications indicate that the use of photochemistry of organic dye molecules is indispensable for our life.

This variety of applications is originated from various usages of the absorbed energy. In usual organic molecules, dipole-allowed fluorescent decay occurs with the lifetime of several nanoseconds.[8] When the absorbed energy is used for intramolecular reaction, it usually proceeds faster than fluorescent decay. For example, photo-excited cinnamate derivatives decays, reaching its electronic ground state within several picoseconds,[19,20] and the photo-induced diarylethenes in its closed form do within tens-of-picoseconds.[7,21] On the other hand, organic photocatalysts usually reach a triplet state rather than causing fluorescent decay.[16,22] As the typical lifetime of triplet states is long enough to encounter reactants, the photocatalytic reaction occurs via triplet state-assisted channels. Considering the difference in the process after photoabsorption, one can say that the application of the organic dye molecules should be controlled by the rate constant of electronic transitions after photoabsorption.

From this context, theoretical estimation of the rate constants for electronic transitions in organic molecules have attracted growing attention toward theory-based molecular design. The possible methods to estimate rate constants are the nonadiabatic molecular dynamics simulations,[23–25] perturbative methods like Fermi's golden rule[26–36] or Marcus theory,[37] or application of Eyring's equation[38] to the activation energy at the excited state. Of these methods, the nonadiabatic dynamics simulations have been applied mainly to the ultrafast decays, such as the cycloreversion of cyclohexatriene,[39–41] *cis-trans* isomerization of azoben-

zenes,[42–44] partially because longer lifetime requires a larger computational cost. Hence, for the relatively slow decays, the perturbative approach has been applied in recent years. Wu et al. employed this method for theoretically designing a pH-responsive organic photocatalyst for polymerization.[45] Several studies have investigated the rate constant of reverse intersystem crossing (rISC) in TADF molecules to gain some insight for accelerating the rISC process.[46–50] This perturbative method to estimate rate constants has been becoming a tool for theory-based molecular design.

However, the accessibility to computer programs for estimating rate constant is still limited. Wu et al. employed MOMAP program[28] in their study. I also have ever used this program;[51] at that time, I found that it was short of some methods. Neese et al. implemented these computational methods to their quantum chemistry calculation package ORCA.[52,53] Several studies have investigated the rate constant of reverse intersystem crossing (rISC) in TADF molecules to gain some insight for accelerating the rISC process using their in-house codes.[49,50,54] Except for the FCClasses by Santoro et al.[55] in its β version, program codes with its source code accessible are not publically available. In order for me to conduct these calculations, access to the further feasible program code is desirable.

Another problem in the perturbative method is that the necessity of applying harmonic approximation to potential energy surfaces to compute the overlap of vibrational wavefunction makes it impossible to study anharmonic events under this method.[29] One of the important anharmonic events is the thermally activated decay through conical intersection.[56–58] Decay through a conical intersection can be seen among several organic dye molecules, such as stilbene[59] and nucleic acids.[60,61] Assuming that the nonadiabatic transition at the conical intersection is not a rate-determining step and that the whole decay process is much slower than vibrational redistribution, the rate constant of the decay is considered to be controlled by activation energy.[56–58] In such a case, the rate constant of the decay should be estimated using Eyring's equation. Some studies employed Kramers' barrier-crossing theory instead of Eyring's equation.[58,62] Using these methods, the rate constant of electronic transition can be theoretically estimated.

In the theoretical estimation of the rate constants, the accuracy of the quantum mechanical calculation can be an important matter. According to the energy gap law, the rate constant of radiationless electronic transition in the rigid molecule is proportional to the exponential of the energy gap.[33,63] The rate constant in Eyring's equation is also proportional to the exponential of the activation energy.[38] This sensitivity of the rate constants to relative energy indicates that the use of highly accurate quantum mechanical calculation methods is highly recommended for reasonably estimating the rate constants. Actually, Marian et al. have employed a combination of density functional theory and multireference configuration interaction (DFT/MRCI methods) to reliably estimate the relative energy.[30–33,64] Kim et al. employed spin component scaled variant[65] of the second-order algebraic diagrammatic construction method[66] (SCS-ADC(2)) to reliably estimate the geometry and Hessian.[49,50] If possible, the use of functional-free wavefunction theories is desirable to obtain reliable computational results.

In recent years, the applicability of the several high-level wavefunction theory has been extended thanks to the development of efficient approximations and the release of publically available programs. Neese et al. have developed an efficient approximation for handling electron correlation, known as domain-based local pair natural orbital-based (DLPNO-) approaches, and implemented them into their ORCA program package.[53,67–70] In the framework of these methods, the energy of the medium size of molecules may be reasonably estimated at the usual geometry. However, computation at the specific geometry can be out of range of the applicability of these single reference methods; at such geometry, so-called multireference (MR) methods[71–81] may properly work. The multireference methods have also been extended by the introduction of the density matrix renormalization group (DMRG) algorithm. Chan and Yanai et al. have introduced DMRG to extend the size of applicable molecule.[82–86] As well as the extension to a large system, the analytical nuclear derivative at the MR level of theory has been developed and implemented,[77,87–93] which enables the optimization of molecular geometry at the MR level of theory. These recent techniques indicate that the infrastructure of the methods to reasonably estimate the energy of molecules is being constructed.

In my three years, I tried to theoretically estimate the rate constant of electronic transition in the excited organic dye molecules using both Eyring's equation and perturbative approach. In validating the application of Eyring's equation to estimate a rate constant, I chose silepin molecules as a subject of research. The silepin molecules are *cis*-stilbene derivatives bridged by $SiMe_2$ moiety as they have a 7-membered ring. The radiative and nonradiative decay rate constants were experimentally obtained;[94] however, the mechanism of the nonradiative decay was unknown. By assuming that the decay process is the thermally activated decay triggered by the twisting of the central C=C bond, I tried to compute the rate constants by applying Eyring's equation,[95] which is given in Chapter 3. In the study, the use of multireference theory for the evaluation of geometry as well as energy was critical to obtain reasonable activation energy. The findings obtained in this study were useful in the collaborative research with Dr. Okuno and Mr. Nomoto.[96]

Motivated by the collaborative research with Yamaguchi group[51] and the discussions with Dr. Okuno, who is my double-mentor in the GTR program, I wrote a Python code for computing the rate constants using perturbative approach; the code was mainly derived from FCClasses in the β version which was kindly provided by Prof. Santoro. For handling weakly allowed transitions in radiative decay and intersystem crossing, the 1st-order derivative of the couplings are also treated (so-called Herzberg-Teller (HT) approximation); using this method, rate constants of a characteristic TADF molecule (DABNA)[14] was estimated and compared with the experimentally obtained value and theoretical one in a previous study.[50] There, a reliable prediction of the relative energies as well as the treatment of the spin-orbit coupling matrix elements (SOCMEs) at a higher level than the constant model (Franck–Condon level) were required for a reasonable estimation of the rate constant. Thanks to my Python code, I got to compute the rate constants using an editable program. This code will be potentially used to estimate rate constants with coupling terms estimated at higher-

level quantum mechanical methods under the development in Yanai group. The theories, validation of my code, and application to DABNA are given in Chapter 2.

Using my code, I investigated the nonradiative decays of the bis-phosphanyl-bridged stilbene analogues. Yamaguchi et al. synthesized the bis-phosphanyl-bridged stilbene and its dioxide (bis-phosphoyyl-bridged stilbene) in 2008,[97] where the oxidation turned out to increase the fluorescence quantum yield (Φ_{F}). When they synthesized the thiophene-fused phospholo[3,2-b]phosphole and its dichalcogenides, which are the thiophene-fused analogue of bis-phosphanyl-bridged stilbenes, in 2010,[98] it turned out to be that the oxygenation of thiophene-fused phospholo[3,2-b]phosphole drastically reduced its Φ_{F}. To theoretically gain insight into the changes in Φ_{F}, I computed the rate constants of the transitions from the first excited state of these molecules; there, the perturbative method and conical intersection search were both necessary. The study of these P-bridged stilbene analogues is given in Chapter 4.

The rest of this thesis is composed of 4 other chapters. The theories employed in this study and implementation of the rate constant calculations are provided in Chapter 2, where some computations to be compared with the FCClasses codes and application to DABNA are also provided. Theoretical investigation of the nonradiative decay of silepin molecules is shown in Chapter 3. Investigation of the effect of the phosphorus oxigenation in the bis-phosphanyl-stilbene analogues on nonradiative decays is provided in Chapter 4. Concluding remarks are given in Chapter 5. After that, other publications are included.

Bibliography

[1] A. Gunia-Krzyżak et al., Int. J. Cosmet. Sci. **40**, 356 (2018).

[2] J. Kockler, M. Oelgemöller, S. Robertson, and B. D. Glass, J. Photochem. Photobiol. C Photochem. Rev. **13**, 91 (2012).

[3] L. A. Baker et al., J. Phys. Chem. Lett. **7**, 56 (2016).

[4] M. Promkatkaew et al., Photochem. Photobiol. Sci. **13**, 583 (2014).

[5] J. Luo et al., J. Phys. Chem. Lett. **8**, 1025 (2017).

[6] M. Irie, Chem. Rev. **100**, 1685 (2000).

[7] M. Irie, T. Fukaminato, K. Matsuda, and S. Kobatake, Chem. Rev. **114**, 12174 (2014).

[8] J. R. Lakowicz, *Principles of fluorescence spectroscopy*, Springer science & business media, third edition, 2013.

[9] T. Terai and T. Nagano, Pflügers Archiv-European Journal of Physiology **465**, 347 (2013).

[10] J. Chan, S. C. Dodani, and C. J. Chang, Nat. Chem. **4**, 973 (2012).

[11] Y. Tsuchiya et al., Science **349**, 864 (2015).

[12] C. Wang et al., Angew. Chem. Int. Ed. **127**, 15428 (2015).

[13] H. Uoyama, K. Goushi, K. Shizu, H. Nomura, and C. Adachi, Nature **492**, 234 (2012).

[14] T. Hatakeyama et al., Adv. Mater. **28**, 2777 (2016).

[15] Y. Kondo et al., Nat. Photonics **13**, 678 (2019).

[16] J. C. Theriot et al., Science **352**, 1082 (2016).
[17] Y. Lee and M. S. Kwon, Eur. J. Org. Chem. **2020**, 6028 (2020).
[18] D. Liu et al., Org. Lett. **20**, 5700 (2018).
[19] Y. Peperstraete et al., Phys. Chem. Chem. Phys. **18**, 28140 (2016).
[20] J. M. Woolley et al., Phys. Chem. Chem. Phys. **21**, 14350 (2019).
[21] H. Sotome et al., J. Am. Chem. Soc. **139**, 17159 (2017).
[22] N. A. Romero and D. A. Nicewicz, Chem. Rev. **116**, 10075 (2016).
[23] J. C. Tully, J. Chem. Phys. **93**, 1061 (1990).
[24] D. B. Lingerfelt, D. B. Williams-Young, A. Petrone, and X. Li, J. Chem. Theory Comput. **12**, 935 (2016).
[25] J. W. Park and T. Shiozaki, J. Chem. Theory Comput. **13**, 3676 (2017).
[26] Y. Niu, Q. Peng, C. Deng, X. Gao, and Z. Shuai, J. Phys. Chem. A **114**, 7817 (2010).
[27] Q. Peng, Y. Niu, Q. Shi, X. Gao, and Z. Shuai, J. Chem. Theory Comput. **9**, 1132 (2013).
[28] Y. Niu et al., Mol. Phys. **116**, 1078 (2018).
[29] A. Humeniuk et al., J. Chem. Phys. **152**, 054107 (2020).
[30] M. Etinski, J. Tatchen, and C. M. Marian, J. Chem. Phys. **134**, 154105 (2011).
[31] M. Etinski, V. Rai-Constapel, and C. M. Marian, J. Chem. Phys. **140**, 114104 (2014).
[32] J. Tatchen, N. Gilka, and C. M. Marian, Phys. Chem. Chem. Phys. **9**, 5209 (2007).
[33] T. J. Penfold, E. Gindensperger, C. Daniel, and C. M. Marian, Chem. Rev. **118**, 6975 (2018).
[34] V. Lawetz, G. Orlandi, and W. Siebrand, J. Chem. Phys. **56**, 4058 (1972).
[35] R. Valiev, V. Cherepanov, G. V. Baryshnikov, and D. Sundholm, Phys. Chem. Chem. Phys. **20**, 6121 (2018).
[36] R. R. Valiev, V. N. Cherepanov, R. T. Nasibullin, D. Sundholm, and T. Kurten, Phys. Chem. Chem. Phys. **21**, 18495 (2019).
[37] N. Aizawa, Y. Harabuchi, S. Maeda, and Y.-J. Pu, Nat. Commun. **11**, 1 (2020).
[38] H. Eyring, J. Chem. Phys. **3**, 107 (1935).
[39] A. Ohta, O. Kobayashi, S. O. Danielache, and S. Nanbu, Chem. Phys. **459**, 45 (2015).
[40] A. Ohta, O. Kobayashi, S. O. Danielache, and S. Nanbu, Chem. Phys. **485**, 45 (2017).
[41] I. Polyak, L. Hutton, R. Crespo-Otero, M. Barbatti, and P. J. Knowles, J. Chem. Theory Comput. **15**, 3929 (2019).
[42] A.-H. Gao, B. Li, P.-Y. Zhang, and K.-L. Han, J. Chem. Phys. **137**, 204305 (2012).
[43] L. Liu, Y. Wang, and Q. Fang, J. Chem. Phys. **146**, 064308 (2017).
[44] R. Liang, J. Chem. Theory Comput. **17**, 3019 (2021).
[45] C. Wu et al., J. Am. Chem. Soc. **141**, 8207 (2019).
[46] J. Gibson, A. P. Monkman, and T. J. Penfold, ChemPhysChem **17**, 2956 (2016).
[47] T. Northey and T. Penfold, Org. Electron. **59**, 45 (2018).
[48] L. Lv, K. Yuan, T. Zhao, and Y. Wang, J. Mater. Chem. C **8**, 10369 (2020).
[49] I. Kim et al., J. Chem. Theory Comput. **16**, 621 (2020).
[50] I. Kim et al., JACS Au **1**, 987 (2021).

[51] Y. Sugihara et al., Chem. Sci. **12**, 6333 (2021).
[52] B. de Souza, F. Neese, and R. Izsák, J. Chem. Phys. **148**, 034104 (2018).
[53] F. Neese, F. Wennmohs, U. Becker, and C. Riplinger, J. Chem. Phys. **152**, 224108 (2020).
[54] S. Lin, Z. Pei, B. Zhang, H. Ma, and W. Liang, J. Phys. Chem. A **126**, 239 (2022).
[55] *FCclasses 3.0 beta release*, http://www.pi.iccom.cnr.it/fcclasses.
[56] Y. Harabuchi, T. Taketsugu, and S. Maeda, Phys. Chem. Chem. Phys. **17**, 22561 (2015).
[57] Y. Harabuchi, T. Taketsugu, and S. Maeda, Chem. Lett. **45**, 940 (2016).
[58] J. Hoche et al., Chem. Sci. **10**, 11013 (2019).
[59] I. N. Ioffe and A. A. Granovsky, J. Chem. Theory Comput. **9**, 4973 (2013).
[60] C. E. Crespo-Hernández, B. Cohen, P. M. Hare, and B. Kohler, Chem Rev **104**, 1977 (2004).
[61] S. Yamazaki and T. Taketsugu, J. Phys. Chem. A **116**, 491 (2012).
[62] T. S. Blacker, R. J. Marsh, M. R. Duchen, and A. J. Bain, Chem. Phys. **422**, 184 (2013).
[63] J. Shi et al., Org. Chem. Front. **6**, 1948 (2019).
[64] A. Rodriguez-Serrano, F. Dinkelbach, and C. M. Marian, Phys. Chem. Chem. Phys. **23**, 3668 (2021).
[65] S. Grimme, J. Chem. Phys. **118**, 9095 (2003).
[66] J. Schirmer, Physical Review A **26**, 2395 (1982).
[67] P. Pinski and F. Neese, J. Chem. Phys. **150**, 164102 (2019).
[68] C. Riplinger and F. Neese, J. Chem. Phys. **138**, 034106 (2013).
[69] M. Saitow, U. Becker, C. Riplinger, E. F. Valeev, and F. Neese, J. Chem. Phys. **146**, 164105 (2017).
[70] R. Izsák, Int. J. Quantum Chem. **121**, e26327 (2021).
[71] B. O. Roos et al., Chem. Phys. **48**, 157 (1980).
[72] K. Andersson, P.-Å. Malmqvist, and B. O. Roos, J. Chem. Phys. **96**, 1218 (1992).
[73] J. Finley, P.-Å. Malmqvist, B. O. Roos, and L. Serrano-Andrés, Chem. Phys. Lett. **288**, 299 (1998).
[74] K. Hirao, Chem. Phys. Lett. **190**, 374 (1992).
[75] H. Nakano, J. Chem. Phys. **99**, 7983 (1993).
[76] A. A. Granovsky, J. Chem. Phys. **134**, 214113 (2011).
[77] T. Shiozaki, W. Győrffy, P. Celani, and H.-J. Werner, J. Chem. Phys. **135**, 081106 (2011).
[78] C. Angeli, R. Cimiraglia, S. Evangelisti, T. Leininger, and J.-P. Malrieu, J. Chem. Phys. **114**, 10252 (2001).
[79] C. Angeli, R. Cimiraglia, and J.-P. Malrieu, Chem. Phys. Lett. **350**, 297 (2001).
[80] C. Angeli, R. Cimiraglia, and J.-P. Malrieu, J. Chem. Phys. **117**, 9138 (2002).
[81] C. Angeli, S. Borini, M. Cestari, and R. Cimiraglia, J. Chem. Phys. **121**, 4043 (2004).
[82] D. Ghosh, J. Hachmann, T. Yanai, and G. K.-L. Chan, J. Chem. Phys. **128**, 144117 (2008).
[83] T. Yanai, Y. Kurashige, D. Ghosh, and G. K.-L. Chan, Int. J. Quantum Chem. **109**,

2178 (2009).

[84] S. Guo, M. A. Watson, W. Hu, Q. Sun, and G. K.-L. Chan, J. Chem. Theory Comput. **12**, 1583 (2016).

[85] Y. Kurashige and T. Yanai, J. Chem. Phys. **135**, 094104 (2011).

[86] T. Yanai et al., J. Chem. Theory Comput. **13**, 4829 (2017).

[87] B. Vlaisavljevich and T. Shiozaki, J. Chem. Theory Comput. **12**, 3781 (2016).

[88] T. Shiozaki, WIREs Comput. Mol. Sci. **8**, e1331 (2018).

[89] J. W. Park, R. Al-Saadon, N. E. Strand, and T. Shiozaki, J. Chem. Theory Comput. **15**, 4088 (2019).

[90] J. W. Park, J. Chem. Theory Comput. **15**, 5417 (2019).

[91] J. W. Park, J. Chem. Theory Comput. **16**, 326 (2020).

[92] J. W. Park, J. Chem. Theory Comput. **17**, 6122 (2021).

[93] Y. Nishimoto, J. Chem. Phys. **151**, 114103 (2019).

[94] L. G. Mercier et al., Organometallics **30**, 1719 (2011).

[95] N. Inai, D. Yokogawa, and T. Yanai, J. Phys. Chem. A **125**, 559 (2021).

[96] A. Nomoto, N. Inai, T. Yanai, and Y. Okuno, J. Phys. Chem. A, *in press*.

[97] A. Fukazawa et al., Org. Lett. **10**, 913 (2008).

[98] A. Fukazawa, T. Murai, L. Li, Y. Chen, and S. Yamaguchi, C. R. Chim. **13**, 1082 (2010).

Chapter 2

Theoretical Background

2.1 Overview

In this chapter, some of the methods employed in this thesis are summarized: 1. The multireference quasi-degenerate perturbation theory (MR-QDPT), 2. The method to optimize the molecular geometry on the intersection space of adiabatic potential energy surfaces (PESs), 3. The method to compute the rate constant of vibronic transition. The main theme of this thesis is related to how the photo-excited organic dye molecules lose their energy. To handle the complicated electronic structure of the photo-excited organic molecules, MR-QDPT methods,[1–4] which can effectively expand the complicated electronic state by including all configurations in the important orbitals, were employed. For understanding the decay of photo-excited molecules, both radiative and nonradiative decays should be considered. The nonradiative decays consist of the decay at the intersection of PESs and the one between vibronic states. For the computation of the former ones, geometry optimization on the intersection seam between PESs is an effective approach, while a perturbative approach like Fermi's golden rule is effective to the latter ones. In this study, MR-QDPT level calculations and geometry optimization on the intersection space were conducted using existing programs,[2,5] while rate constant calculations based on perturbation theory were conducted using the program that I coded. In coding my program, modules for handling internal coordinate of molecular geometry were adopted from Psi4 program,[6] and several parts are coded based on β version of FCClasses 3.0 by Santoro et al.[7] Some computed results were compared with results produced using MOMAP by Shuai et al.[8] and DUSHIN by Reimers.[9] In coding, Python 3 was employed, and numerical operations such as matrix operation and Fourier transformation are conducted by Numpy module.[10] In the last, several calculations were conducted to validate my code. First, the data computed by my code is compared with that by FCClasses to verify that I successfully implemented these theories; there, some analysis of the computed results is provided. Then, the rate constants of the reverse intersystem crossing (rISC) in a characteristic MR-TADF molecule were computed.

2.2 Multireference quasi-degenerate perturbation theory (MR-QDPT)

2.2.1 Complete-active-space self-consistent-field (CASSCF) method

The complete-active-space self-consistent-field (CASSCF) method is a method to obtain a wavefunction better than the Hartree-Fock (HF) approximation. The HF theory[11,12] is one of the basic theories in quantum chemistry. There, the ground state wavefunction is approximated by a ground state electronic configuration. The HF approximation is considered to cover almost 99% of the total energy; however, the residual part, called the electron correlation, is often important in the chemical discussion.

The electron correlation can be handled by including the electrically excited configurations to expand the wavefunction. If all of the configurations were included, known as the full-configuration interaction (Full-CI) method, the exact electronic energy would be obtained. In practice, only a fraction of the configurations is included to save the computational cost. Because only a fraction of the configurations is included, the quality of the HF reference becomes important.

When the quality of the HF wavefunction is reasonable, the single-reference methods such as the configuration interaction including all single and double excitations (CISD)[13] and the coupled-cluster method with the singles and doubles (CCSD)[14] can reasonably include the electronic correlation using the HF solution as a reference state. On the other hand, when the electronic state has any possible degeneracy, the quality of the HF reference becomes questionable. In such cases, the reference wavefunction should be re-constructed by including some of the other configurations.

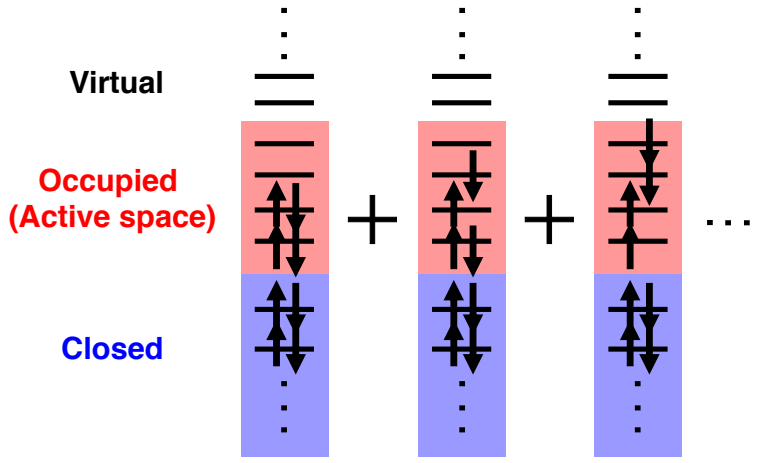

Fig. 2.1: A schematic figure of the expansion of wavefunction in the CASSCF method

A popular method to handle the electronic state with possible degeneracy is the CASSCF method.[15] In the CASSCF method, molecular orbitals are separated into three classes as shown in Fig. 2.1. The first one contains the closed orbitals, which are kept doubly occupied

during CASSCF calculation. The second one contains the occupied orbitals, whose occupation number is between 0 to 2; this class is also called the active space. The last one contains the virtual orbitals, which are unoccupied during the CASSCF calculation. The CASSCF calculation is composed of the Full-CI step in the active space (CAS-CI) and orbital optimization step (SCF). Originally, these steps were conducted at the same time (1-step algorithm). On the other hand, the programs I employed, such as ORZ and QSimulate-QM,[16] compute these steps separately (two-step algorithm).[17]

CAS-CI part is the diagonalization of the active space Hamiltonian. Because the CAS-CI part is the Full-CI calculation in the active space, the order of the computational cost is factorial to the size of the active space employed. Usually, an active space where 14 electrons in 14 orbitals is located near the upper limit of the application. SCF part is the optimization of the molecular orbitals to minimize the energy of the electronic state given by the CAS-CI part. The optimization of the molecular orbitals is expressed by the unitary transformation of the MO coeficient matrix as,[17]

$$\mathbf{C}^{\mathrm{new}} = \mathbf{C}^{\mathrm{old}}\mathbf{U}. \tag{2.1}$$

A unitary matrix can be parameterized using a antysymmetric matrix $\mathbf{X}$ as,

$$\mathbf{U} = \exp(\mathbf{X}), \tag{2.2}$$

$$\mathbf{X}^{\dagger} = -\mathbf{X}. \tag{2.3}$$

Using the derivative of the CAS-CI energy with respect to the matrix element of $\mathbf{X}$, the CAS-CI energy can be expanded to the 2nd order as,

$$E(\mathbf{X}) \approx E(\mathbf{0}) + \mathbf{g}^{\dagger}\mathbf{X} + \frac{1}{2}\mathbf{X}^{\dagger}\mathbf{H}\mathbf{X}, \tag{2.4}$$

where $\mathbf{g}$ and $\mathbf{H}$ are the 1st-order and 2nd-order derivative of the CAS-CI energies. Note that $\mathbf{X}$ in Eqn. 2.4 is regarded as a column vector, where a pair of indices p and q behaves as an index. $\mathbf{X}$ for orbital rotation is determined by taking the eigenvector with lowest eigenvalue the augmented Hessian,

$$\begin{pmatrix} 0 & \mathbf{g}^{\dagger} \\ \mathbf{g} & \mathbf{H}/\lambda \end{pmatrix} \begin{pmatrix} 1/\lambda \\ \mathbf{X} \end{pmatrix} = \epsilon \begin{pmatrix} 1/\lambda \\ \mathbf{X} \end{pmatrix}. \tag{2.5}$$

In the two-step algorithm, CAS-CI and SCF steps are repeated until the CASSCF calculation reaches convergence.

2.2.2 Extended multistate complete-active-space 2nd-order perturbation (XMS-CASPT2) method

The extended multistate complete-active-space 2nd-order perturbation (XMS-CASPT2) method was developed as an extension of the complete-active-space 2nd-order perturbation theory (CASPT2). Although the description of the CASSCF solution is usually better than that of the HF solution, the reliability of the CASSCF result is usually insufficient. To increase the reliability of the computed results, some corrections should be conducted based on the

CASSCF solution. In the multireference perturbation theory (MRPT), such as CASPT2,[18] the correction is conducted perturbatively. In the CASPT2 theory, by constructing the generalized Fock matrix as the zeroth-order Hamiltonian, the 1st-order wavefunction is computed so as to minimize the Hylleraas functional. Because the generalized Fock matrix is not diagonal, the 1st-order wavefunction is computed iteratively. Note that only the diagonal part of the generalized Fock matrix was considered in the original paper by Roos et al.[18] Other MRPT methods include the multireference 2nd-order Møller–Plesset perturbation theory (MRMP2) by Hirao[19] and the N-electron valence 2nd-order perturbation theory (NEVPT2) by Angeli et al.[20–22]

In handling the degenerate electronic states, the perturbative correction should be considered based on the quasi-degenerate perturbation theory (QDPT). Roos et al. extended the CASPT2 to the multistate formulation, resulting in the multistate (MS-) CASPT2.[23] Similarly, Nakano extended the MRMP2 to the multiconfigurational quasi-degenerate 2nd-order perturbation theory (MCQDPT2)[24] while Angeli et al. extended the NEVPT2 to the QD-NEVPT2.[25] As a reference state, the CASSCF is solved so as to minimize the average of the energies of the states of interest, which is called state-averaged (SA-) CASSCF.

In 2011, Granovsky introduced the concept of the extended-MRPT to develop the extended MCQDPT2 (XMCQDPT2).[26] There, the reference state is prepared by diagonalizing the multistate Fock matrix to include the off-diagonal elements of the multistate Fock matrix. This extension resulted in smooth potential energy surfaces near the conical intersections with a negligible additional computational cost. Then Shiozaki et al. combined this concept with the MS-CASPT2 to develop the XMS-CASPT2.[1] Up to date, several extensions have been conducted to the XMS-CASPT2 method, including the analytical derivative coupling[3] and the use of the imaginary level-shift.[4]

Here, equations related to the XMS-CASPT2 were summarized based on Ref 2. First, the SA-CASSCF calculation should be conducted to obtain a set of wavefunctions $\{|M\rangle\}$ ($M = 1, 2, \cdots, N$) to be used for constructing the reference states. The reference state employed for the perturbative correction is constructed by diagonalizing the multistate Fock matrix. The Fock operator can be defind as,

$$\hat{f} = \sum_{pq} f_{pq} \hat{E}_{pq}, \tag{2.6}$$

where $\hat{E}_{pq}$ is the spin-summed single excitation operater and f_{pq} is the generalized Fock matrix constructed using the state-averaged 1-body reduced density matrix (SA-1-RDM). The formula of the $\hat{E}_{pq}$ and 1-RDM ($D^p_q(L, M)$) are given as,

$$\hat{E}_{pq} = a^\dagger_{p\alpha} a_{q\alpha} + a^\dagger_{p\beta} a_{q\beta}, \tag{2.7}$$

$$D^p_q(L, M) = \langle L|\hat{E}_{pq}|M\rangle\,. \tag{2.8}$$

Note that the $D^p_q(L, M)$ is called 1-RDM when L=M; otherwise, it is called 1-body transition RDM (1-TRDM). The matrix element of the multistate Fock matrix is given as,

$$f_{LM} = \langle L|\hat{f}|M\rangle = \sum_{pq} f_{pq} D^p_q(L, M). \tag{2.9}$$

The reference states are constructed by diagonalizing the multistate Fock matrix. When this diagonalization is given using a diagonal matrix $\tilde{\mathbf{f}}$ as,

$$\mathbf{U}^\dagger \mathbf{f} \mathbf{U} = \tilde{\mathbf{f}}, \tag{2.10}$$

the reference states $\{|\tilde{M}\rangle\}$ $(M = 1, 2, \cdots, N)$ are given by,

$$|\tilde{M}\rangle = \sum_L |L\rangle\, U_{LM}. \tag{2.11}$$

Note that the use of an identity matrix $\mathbf{1}$ as $\mathbf{U}$ is equivalent to the original MS-CASPT2, because this diagonalization was not conducted.

Using the reference states $\{|\tilde{M}\rangle\}$ thus obtained, perturbative correction is considered. The 1st-order wavefunction is expanded using the internally contracted basis (ICB), which is a set of wavefunctions produced by operating the double excitation operators to the reference state. There are two variants of the choice of the ICBs employed in the expansion.[27] One is the multistate multireference (MS-MR) scheme, where the 1st-order wavefunction for the reference $\{|\tilde{M}\rangle\}$ $(|\Psi_M^{(1)}\rangle)$ is expanded using ICBs produced by all of the references as,

$$|\Psi_M^{(1)}\rangle = \sum_L \sum_\Omega \hat{E}_\Omega\, |\tilde{L}\rangle\, T_{\Omega,LM}, \tag{2.12}$$

where $\hat{E}_\Omega$ are the spin-summed double excitation operaters $(\{\hat{E}_\Omega\} = \{\hat{E}_{pq}\hat{E}_{rs}\})$, and $T_{\Omega,LN}$ is the amplitude for the corresponding ICB. The other is the single-state single-reference (SS-SR) scheme, where the 1st-order wavefunction for the reference $\{|\tilde{M}\rangle\}$ $(|\Psi_M^{(1)}\rangle)$ is expanded using ICBs produced by $\{|\tilde{M}\rangle\}$ itself as,

$$|\Psi_M^{(1)}\rangle = \sum_\Omega \hat{E}_\Omega\, |\tilde{M}\rangle\, T_{\Omega,MM}. \tag{2.13}$$

Although the MS-MR contraction is better in accuracy than the SS-SR one, the computational cost in MS-MR one is larger than that in the SS-SR one. The amplitudes are computed by solving the amplitude equations for each reference state as,

$$\langle \tilde{M}|\hat{E}_\Omega^\dagger(\hat{f} - E_L^{(0)})|\Psi_L^{(1)}\rangle + \langle \tilde{M}|\hat{E}_\Omega^\dagger \hat{H}|\tilde{L}\rangle = 0. \tag{2.14}$$

Note that this equation is usually modified by introducing the level-shift technique, especially with the imaginary level-shift,[4,28] because the CASPT2 method is known to have the so-called intruder state problem. The amplitude equation with an imaginary shift $i\epsilon$ is rewritten as,

$$\langle \tilde{M}|\hat{E}_\Omega^\dagger(\hat{f} - E_L^{(0)}) + i\epsilon|\Psi_L^{(1)}\rangle + \langle \tilde{M}|\hat{E}_\Omega^\dagger \hat{H}|\tilde{L}\rangle = 0. \tag{2.15}$$

Using the 1st-order wavefunctions thus obtained, the symmetrized effective Hamiltonian is constructed as,

$$H_{ML}^{\text{eff}} = H_{ML}^{\text{ref}} + \frac{1}{2}\left(H_{ML}^{(2)} + H_{LM}^{(2)}\right) \tag{2.16}$$

$$= \langle \tilde{M}|\hat{H}|\tilde{L}\rangle + \frac{1}{2}\left(\langle \tilde{M}|\hat{H}|\Psi_L^{(1)}\rangle + \langle \tilde{L}|\hat{H}|\Psi_M^{(1)}\rangle\right). \tag{2.17}$$

Finally, diagonalization of the effective Hamiltonian gives the XMS-CASPT2 energies.

2.2.3 Density matrix renormalization group (DMRG-)XMS-CASPT2 method

The density matrix renormalization group (DMRG-) XMS-CASPT2 is an approximation of the XMS-CASPT2 method to reduce the computational cost in the CAS-CI step.[2] The DMRG was first introduced by White to study the model 1-dimensional system with a strong correlation.[29,30] Then, Chan and Yanai et al. introduced the DMRG into the diagonalization in the CAS-CI step of the CASSCF calculation. Using the resulting DMRG-CASSCF method, a CASSCF calculation with an active space of 24 electrons in the 24 orbitals, i.e. (24e,24o) was conducted,[31] although the upper limit of the conventional CASSCF was located near (14e,14o).

The DMRG algorithm is so complicated that only the concept of the DMRG-CASSCF is shown here in accordance with Ref. 32. The key concept of the DMRG-CASSCF is the low-rank approximation to the CAS-CI step based on the singular value decomposition (SVD). The DMRG-CAS-CI is composed of three steps: blocking, sweeping, and decimation. In the DMRG-CAS-CI, localized molecular orbitals are regarded to form a 1-dimensional system. The k molecular orbitals in the active space are transformed to the k localized orbitals and put into a 1-dimensional box. The position in the box is expressed by a set of indices $\{i\}$ ($i = 1, 2, \cdots, k$). By defining an electron configuration using the occupation state of each box n_i, where the occupation state is composed of empty, an α electron, a β electron and 2 electrons, the Full-CI wavefunction can be expressed as,

$$|\Psi_{\mathrm{FCI}}\rangle = \sum_{n_1 n_2 \cdots n_k} C_{n_1 n_2 \cdots n_k} |n_1 n_2 \cdots n_k\rangle . \tag{2.18}$$

In the DMRG-CAS-CI, the box of the localized orbitals is separated into 4 blocks; from the site 1 to site $p-1$ form the block L, the site p forms the block Δ_{L}, the site $p+1$ forms the block Δ_{R}, and the others form the block R. Using these blocks, the DMRG-CAS-CI wavefunction is given as,

$$|\Psi_{\mathrm{DMRG}}\rangle = \sum_{l n_p n_{p+1} r} C_{l n_p n_{p+1} r} |l\rangle |n_p\rangle |n_{p+1}\rangle |r\rangle , \tag{2.19}$$

where the basis of wavefunction of the block L ($|l\rangle$) and R ($|r\rangle$) are composed of the electronic configurations given by their components. When the bases $|l\rangle$ and $|r\rangle$ form a complete set, the DMRG wavefunction may cover the Full-CI wavefunction. In practice, the numbers of $|l\rangle$ and $|r\rangle$ are truncated by a user-defined constant M. Hence, the dimension of the DMRG wavefunction is at most $16M^2$, whereas the scaling of the dimension in the Full-CI is k!. Thanks to the small dimensions the coefficients in Eqn. 2.19 is determined by the diagonalization of the CI matrix.

Similar calculations should be conducted at other sites. In Eqn. 2.19, the block L is regarded as the system while R is regarded as the environment. Then, the next system is constructed using the old $|L\rangle$ and $|n_p\rangle$. In other words, p is replaced by $p+1$. This change in the system is repeated until the environment become empty; after that similar calculations

are conducted by regarding block R as the system and L as the environment. This gradual change in the position of the system is called the sweeping.

The dimensions of $|l\rangle$ and $|n_p\rangle$ are M and 4, respectively. To sweep the position, the dimension of $\bar{\mathrm{L}} = \mathrm{L} \bigotimes \Delta_{\mathrm{L}}$ should be reduced from $4M$ to M. This decrease in the dimension is achieved by the low-rank approximation of the density matrix. The set of $4M$ basis $|\bar{l}\rangle$ is given by the unitary transformation as,

$$|\bar{l}\rangle = \sum_{l=1}^{M} \sum_{n_p} U^{\bar{l}}_{ln_p} |l\rangle |n_p\rangle . \tag{2.20}$$

In this process, the unitary matrix is given by the diagonalization of the reduced density matrix $D^{\mathrm{L}}_{ln_p,l'n'_p}$, where $D^{\mathrm{L}}_{ln_p,l'n'_p}$ is given as.

$$D^{\mathrm{L}}_{ln_p,l'n'_p} = \sum_{n_{p+1}r} C_{ln_p n_{p+1} r} C^{*}_{l'n'_p n_{p+1} r}. \tag{2.21}$$

Using the eigenvalues of $D^{\mathrm{L}}_{ln_p,l'n'_p}$ $\{\omega_m\}$, the relation between $D^{\mathrm{L}}_{ln_p,l'n'_p}$ and $U^{\bar{l}}_{ln_p}$ is given as,

$$D^{\mathrm{L}}_{ln_p,l'n'_p} = \sum_{l=1}^{4M} \omega_{\bar{l}} U^{\bar{l}}_{ln_p} U^{\bar{l}}_{l'n'_p}. \tag{2.22}$$

Of the $4M$ eigenvalues, M highest eigenvalues and related eigenvectors are used; while others are truncated to reduce the dimension. This truncation process is called the decimation process. The total discarded weight, which is an index of the reliability of the DMRG approximation, is computed using the truncated eigenvalues.

To sum up, in the DMRG-CAS-CI, by iterating the blocking, decimation, and sweeping to reach convergence, a reasonable low-rank approximation to the CAS-CI calculation is conducted. By using the DMRG-CASSCF wavefunction for the construction of the reference states, DMRG-XMS-CASPT2 calculations are conducted.

2.3 Geometry optimization on the intersection of PESs

In the calculations in this thesis, minimal energy geometry of the conical intersection between singlet states or linear intersection between singlet and triplet states were optimized. The methods employed to write my Python code are summarized. First, a definition of potential energy surface (PES) is given. Second, geometry optimization is expressed as the numerical optimization of the energy on PES. Third, techniques unique to geometry optimization, such as handling cartesian coordinates or internal coordinates are shown. Finally, geometry optimization on the intersection space between PESs is shown.

2.3.1 Potential Energy Surfaces (PESs)

Here, the definition of a potential energy surface (PES) is briefly described. The time-independent Schrödinger equation is given as,

$$\hat{H}(\mathbf{r},\mathbf{R})\Psi(\mathbf{r},\mathbf{R}) = E\ \Psi(\mathbf{r},\mathbf{R}), \tag{2.23}$$

$$\hat{H}(\mathbf{r},\mathbf{R}) = \sum_A \frac{\hat{P}_A^2}{2M_A} + \sum_a \frac{\hat{P}_a^2}{2m_e} + V(\mathbf{r},\mathbf{R}), \tag{2.24}$$

where $\hat{H}(\mathbf{r},\mathbf{R})$ is the Hamiltonian, $\Psi(\mathbf{r},\mathbf{R})$ is the wavefunction, $\hat{P}_A$ is the momentum operator of the Ath nuclear, $\hat{P}_a$ is the momentum operator of the ath electron, M_A is the mass of the Ath nuclear, m_e is the mass of electron, and $V(\mathbf{r},\mathbf{R})$ is the potential energy arising from nuclei and electrons, respectively. In Eqn. 2.23, the energies are obtained as scalar eigenvalues, which depend on the quantum number of the eigenstates. Due to the difficulty in solving Eqn. 2.23, the electron Schrödinger equation (Eqn. 2.25), which is obtained by fixing the atomic coordinate at $\mathbf{R}$ in Eqn. 2.23, is solved in practice.

$$\hat{H}(\mathbf{r};\mathbf{R})\Psi_{\mathrm{e}}(\mathbf{r};\mathbf{R}) = E(\mathbf{R})\Psi_{\mathrm{e}}(\mathbf{r};\mathbf{R}), \tag{2.25}$$

$$\hat{H}(\mathbf{r};\mathbf{R}) = \sum_a \frac{\hat{P}_a^2}{2m_e} + V(\mathbf{r};\mathbf{R}). \tag{2.26}$$

In Eqn. 2.25, the atomic coordinates are regarded as parameters, making the eigenvalue of energy a function of the atomic coordinate. A potential energy surface is defined as the plot of the energy $E(\mathbf{R})$ with respect to atomic coordinate $\mathbf{R}$.[33]

2.3.2 Geometry optimization as a numerical optimization

Geometry optimization of a molecule in theoretical chemistry can be regarded as the search for the geometry of minimal energy point or saddle point on the PES. Because the analytical formula of PES with respect to nuclear coordinate cannot be obtained, the geometric search should be done numerically. In such a case, iterative procedure using derivatives of the target function, such as steepest descent method, Newton-Raphson method, and rational function optimization method (or augmented Hessian method), can be a possible choice.[34]

Taylor expansion of energy around the current geometry $\mathbf{R}$ at the 1st order is given using the 1st-order derivative (gradient, $\mathbf{g}$) as,

$$E(\mathbf{R}+\Delta\mathbf{R}) - E(\mathbf{R}) \approx \mathbf{g}^{\mathrm{T}}\Delta\mathbf{R} \tag{2.27}$$

$$g_i = \frac{\partial E}{\partial R_i} \tag{2.28}$$

To reduce the energy, the right side of Eqn. 2.27 should be negative. Considering that an inner product of the same real vector is a positive value, substitution of $\Delta\mathbf{R} = -\mathbf{g}$ yields,

$$E(\mathbf{R}-\mathbf{g}) - E(\mathbf{R}) \approx -\mathbf{g}^{\mathrm{T}}\mathbf{g} < 0 \tag{2.29}$$

The numerical optimization method based on Eqn. 2.29 is known as the steepest descent method. Because the use of $\Delta\mathbf{R} = -\mathbf{g}$ tends to give a too large displacement, the displacement is scaled before updating variables in practice; this scaling is common among the numerical optimization methods. This method is the simplest of the methods using gradient; however, this method is known to be a bad convergence.

Taylor expansion of energy around the current geometry $\mathbf{R}$ at the 2nd-order is given using

g and the 2nd-order derivative (Hessian matrix or force constant matrix, **H**) as,

$$E(\mathbf{R}+\Delta\mathbf{R}) - E(\mathbf{R}) \approx \mathbf{g}^{\mathrm{T}}\Delta\mathbf{R} + \frac{1}{2}\Delta\mathbf{R}^{\mathrm{T}}\mathbf{H}\Delta\mathbf{R} \tag{2.30}$$

$$H_{ij} = \frac{\partial^2 E}{\partial R_i \partial R_j} \tag{2.31}$$

Because Eqn. 2.30 is a collection of parabolas, their stationary points can be defined. Setting the partial derivative of the right-side of Eqn. 2.30 equal to **0**, we obtain,

$$\Delta\mathbf{R} = -\mathbf{H}^{-1}\mathbf{g}. \tag{2.32}$$

The numerical optimization based on Eqn. 2.32 is known as the Newton-Raphson method. From Eqn. 2.30 and 2.32, the change in energy can be estimated as,

$$E(\mathbf{R}+\Delta\mathbf{R}) - E(\mathbf{R}) \approx -\frac{1}{2}\Delta\mathbf{R}^{\mathrm{T}}\mathbf{H}\Delta\mathbf{R}. \tag{2.33}$$

Using the unitary matrix which diagonalizes **H** and corresponding eigenvalues **h**, Eqn. 2.33 can be rewritten as,

$$E(\mathbf{R}+\Delta\mathbf{R}) - E(\mathbf{R}) \approx -\frac{1}{2}\sum_i h_i \Delta R_i'^2, \tag{2.34}$$

$$\Delta\mathbf{R}' = \mathbf{U}^{\dagger}\Delta\mathbf{R} \tag{2.35}$$

Because the Newton-Raphson method employs the 2nd-order Taylor expansion, its convergence is known to be better than the steepest descent method. However, according to Eqn. 2.34, negative eigenvalue in **h** cause destabilization; hence, the positive definiteness of **H** is important to reach a local minimum, not any saddle point.

To ensure the positive definiteness of **H** in determining displacement, the use of the augmented Hessian is an effective choice. In the rational function optimization (RFO) method,[35] energy is expanded using rational function as,

$$E(\mathbf{R}+\Delta\mathbf{R}) - E(\mathbf{R}) \approx \frac{\mathbf{g}^{\mathrm{T}}\Delta\mathbf{R} + \frac{1}{2}\Delta\mathbf{R}^{\mathrm{T}}\mathbf{H}\Delta\mathbf{R}}{1 + \Delta\mathbf{R}^{\mathrm{T}}\mathbf{S}\Delta\mathbf{R}}, \tag{2.36}$$

where the **S** is a unit matrix or a scaled unit matrix.[35,36] By setting the partial derivative of the right-side of Eqn. 2.36 with respect to $\Delta\mathbf{R}$ equal to **0**, we obtain,

$$\begin{pmatrix} \mathbf{H} & \mathbf{g} \\ \mathbf{g}^{\mathrm{T}} & 0 \end{pmatrix} \begin{pmatrix} \Delta\mathbf{R} \\ 1 \end{pmatrix} = \lambda \begin{pmatrix} \mathbf{S} & \mathbf{0} \\ \mathbf{0}^{\mathrm{T}} & 1 \end{pmatrix} \begin{pmatrix} \Delta\mathbf{R} \\ 1 \end{pmatrix}. \tag{2.37}$$

Practically, $\Delta\mathbf{R}$ is computed by diagonalizing the augmented Hessian, i.e. the matrix on the left-side of Eqn. 2.37, and being scaled so as to the last term become 1. Separation of 2.37 yields,

$$(\mathbf{H} - \lambda\mathbf{S})\,\Delta\mathbf{R} + \mathbf{g} = \mathbf{0}, \tag{2.38}$$

$$\mathbf{g}^{\mathrm{T}}\Delta\mathbf{R} = \lambda. \tag{2.39}$$

Because **S** in Eqn. 2.38 a scaled unit matrix, the RFO method can be regarded as a method to add a constant shift ($-\lambda\alpha$ when $\mathbf{S} = \alpha\mathbf{I}$) to the eigenvalues of **H** in the Newton-Raphson

method.[35] In case the eigenvector of the augmented Hessian with the smallest eigenvalue is chosen, all of the eigenvalues of $(\mathbf{H} - \lambda\mathbf{S})$ become positive, resulting in the guarantee of the decrease in energy by a Newton-Raphson step. Similarly, when the eigenvector of the augmented Hessian with the second smallest eigenvalue is chosen, all of the eigenvalues of $(\mathbf{H} - \lambda\mathbf{S})$ except the smallest one become positive; this property is useful to search the 1st-order saddle point, i.e. the transition states in the PES.[35] As a modification, a method to strict the step size in RFO was proposed as the restricted-step RFO (RS-RFO) method.[36] In my Python code to optimize geometry, the RS-RFO method was mainly applied to determine the displacement.

As shown above, the Hessian matrix is required for Newton-Raphson and RFO methods. Computation of the Hessian matrix at each geometry might be possible; however, its large computational cost has encouraged us to take other approaches. Especially, in employing a method with its analytical hessian unavailable, the cost to compute the semi-numerical Hessian tends to become huge. In practice, geometry optimization with Hessian computed at each geometry is a rare procedure; instead, the initial Hessian is chosen from a guess Hessian or analytical/semi-numerical Hessian, then the Hessian is updated at each step by using the change in gradient because the Hessian matrix is the derivative of the gradient. This popular method, where an approximated Hessian is applied to Newton-Raphson step, is called the Quasi-newton method. There are several scheme to update Hessian. One of the popular methods, which is employed in my code, is the BFGS method, named after its inventors, Broyden, Fletcher, Goldfarb, and Shanno.[34] In the BFGS procedure, the Hessian matrix at the $(k+1)$th geometry is updated using the changes in the geometry ($\Delta\mathbf{R}^{(k,k+1)} = \mathbf{R}^{k+1} - \mathbf{R}^{k}$) and gradient ($\Delta\mathbf{g}^{(k,k+1)} = \mathbf{g}^{k+1} - \mathbf{g}^{k}$) as,

$$\mathbf{H}^{(k+1)} = \mathbf{H}^{(k)} - \frac{\mathbf{H}^{(k)}\Delta\mathbf{R}^{(k,k+1)}\Delta\mathbf{R}^{(k,k+1)^{\mathrm{T}}}\mathbf{H}^{(k)}}{\Delta\mathbf{R}^{(k,k+1)^{\mathrm{T}}}\mathbf{H}^{(k)}\Delta\mathbf{R}^{(k,k+1)}} + \frac{\Delta\mathbf{g}^{(k,k+1)}\Delta\mathbf{g}^{(k,k+1)^{\mathrm{T}}}}{\Delta\mathbf{g}^{(k,k+1)^{\mathrm{T}}}\Delta\mathbf{R}^{(k,k+1)}}. \tag{2.40}$$

The main advantages of the BFGS method are that the Hessian is updated by using Rank 2 matrix and that BFGS-updating of a positive-definite Hessian matrix gives a positive-definite Hessian matrix when the curvature condition is satisfied.

Note that the inverse of the Hessian matrix ($\mathbf{H}^{-1}$) is updated in usual quasi-Newton methods to avoid the computation of the inverse of Hessian matrix in Eqn. 2.32, because the computation of the inverse of a matrix tends to be numerically unstable and its computational cost is larger than that of matrix multiplication. Nevertheless, the Hessian matrix itself is updated in quantum mechanical geometry optimization; the possible reasons are that a reasonable guess Hessian can be prepared using the information of internal coordinates, and that conversion into internal coordinate space is a usual choice, which requires Hessian matrix itself.[37] In addition, the updating subroutine in the famous program Gaussian[38] uses gradient and geometry before kth step as well.

In optimization using the quasi-Newton method, the choice of the initial Hessian is also important because its quality affects the number of steps to reach convergence. The simplest guess is the use of a unit matrix, where the first step is equivalent to the steepest descent

method. In quantum mechanical geometry optimization, a guess diagonal Hessian can be constructed using the information of internal coordinate. Details are shown in the geometry optimization using Cartesian/internal coordinate sections.

2.3.3 Geometry optimization in Cartesian coordinate

Molecular geometry can be optimized based on Cartesian coordinate. The steepest descent method can be employed without any additional consideration; however, use of the other methods where Hessian matrix is employed requires additional manipulation. The Newton-Raphson method given in Eqn. 2.32 can be rewritten using the unitary matrix whith diagonalize Hessian matrix like Eqn. 2.35 as,

$$\mathbf{g}' = \mathbf{U}^\dagger \mathbf{g}, \tag{2.41}$$

$$\Delta\mathbf{R}' = -\mathbf{h}^{-1}\mathbf{g}', \tag{2.42}$$

$$\Delta R'_i = -\frac{g'_i}{h_i}, \tag{2.43}$$

where h_i is the i-th eigenvalue of the Hessian matrix. Eqn. 2.43 have the eigenvalues as a denominator; however, this is not suitable for molecular geometry optimization. The Hessian matrix is a $(3N \times 3N)$ square matrix. Because the $3N$ dimension contains translational and rotational contributions, which do not affect the energy of the molecule, the Hessian matrix is intrinsically $3N - 6$ dimension. This means that the Hessian matrix has 6 zeros as its eigenvalue, resulting in the divergence in Eqn. 2.43.

To avoid the divergence by zero-division, the translational and rotational contributions should be projected out from the full Hessian matrix. The translational $(\mathbf{c}_1, \mathbf{c}_2, \mathbf{c}_3)$ and rotational vectors $(\mathbf{c}_4, \mathbf{c}_5, \mathbf{c}_6)$ before normalization are given when the center of geometry, i.e. center of mass with all atomic masses equals, as,[39]

$$\mathbf{c}_1^{\mathrm{T}} = \mathbf{c}_{\mathrm{trx}}^{\mathrm{T}} = (1, 0, 0, 1, 0, 0, \cdots, 1, 0, 0), \tag{2.44}$$

$$\mathbf{c}_2^{\mathrm{T}} = \mathbf{c}_{\mathrm{try}}^{\mathrm{T}} = (0, 1, 0, 0, 1, 0, \cdots, 0, 1, 0), \tag{2.45}$$

$$\mathbf{c}_3^{\mathrm{T}} = \mathbf{c}_{\mathrm{trz}}^{\mathrm{T}} = (0, 0, 1, 0, 0, 1, \cdots, 0, 0, 1), \tag{2.46}$$

$$\mathbf{c}_4^{\mathrm{T}} = \mathbf{c}_{\mathrm{rotx}}^{\mathrm{T}} = (0, z_1, -y_1, 0, z_2, -y_2, \cdots, 0, z_N, -y_N), \tag{2.47}$$

$$\mathbf{c}_5^{\mathrm{T}} = \mathbf{c}_{\mathrm{roty}}^{\mathrm{T}} = (-z_1, 0, x_1, -z_2, 0, x_2, \cdots, -z_N, 0, x_N), \tag{2.48}$$

$$\mathbf{c}_6^{\mathrm{T}} = \mathbf{c}_{\mathrm{rotz}}^{\mathrm{T}} = (y_1, -x_1, 0, y_2, -x_2, 0, \cdots, y_N, -x_N, 0). \tag{2.49}$$

After (ortho-)normalizing these vectors, the Hessian and gradient are projected in a similar way in the internal coordinate[40] as,

$$\mathbf{P} = \mathbf{1} - \sum_{i=1}^{6} \mathbf{c}\mathbf{c}^{\mathrm{T}}, \tag{2.50}$$

$$\tilde{\mathbf{g}} = \mathbf{P}\mathbf{g}, \tag{2.51}$$

$$\tilde{\mathbf{H}} = \mathbf{P}\mathbf{H}\mathbf{P} + \alpha(\mathbf{1} - \mathbf{P})\mathbf{1}(\mathbf{1} - \mathbf{P}), \tag{2.52}$$

where α is a large constant; $\alpha = 1000$ was employed in Ref. 40, whereas $\alpha = 5000$ was employed in my case. Using these projected Hessian and gradient, the displacement to the

next geometry is computed as,

$$\Delta\mathbf{R} = -\tilde{\mathbf{H}}\tilde{\mathbf{g}}. \tag{2.53}$$

In this process, the zero eigenvalues are replaced by α. Because α is a large constant, displacements along the modes with zero eigenvalues become negligible under Eqn. 2.43. This corresponds to the concept of constrained optimization technique.[40]

Hessian must be prepared before projecting it. A typical guess Hessian for Quasi-Newton method is prepared by Badger's method.[41,42] A guess of the force constant of the stretch(i-j) is given as,

$$\frac{\partial^2 E}{\partial R_{ij}^2} = 0.3601 \exp(-1.944(R_{ij} - R_i^{\mathrm{cov}} - R_j^{\mathrm{cov}})). \tag{2.54}$$

By converting force constants from i-j distance basis into R_i and R_j basis using the chain rule, a guess Hessian can be obtained. Note that this guess Hessian has 6 zero eigenvalues because this is prepared based on bond distance, which is an element of internal coordinate.

2.3.4 Geometry optimization in internal coordinate

Molecular geometry can also be optimized based on internal coordinate space. The internal coordinate here contains the stretch (bond), bend (angle), and torsion (dihedral angle). The mathematical treatment of these internal coordinates is given Ref. 43 or source code of Psi4.[6] Here, the construction of internal coordinate and matrix operations are shown.

To construct the internal coordinate at the given geometry, a matrix representing the bond connectivity, i.e. a connectivity matrix, is constructed. The i-th and j-th atoms are considered to have connectivity between them when,

$$|\mathbf{R}_i - \mathbf{R}_j| < c(R_i^{\mathrm{cov}} + R_j^{\mathrm{cov}}), \tag{2.55}$$

where R_i^{cov} is the covalent radius of i-th atom and c is a scaling factor, respectively; and $c = 1.3$ is usually employed. When i-th and j-th atoms have connectivity, an internal coordinate of stretch(i-j) is assigned. Then, bends are assigned by connecting the stretches, i.e. a bend(i-j-k) is assignd when stretch(i-j) and stretch(j-k) exist. Similarly, a torsion(i-j-k-l) is assigned when bend(i-j-k) and bend(j-k-l) exist. Note that the inclusion of hydrogen bonds and handling bends at almost linear requires additional care. In my case, N, O, F, and Cl atoms are assigned to be hydrogen bond acceptors (X). H-X_2 bond is added when X_1-H bond exists, H-X_2 bond doesn't, and X_1-H-X_2 angle is larger than 90°.[6] On the other hand, the linear bend is expressed as the sum of two angles.[6,43,44] Then, the torsion containing a linear bend is replaced by other possible dihedrals. The intrinsic dimension of the internal coordinate is $3N - 6$; however, the number of the internal coordinated thus obtained is usually larger than it. Therefore, this set of internal coordinates is called redundant internal coordinates.

Based on the internal coordinates prepared, the Wilson's B matrix[45] is constructed as,

$$B_{ij} = \frac{\partial q_i}{\partial R_j}, \tag{2.56}$$

where q_i is i-th internal coordinate and R_j is the j-th cartesian coordinate, respectively. Because each internal coordinate is involved in at most 4 atoms, the B matrix is sparse.

For determining displacement, the Hessian and gradient must be transformed into internal coordinate space. Based on the chain rule, gradient and Hessian in two coordinate system satisfies the relation as,[40,43]

$$\mathbf{g}_R = \mathbf{B}^{\mathrm{T}}\mathbf{g}_q, \tag{2.57}$$

$$\mathbf{H}_R = \mathbf{B}^{\mathrm{T}}\mathbf{H}_q\mathbf{B} + \mathbf{B'}^{\mathrm{T}}\mathbf{g}_q, \tag{2.58}$$

where the subscript R and q represent Cartesian and internal coordinate system, respectively, and $\mathbf{B'}$ is the derivative of the B matrix given analytically as,

$$B'_{ijk} = \frac{\partial^2 q_i}{\partial R_j \partial R_k}. \tag{2.59}$$

To convert the gradient and Hessian from Cartesian to internal space, the inverse of the B matrix is required; however, the B matrix is a rectangular matrix when the number of the internal coordinates is larger than $3N-6$. In such a case, an operation using the pseudoinverse (or generalized inverse) properly works. Wilson's G matrix is given as

$$\mathbf{G} = \mathbf{B}\mathbf{u}\mathbf{B}^{\mathrm{T}}, \tag{2.60}$$

where $\mathbf{u}$ is an arbitrary matrix; usually, a unit matrix is employed in this context. Note that a diagonal matrix composed of the inverse of atomic masses is employed for vibrational analysis, as written later. G matrix a singular matrix with its rank at $3N-6$. By neglecting the zero eigenvalues, the generalized inverse of the G matrix is given using the unitary matrix which diagonalize G matrix.[40,46] When eigenvectors with nonzero eigenvalues build $\mathbf{K}$ and those with zero eigenvalues build $\mathbf{L}$, diagonalization of the G matrix can be written as,

$$\mathbf{G}\begin{pmatrix} \mathbf{K} & \mathbf{L} \end{pmatrix} = \begin{pmatrix} \mathbf{K} & \mathbf{L} \end{pmatrix}\begin{pmatrix} \mathbf{\Lambda} & \mathbf{0} \\ \mathbf{0} & \mathbf{0} \end{pmatrix}, \tag{2.61}$$

where $\mathbf{\Lambda}$ is a diagonal matrix composed of nonzero eigenvalues. Using matrices in Eqn. 2.61, generalized inverse of the G matrix is given as,

$$\mathbf{G}^{-} = \begin{pmatrix} \mathbf{K} & \mathbf{L} \end{pmatrix}\begin{pmatrix} \mathbf{\Lambda}^{-1} & \mathbf{0} \\ \mathbf{0} & \mathbf{0} \end{pmatrix}\begin{pmatrix} \mathbf{K}^{\mathrm{T}} \\ \mathbf{L}^{\mathrm{T}} \end{pmatrix}. \tag{2.62}$$

Then, the pseudoinverse of the B matrix is given as,[40,46]

$$\mathbf{B}^{-} = \left(\mathbf{G}^{-}\mathbf{B}\mathbf{u}\right)^{\mathrm{T}} = \mathbf{u}^{\mathrm{T}}\mathbf{B}^{\mathrm{T}}\mathbf{G}^{-}, \tag{2.63}$$

$$\left(\mathbf{B}^{\mathrm{T}}\right)^{-} = \mathbf{G}^{-}\mathbf{B}\mathbf{u}. \tag{2.64}$$

Finally, the gradient and Hessian are converted as,

$$\mathbf{g}_q = \mathbf{G}^{-}\mathbf{B}\mathbf{u}\mathbf{g}_R, \tag{2.65}$$

$$\mathbf{H}_q = \mathbf{G}^{-}\mathbf{B}\mathbf{u}(\mathbf{H}_R - \mathbf{B'}^{\mathrm{T}}\mathbf{g}_q)\mathbf{u}^{\mathrm{T}}\mathbf{B}^{\mathrm{T}}\mathbf{G}^{-}. \tag{2.66}$$

Using the Hessian and gradient in the internal coordinate space, the corresponding displacement can be computed; however, there are two problems: 1. treatment of the zero eigenvalues and 2. conversion of displacement into Cartesian coordinate.

When the internal coordinates constructed are redundant, the Hessian in internal coordinate becomes singular. To remove components with zero eigenvalue, a projector is constructed using eigenvectors of G matrix with zero eigenvalue ($\mathbf{L}$ in eq. 2.62) as,

$$\mathbf{P} = \mathbf{1} - \sum_{\mathbf{c}\in\mathbf{L}} \mathbf{c}\mathbf{c}^{\mathrm{T}} = \mathbf{G}\mathbf{G}^{-}. \tag{2.67}$$

Then, the gradient and Hessian are projected as,

$$\tilde{\mathbf{g}}_q = \mathbf{P}\mathbf{g}_q, \tag{2.68}$$

$$\tilde{\mathbf{H}}_q = \mathbf{P}\mathbf{H}_q\mathbf{P} + \alpha(\mathbf{1}-\mathbf{P})\mathbf{1}(\mathbf{1}-\mathbf{P}). \tag{2.69}$$

The displacement in internal coordinate space is computed in Newton-Raphson scheme as,

$$\Delta\mathbf{q} = -\tilde{\mathbf{H}}_q\tilde{\mathbf{g}}_q. \tag{2.70}$$

To obtain the next geometry, the displacement must be transformed into cartesian coordinate space. Because the relation between them is given by Wilson's B matrix (Eqn. 2.56) in infinitesimal manner, the conversion of a finite displacement ($\Delta\mathbf{q}$) into $\Delta\mathbf{R}$ cannot be conducted analytically; instead, this conversion is done in iterative method.[40,46] A pseudocode for this conversion follows.

procedure $\Delta\mathbf{q}$ TO $\Delta\mathbf{R}(\Delta\mathbf{q}, \mathbf{R})$
  $\Delta\mathbf{R} = \mathbf{0}$
  while RMS$(\Delta\Delta\mathbf{R}) > 1e-10$ **do**
    $\Delta\Delta\mathbf{q} = \Delta\mathbf{q} - (\mathbf{q}(\mathbf{R}+\Delta\mathbf{R}) - \mathbf{q}(\mathbf{R}))$
    $\Delta\Delta\mathbf{q} = \mathbf{P}\Delta\Delta\mathbf{q}$
    $\Delta\Delta\mathbf{R} = \mathbf{B}^{\mathrm{T}^{-}}\Delta\Delta\mathbf{q}$
    $\Delta\mathbf{R} = \Delta\mathbf{R} + \Delta\Delta\mathbf{R}$
  end while
end procedure

In the last, preparation of the initial Hessian for the quasi-Newton method is noted. In this context, the Hessian in internal coordinate is prepared rather than that in Cartesian basis, because a reasonable diagonal guess can be made for each internal coordinate. In the simple method, a constant is assigned for each internal coordinate type; namely, 0.5 for stretch, 0.2 for bend, and 0.1 for torsion, respectively. Other guess methods are suggested by Ficsher et al.[42] and Schlegel.[47]

2.3.5 Intersection of PESs

Geometry optimization on the intersection of PESs is regarded as an optimization of the higher-level state with constraints to keep the same adiabatic energy among states involving intersections. The number of constraints depends on the type of the intersection. Here, the intersection of the PESs is introduced before going into geometry optimization there. A famous type is the conical intersection, where two adiabatic states with the same spin

multiplicity are degenerate. The adiabatic energies of the state 1 (E_1) and state 2 (E_2) are represented by their diabatic energies (U_{11} and U_{22}) and diabatic coupling ($U_{12} = U_{21}$) as,[48]

$$E_1 = \frac{1}{2}(U_{11} + U_{22}) - \frac{1}{2}\sqrt{(U_{11} - U_{22})^2 + 4U_{12}^2}, \tag{2.71}$$

$$E_2 = \frac{1}{2}(U_{11} + U_{22}) + \frac{1}{2}\sqrt{(U_{11} - U_{22})^2 + 4U_{12}^2}. \tag{2.72}$$

These energies are obtained by diagonalizing the Hamiotonian in diabatic basis. On the conical intersection seam, $E_1 = E_2$ holds, which means $U_{11} = U_{22}$ and $U_{12} = 0$. Assuming the diabatic energies and diabatic couplings are linearly dependent on the geometrical displacement, the gradient of the square of the difference in adiabatic energies are given as,

$$\frac{\partial (E_2 - E_1)^2}{\partial R} = 2(U_{22} - U_{11})\left(\frac{\partial U_{22}}{\partial R} - \frac{\partial U_{11}}{\partial R}\right) + 8U_{12}\frac{\partial U_{12}}{\partial R}. \tag{2.73}$$

This means that the energy gap changes when geometry changes along the specific 2 directions; one is the difference gradient vector ($\mathrm{d}U_{22}/\mathrm{d}\mathbf{R} - \mathrm{d}U_{11}/\mathrm{d}\mathbf{R}$), and the other is the derivative coupling vector ($\mathrm{d}U_{12}/\mathrm{d}\mathbf{R}$).[48,49] Hence, a plane composed of the difference gradient vector and derivative coupling vector is called the brancing plane, while the other space is called the intersection seam. Because the adiabatic states are given by the linear combination of the diabatic states, these vectors for adiabatic energies are also given by the linear combination of those for diabatic energies, resulting in the same branching plane.[48] This means that we can apply the vectors for adiabatic energies to define the blanching plane; they are the difference gradient vector ($\mathbf{g}_2 - \mathbf{g}_1$) and the derivative of the interstate coupling, which is so closely related to the nonadiabatic coupling vector.[49–51] Because displacement in two dimensions (branching plane) lifts the degeneracy, the intersection seam is $3N-8$ dimension. Note that the conical intersection was named from that the plot of the adiabatic energies in the branching plane construct two cones.

Another type of intersection is the linear intersection, where two adiabatic states with different spin multiplicity are degenerate. The difference from the conical intersection is that the interstate diabatic coupling always becomes zero due to the spin-symmetry; hence, it is no longer a constraint. This results in the one-dimensional constraint given by gradient difference vector; therefore, the dimension of the linear intersection seam becomes $3N-7$.

The intrinsic dimension of the conical and linear intersection seams are $3N-8$ and $3N-7$; however, practically this dimension is affected by the quantum mechanical methods employed to compute the PES. Martínez and Olivucci et al. investigated the shape of the PES of Penta-2,4- dieniminium Cation Model around the conical intersection at the several quantum mechanical theories;[52] there, they found that some methods fail to produce the $3N-8$ dimensional intersection space. Some important findings are: (1)MRCISD properly gave a conical intersection; however, the inclusion of the Davidson correction gave a linear crossing because it lacks the correction to the coupling term. (2)Multi-state MR-QDPT methods, such as MS-CASPT2, QD-NEVPT2, and XMCQDPT2 methods, gave a conical intersection only when the MS-CASPT2 Hamiltonian is symmetrized; nevertheless, they gave a $3N-9$ dimensional intersection space. (3)TD-DFT using the restricted DFT as the reference gave a

linear intersection. (4)Spin-flip TD-DFT without spin projection gave a conical intersection. I did not pay attention to this point in this thesis because the objective is to obtain a geometry with the degeneracy of the states.

2.4 Geometry optimization in the intersection space of PESs

In this section, the geometry optimization on the intersection seam is provided. Because the linear intersection can be regarded as a special case of conical intersection, where the interstate diabatic coupling is always zero, the optimization on conical intersection seam is mainly written here.

There are several methods to optimize geometry on the intersection seam; the famous methods are the Lagrange-Newton method by Yarkony et al.,[50] the penalty function method by Persico et al.,[53] and the gradient projection method by Schlegel and Robb et al.[54,55] Thiel et al. compared these methods;[49] there, use of the gradient projection or the Lagrange-Newton methods is recommended unless the nonadiabatic coupling terms cannot be obtained, because the penalty function method is free from computing the nonadiabatic coupling. Then, Maeda et al. developed an updating scheme of the branching plane and combined it with the gradient projection method to make it free from the nonadiabatic coupling.[48] Blancafort et al. improved the convergence of the geometry optimization by introducing the double-Newton-Raphson method.[56] In this study, I employed these methods based on the gradient projection methods. These methods are briefly introduced. Other important extensions which I did not employ contain the combination with the single component artificial force induced reaction method (SC-AFIR) by Maeda et al.[57]

The key concept of the gradient projection is the separation of the full dimension $(3N-6)$ into the intersection space $(3N-8)$ and the branching plane (2).[54] The gap between states to be degenerate is minimized in the branching plane while the energy at the higher state is minimized in the intersection seam. Because the branching plane is given by the difference gradient vector and coupling derivative vector, unit vectors parallel to them ($\mathbf{x}$, $\mathbf{y}$) are used to build a projector as,

$$\mathbf{P}_{\mathrm{CI}} = \mathbf{1} - \mathbf{x}\mathbf{x}^{\mathrm{T}} - \mathbf{y}\mathbf{y}^{\mathrm{T}}. \tag{2.74}$$

Using this projector, the gradient in intersection space ($\mathbf{g}_{\mathrm{IS}}$) is given as,[54,55]

$$\mathbf{g}_{\mathrm{IS}} = \mathbf{P}\mathbf{g}_2 = \frac{1}{2}\mathbf{P}(\mathbf{g}_1 + \mathbf{g}_2), \tag{2.75}$$

while the gradient with respect to the energy gap ($\mathbf{g}_{\mathrm{BP}}$) is given as,

$$\mathbf{g}_{\mathrm{BP}} = 2(E_2 - E_1)\mathbf{x}. \tag{2.76}$$

Note that these projections must be conducted after transforming into the internal coordinate system.[56] In the original gradient method, the total gradient was defined as the sum of $\mathbf{g}_{\mathrm{IS}}$ and $\mathbf{g}_{\mathrm{BP}}$, this is to be minimized to obtain the minimal energy conical intersection geometry.

An approximated Hessian for the quasi-Newton method is updated by using the gradient in the optimization step.

However, the inclusion of the component in the branching plane can be problematic for updating Hessian, because this component may produce the displacement in the branching plane, resulting in the increase of energy gap.[56] To separate these components, Blancafort et al. employed two Hessians; one is for intersection space updated using $\mathbf{g}_{\mathrm{IS}}$, and the other for the branching space updated using $\mathbf{g}_{\mathrm{BP}}$. Using two Hessians, the displacement is obtained as,

$$\Delta q = \Delta q_{\mathrm{IS}} + \Delta q_{\mathrm{BP}}, \tag{2.77}$$

$$\Delta q_{\mathrm{IS}} = -\tilde{\mathbf{H}}_{\mathrm{IS}}\mathbf{g}_{\mathrm{IS}}, \tag{2.78}$$

$$\Delta q_{\mathrm{BP}} = -\mathbf{H}_{\mathrm{BP}}\mathbf{g}_{\mathrm{BP}} \tag{2.79}$$

By separating the two components, the number of steps to reach the space with degeneracy can be reduced.[56] However, in their paper, the treatment of $\mathbf{H}_{\mathrm{BP}}$ contains a problem related to a lot of zero eigenvalues. The authors avoided this problem by changing the optimization step from Newton-Raphson to the steepest descent after minimizing the energy gap. I think this problem can be removed by projecting $\mathbf{H}_{\mathrm{BP}}$ into 2 dimention as,

$$\tilde{\mathbf{H}}_{\mathrm{BP}} = (\mathbf{1} - \mathbf{P}_{\mathrm{CI}})\mathbf{H}_{\mathrm{BP}}(\mathbf{1} - \mathbf{P}_{\mathrm{CI}}) + \alpha\mathbf{P}_{\mathrm{CI}}\mathbf{1}\mathbf{P}_{\mathrm{CI}}. \tag{2.80}$$

Note that the projection to remove zero eigenvalues is also necessary for actual optimization.

2.5 Computation of the rate constant of transitions between vibronic states

I coded a Python program to estimate the rate constant of transitions between vibronic states. Theoretical details of the method and my implemantation are provided in this section.

2.5.1 Vibronic state and adiabatic approximation

Almost all of this subsection is written based on Ref. 33. The time-independent Schrödinger equation is written as Eqn. 2.23. The eigenvalues of Eqn. 2.23 is scaler values, and the eigenfunctions are the vibronic wavefunction, which is composed of electronic part and vibrational part. Eqn. 2.25 can be obtained by freezing the nuclear coordinates in Eqn. 2.23, resulting eigenvalues are scaler functions with respect to nuclear coodinate and eigenfunctions are the electronic wavefunctions. Because the eigenstates of Eqn. 2.25 form a complete set, the vibronic state in Eqn. 2.23 should be expanded using eigenstates of Eqn. 2.25. Using the coefficients which are functions of the nuclear coordinates ($\phi_n(\mathbf{R})$), the vibronic state can be expanded as,

$$\Psi(\mathbf{r}, \mathbf{R}) = \sum_n \phi_n(\mathbf{R})\psi_{en}(\mathbf{r}; \mathbf{R}). \tag{2.81}$$

Substitution of Eqn. 2.81 into Eqn. 2.23 yields,

$$\left[\sum_A \frac{\hat{P}_A^2}{2M_A} + \sum_a \frac{\hat{P}_a^2}{2m_e} + V(\mathbf{r},\mathbf{R})\right] \sum_n \phi_n(\mathbf{R})\psi_{en}(\mathbf{r};\mathbf{R}) = E \sum_n \phi_n(\mathbf{R})\psi_{en}(\mathbf{r};\mathbf{R}). \quad (2.82)$$

Integration of Eqn. 2.82 after multiplying $\psi_m(\mathbf{r};\mathbf{R})$ from left side yields,[33]

$$\sum_A \left\{ \frac{1}{2M_A} \left[\hat{P}_A^2 \phi_m(\mathbf{R}) + 2 \sum_n \left(\hat{P}_A \phi_n(\mathbf{R}) \int \psi_{em}^*(\mathbf{r};\mathbf{R}) \hat{P}_A \psi_{en}(\mathbf{r};\mathbf{R}) d\mathbf{r} \right) \right.\right.$$
$$\left.\left. + \sum_n \left(\phi_n(\mathbf{R}) \int \psi_{em}^*(\mathbf{r};\mathbf{R}) \hat{P}_A^2 \psi_{en}(\mathbf{r};\mathbf{R}) d\mathbf{r} \right) \right] \right\} + E_m(\mathbf{R})\phi_m(\mathbf{R}) = E\phi_m(\mathbf{R}) \quad (2.83)$$

Although Eqn. 2.83 determines the expansion coefficients $\phi_n(\mathbf{R})$ for $\psi_{en}(\mathbf{r};\mathbf{R})$, off-diagonal elements, such as $\psi_{en}(\mathbf{r};\mathbf{R})$ and $\psi_{em}(\mathbf{r};\mathbf{R})$, are included; this means that a vibronic wavefunction should be expanded using 1 or more electronic wavefunctions.

An approximation to Eqn. 2.83 where the off-diagonal elements of the momentum and momentum square are assumed to be 0 is called Born–Huang adiabatic approximation, or adiabatic approximation. In this approximation, Eqn. 2.83 is simplified to,

$$\left\{ \sum_A \left[\frac{1}{2M_A} \left(\hat{P}_A^2 + \int \psi_{em}^*(\mathbf{r};\mathbf{R}) \hat{P}_A^2 \psi_{em}(\mathbf{r};\mathbf{R}) d\mathbf{r} \right) \right] + E_m(\mathbf{R}) \right\} \phi_m(\mathbf{R}) = E\phi_m(\mathbf{R}). \quad (2.84)$$

Because $\phi_m(\mathbf{R})$ is determined using only the terms related to $\psi_{em}(\mathbf{r};\mathbf{R})$ in Eqn. 2.84, a vibronic wavefunction is expanded using only an electronic wavefunction ($\psi_{em}(\mathbf{r};\mathbf{R})$). There the expansion coefficient $\phi_m(\mathbf{R})$, i.e. the vibrational function, should be described by using the vibrational quantum number v as,

$$\Psi_{mv}(\mathbf{r},\mathbf{R}) = \phi_{mv}(\mathbf{R})\psi_{em}(\mathbf{r};\mathbf{R}). \quad (2.85)$$

The name of the "Adiabatic" approximation comes from that a vibronic wavefunction is described with just an electronic wavefunction. In other words, off-diagonal terms of the momentum which are neglected here are the electronic nonadiabatic coupling (NAC), which enables the nonadiabatic transitions.

On the other hand, the approximation where all terms related to the momentum of the electronic wavefunction are neglected is called the Born–Oppenheimer approximation. In this approximation, Eqn. 2.83 is simplified to,

$$\left\{ \sum_A \left[\frac{1}{2M_A} \left(\hat{P}_A^2 \right) \right] + E_m(\mathbf{R}) \right\} \phi_m(\mathbf{R}) = E\phi_m(\mathbf{R}). \quad (2.86)$$

In this approximation, a vibronic wavefunction is again expanded using only an electronic wavefunction ($\psi_{em}(\mathbf{r};\mathbf{R})$). The difference from the Born–Huang approximation is that the vibrational wavefunctions are obtained as the eigenstates of the Schrödinger equation of nuclei moving on the PES ($E_m(\mathbf{R})$).

2.5.2 Vibronic states employed in this study

The vibrational part of the vibronic states employed in this study is given under the harmonic potential approximation. By assuming that the PES is given by a collection of harmonic potential, the energy on the PES is given using the Hessian matrix at the $\mathbf{R}_0$ ($\mathbf{H}_m(\mathbf{R}_0)$) as,

$$E_m(\mathbf{R}) = E_m(\mathbf{R}_0) + (\mathbf{R}-\mathbf{R}_0)^{\mathrm{T}}\mathbf{H}_m(\mathbf{R}_0)(\mathbf{R}-\mathbf{R}_0). \tag{2.87}$$

The eigenstates of a harmonic oscillator can be analytically obtained, and the whole vibrational wavefunction is given by a collection of the eigenstates of each harmonic oscillator. In this study, this collection of the harmonic wavefunction is expressed as Θ_{mv}. In the formulations shown later, the initial (iv), final (fu), and intermediate (nw) vibronic states appear; these are given as,

$$|\Psi_{\mathrm{i}v}\rangle = |\Phi_{\mathrm{i}}\Theta_{\mathrm{i}v}\rangle\,,\ |\Psi_{\mathrm{f}u}\rangle = |\Phi_{\mathrm{f}}\Theta_{\mathrm{f}u}\rangle\,,\ |\Psi_{\mathrm{n}w}\rangle = |\Phi_{\mathrm{n}}\Theta_{\mathrm{n}w}\rangle\,, \tag{2.88}$$

where Ψ and Φ are the vibronic and electronic wavefunctions, respectively, while $v/u/w$ represents the vibrational state for corresponding vibronic state.

Note that the terms corresponding to electronic wavefunctions such as the transition dipole moment, NAC, and SOC are computed at a specific geometry: the minimum at the initial state. The choice of the geometry to compute these terms tends to affect the results. In this study, assuming that the major population at the initial state is located around the optimized geometry and that geometry does not change within the vibronic transition, these terms were computed at the minimum of the initial state. Discussion of the reference geometry can be seen in Ref. 58.

In computing these terms, the ordering of the electronic states can depend on the geometry employed. Thus, the character of the electronic state should be checked in computing coupling properties; there, visualization of the natural transition orbitals[59] can be an effective technique.

2.5.3 Correlation function formalism

(1) Absorption and fluorescence spectrum

The methods employed in this study are traces of the time-dependent formulations called the thermal vibration correlation function (TVCF) formalism proposed in Refs. 60, 61, and 8. There are similar studies using the time-dependent formalism,[62–65] as well as those using time-independent formalism.[44,58,66,67] The absorption spectrum is given as a function of angular frequency ω as,[8,60,68]

$$\sigma_{\mathrm{abs}}(\omega) = \frac{4\pi^2\omega}{3c}\sum_{v,u}\frac{\exp(-\beta E_{\mathrm{i}v})}{Z_{\mathrm{i}}}\left|\langle\Psi_{\mathrm{f}u}|\vec{\mu}_{\mathrm{fi}}|\Psi_{\mathrm{i}v}\rangle\right|^2\delta\left(-E_{\mathrm{fi}}+E_{\mathrm{i}v}-E_{\mathrm{f}u}+\hbar\omega\right), \tag{2.89}$$

where, c, Z_{i}, and E_{fi} are the velocity of light, vibrational partition function at the initial state, and adiabatic energy, respectively. The population of the vibrational state at the initial

state is given by the Boltzmann distribution in Eqn. 2.89, where the partition function is given from the depth of the harmonic potential because the vibrational energies here must be the eigenvalues of the vibrational Hamiltonian. Note that $E_\mathrm{i} < E_\mathrm{f}$ in photoabsorption results in $E_\mathrm{fi} = E_\mathrm{f} - E_\mathrm{i} > 0$. $|\langle\Psi_{\mathrm{f}u}|\vec{\mu}_\mathrm{fi}|\Psi_{\mathrm{i}v}\rangle|^2$ in Eqn. 2.89 represents the transition dipole moment between initial/final vibronic state. Here, expressions at the Franck–Condon (FC) level and Herzberg–Teller (HT) level are shown. In the FC approximation, the transition dipole moment is regarded as a constant vector with respect to nuclear geometry as,

$$\left|\langle\Psi_{\mathrm{f}u}|\vec{\mu}_\mathrm{fi}^\mathrm{FC}|\Psi_{\mathrm{i}v}\rangle\right|^2 \approx \left|\langle\Phi_\mathrm{f}|\vec{\mu}_\mathrm{fi}^\mathrm{FC}|\Phi_\mathrm{i}\rangle\,\langle\Theta_{\mathrm{f}u}|\Theta_{\mathrm{i}v}\rangle\right|^2 = \left|\vec{\mu}_\mathrm{fi}^\mathrm{FC}\right|^2 |\langle\Theta_{\mathrm{f}u}|\Theta_{\mathrm{i}v}\rangle|^2 . \tag{2.90}$$

Substituting Eqn. 2.89 into Eqn. 2.91 yields,

$$\sigma_\mathrm{abs}^\mathrm{FC}(\omega) = \frac{4\pi^2\omega}{3c}\sum_{v,u}\frac{\exp(-\beta E_{\mathrm{i}v})}{Z_\mathrm{i}}\left|\vec{\mu}_\mathrm{fi}^\mathrm{FC}\right|^2 |\langle\Theta_{\mathrm{f}u}|\Theta_{\mathrm{i}v}\rangle|^2\,\delta\left(-E_\mathrm{fi} + E_{\mathrm{i}v} - E_{\mathrm{f}u} + \hbar\omega\right). \tag{2.91}$$

In the time-independent formalism, or sum-over-state formalism, Eqn. 2.91 is calculated by computing the overlaps between vibrational wavefunctions, i.e. Franck–Condon factors.[58] On the contrary, in time-dependent formalism, the delta function in Eqn. 2.91 is Fourier transformed as,

$$\begin{aligned}\delta\left(-E_\mathrm{fi} + E_{\mathrm{i}v} - E_{\mathrm{f}u} + \hbar\omega\right) &= \delta\left(E_\mathrm{fi} - E_{\mathrm{i}v} + E_{\mathrm{f}u} - \hbar\omega\right)\\ &= \frac{1}{2\pi}\int_{-\infty}^{\infty} dt\ \exp\left(it\left(E_\mathrm{fi} - E_{\mathrm{i}v} + E_{\mathrm{f}v} - \hbar\omega\right)\right)\\ &= \frac{1}{2\pi\hbar}\int_{-\infty}^{\infty} dt\ \exp\left(it\left(\frac{E_\mathrm{fi}}{\hbar} - \frac{E_{\mathrm{i}v}}{\hbar} + \frac{E_{\mathrm{f}u}}{\hbar} - \omega\right)\right).\end{aligned} \tag{2.92}$$

Because the vibrational wavefunctions $\Theta_{\mathrm{i}v/\mathrm{f}u}$ are the eigenfunctions of the vibrational Hamiltonian $\hat{H}_{\mathrm{i/f}}$ with $E_{\mathrm{i}v/\mathrm{f}u}$ as eigenvalue, substitution of Eqn. 2.92 into Eqn. 2.91 yields,

$$\sigma_\mathrm{abs}^\mathrm{FC}(\omega) = \frac{2\pi\omega}{3\hbar c Z_\mathrm{i}}\left|\vec{\mu}_\mathrm{fi}^\mathrm{FC}\right|^2\int dt\ e^{-i\omega t}e^{i\omega_\mathrm{fi}t}\sum_{v,u}\left\langle\Theta_{\mathrm{f}u}\left|\, e^{-i\left(-i\beta+\frac{t}{\hbar}\right)\hat{H}_\mathrm{i}}\,\right|\Theta_{\mathrm{i}v}\right\rangle\left\langle\Theta_{\mathrm{i}v}\left|\, e^{-i\frac{-t}{\hbar}\hat{H}_\mathrm{f}}\,\right|\Theta_{\mathrm{f}u}\right\rangle. \tag{2.93}$$

The last term in Eqn. 2.93 is called the thermal vibration correlation function, which is given by the trace of matrices as,

$$\rho_\mathrm{abs}^\mathrm{FC}(t,T) = \mathrm{Tr}\left[\exp\left(-i\left(-i\beta + \frac{t}{\hbar}\right)\hat{H}_\mathrm{i}\right)\exp\left(-i\frac{-t}{\hbar}\hat{H}_\mathrm{f}\right)\right]. \tag{2.94}$$

Eqn. 2.93 and 2.94 indicate that the absorption spectrum at the Franck–Condon level can be theoretically estimated by computing the time-propagation of $e^{i\omega_\mathrm{fi}t}\rho_\mathrm{abs}^\mathrm{FC}(t,T)$ and subsequent Fourier transformation.

The fluorescence spectrum can also be estimated in a similar manner. The fluorescence spectrum at the Franck–Condon level is given by,

$$\sigma_\mathrm{ems}^\mathrm{FC}(\omega) = \frac{4\omega^3}{3c^3}\sum_{v,u}\frac{\exp(-\beta E_{\mathrm{i}v})}{Z_\mathrm{i}}\left|\vec{\mu}_\mathrm{fi}^\mathrm{FC}\right|^2 |\langle\Theta_{\mathrm{f}u}|\Theta_{\mathrm{i}v}\rangle|^2\,\delta\left(-E_\mathrm{fi} + E_{\mathrm{i}v} - E_{\mathrm{f}u} - \hbar\omega\right). \tag{2.95}$$

Note that $E_{\mathrm{fi}} = E_{\mathrm{f}} - E_{\mathrm{i}} < 0$ in Eqn. 2.95 because $E_{\mathrm{i}} > E_{\mathrm{f}}$ in the fluorescent decay. Similar to the computation of absorption spectrum, the Fourier transformation of the delta function in Eqn. 2.95 yields,

$$\sigma_{\mathrm{ems}}^{\mathrm{FC}}(\omega) = \frac{2\omega^3}{3\pi\hbar c^3 Z_{\mathrm{i}}} \left|\vec{\mu}_{\mathrm{fi}}^{\mathrm{FC}}\right|^2 \int dt\ e^{-i\omega t} e^{-i\omega_{\mathrm{fi}} t} \sum_{v,u} \left\langle \Theta_{\mathrm{f}u} \left| e^{-i\left(-i\beta - \frac{t}{\hbar}\right)\hat{H}_{\mathrm{i}}} \right| \Theta_{\mathrm{i}v} \right\rangle \left\langle \Theta_{\mathrm{i}v} \left| e^{-i\frac{t}{\hbar}\hat{H}_{\mathrm{f}}} \right| \Theta_{\mathrm{f}u} \right\rangle. \tag{2.96}$$

Then, the thermal vibration correlation function for the fluorescence spectrum is defined as,

$$\rho_{\mathrm{ems}}^{\mathrm{FC}}(t,T) = \mathrm{Tr}\left[\exp\left(-i\left(-i\beta - \frac{t}{\hbar}\right)\hat{H}_{\mathrm{i}}\right)\exp\left(-i\frac{t}{\hbar}\hat{H}_{\mathrm{f}}\right)\right] \tag{2.97}$$

Because the difference between the correlation functions in Eqn. 2.94 and 2.97 is the time for each vibrational Hamiltonian, they are given in the same expression as,

$$\tau_{\mathrm{i}} = \begin{cases} -i\beta + \frac{t}{\hbar} & (\mathrm{abs}) \\ -i\beta - \frac{t}{\hbar} & (\mathrm{ems}) \end{cases},\ \tau_{\mathrm{f}} = \begin{cases} -\frac{t}{\hbar} & (\mathrm{abs}) \\ +\frac{t}{\hbar} & (\mathrm{ems}) \end{cases}, \tag{2.98}$$

$$\rho^{\mathrm{FC}}(t,T) = \mathrm{Tr}\left[\exp\left(-i\tau_{\mathrm{i}}\hat{H}_{\mathrm{i}}\right)\exp\left(-i\tau_{\mathrm{f}}\hat{H}_{\mathrm{f}}\right)\right], \tag{2.99}$$

where $\tau_{\mathrm{i/f}}$ is the time for the vibrational Hamiltonian $\hat{H}_{\mathrm{i/f}}$. The difference in the time comes from the sign of $E_{\mathrm{i}v/\mathrm{f}u}/\hbar$ in the delta function in Eqn. 2.91 and 2.95 when the sign of $t/\hbar$ is "-". A similar discussion for the sign of time is given in Ref. 62. In my implementation, this sign is chosen so that Fourier transformation can be conducted using Numpy.fft.fft.[10] Note that this correlation function appears not only in the calculation of absorption/fluorescence spectra but also in that of the intersystem crossing rate constants at the FC level.

The absorption and emission spectra at the FC level are shown in Eqn. 2.91 and 2.95, where the transition dipole moment is assumed to be independent on nuclear coordinate. This assumption can be reasonable when the magnitude of the transition dipole is large enough; in other words, this assumption is insufficient for treating dipole-forbidden transitions. In such a case, the derivatives of the transition dipole moment with respect to geometry can have major contribution. Inclusion of the 1st-order derivatives is known as the Herzberg–Teller (HT) approximation, where the transition dipole moment at the FCHT level is given as,

$$\vec{\mu}_{\mathrm{fi}}^{\mathrm{FCHT}} = \vec{\mu}_{\mathrm{fi}}^{\mathrm{FC}} + \sum_k \left(\frac{\partial \vec{\mu}_{\mathrm{fi}}^{\mathrm{FC}}}{\partial Q_{\mathrm{f}k}}\right) Q_{\mathrm{f}k} \equiv \vec{\mu}_{\mathrm{fi}}^{\mathrm{FC}} + \sum_k \vec{\mu}_k Q_{\mathrm{f}k}. \tag{2.100}$$

Similar manipulation to Eqn. 2.90 yields,

$$\begin{aligned} \left|\langle \Psi_{\mathrm{f}u}|\vec{\mu}_{\mathrm{fi}}^{\mathrm{FCHT}}|\Psi_{\mathrm{i}v}\rangle\right|^2 \approx & \left|\langle \Phi_{\mathrm{f}}|\vec{\mu}_{\mathrm{fi}}^{\mathrm{FC}}|\Phi_{\mathrm{i}}\rangle \langle \Theta_{\mathrm{f}u}|\Theta_{\mathrm{i}v}\rangle\right|^2 \\ & + 2\sum_k \vec{\mu}_{\mathrm{fi}}^{\mathrm{FC}} \cdot \vec{\mu}_k \langle \Theta_{\mathrm{f}u}|\Theta_{\mathrm{i}v}\rangle \langle \Theta_{\mathrm{i}v}|Q_{\mathrm{f}k}|\Theta_{\mathrm{f}u}\rangle \\ & + \sum_{kl} \vec{\mu}_k \cdot \vec{\mu}_l \langle \Theta_{\mathrm{f}u}|Q_{\mathrm{f}k}|\Theta_{\mathrm{i}v}\rangle \langle \Theta_{\mathrm{i}v}|Q_{\mathrm{f}l}|\Theta_{\mathrm{f}u}\rangle. \end{aligned} \tag{2.101}$$

Substitution of Eqn. 2.101 into Eqn. 2.89 yields the expression of the absorption spectrum

at the Herzberg–Teller level as,

$$\sigma_{\rm abs}^{\rm FCHT}(\omega) = \sigma_{\rm abs}^{\rm FC}(\omega) + \sigma_{\rm abs}^{\rm FC/HT}(\omega) + \sigma_{\rm abs}^{\rm HT}(\omega), \tag{2.102}$$

$$\begin{aligned}\sigma_{\rm abs}^{\rm FC/HT}(\omega) = \frac{8\pi^2\omega}{3c}\sum_{v,u}\frac{\exp(-\beta E_{{\rm i}v})}{Z_{\rm i}}\delta\left(-E_{\rm fi}+E_{{\rm i}v}-E_{{\rm f}u}+\hbar\omega\right) \\ \times\sum_k \vec{\mu}_{\rm fi}^{\rm FC}\cdot\vec{\mu}_k\left\langle\Theta_{{\rm f}u}|\Theta_{{\rm i}v}\right\rangle\left\langle\Theta_{{\rm i}v}|Q_{{\rm f}k}|\Theta_{{\rm f}u}\right\rangle,\end{aligned} \tag{2.103}$$

$$\begin{aligned}\sigma_{\rm abs}^{\rm HT}(\omega) = \frac{4\pi^2\omega}{3c}\sum_{v,u}\frac{\exp(-\beta E_{{\rm i}v})}{Z_{\rm i}}\delta\left(-E_{\rm fi}+E_{{\rm i}v}-E_{{\rm f}u}+\hbar\omega\right) \\ \times\sum_{kl}\vec{\mu}_k\cdot\vec{\mu}_l\left\langle\Theta_{{\rm f}u}|Q_{{\rm f}k}|\Theta_{{\rm i}v}\right\rangle\left\langle\Theta_{{\rm i}v}|Q_{{\rm f}l}|\Theta_{{\rm f}u}\right\rangle.\end{aligned} \tag{2.104}$$

The thermal vibration correlation function at this level are given as,

$$\sigma_{\rm abs}^{\rm FC/HT}(\omega) = \frac{4\pi\omega}{3\hbar cZ_{\rm i}}\sum_k\vec{\mu}_{\rm fi}^{\rm FC}\cdot\vec{\mu}_k\int dt\ e^{-i\omega t}e^{i\omega_{\rm fi}t}\rho_{{\rm abs},k}^{\rm FC/HT}(t,T), \tag{2.105}$$

$$\rho_{{\rm abs},k}^{\rm FC/HT}(t,T) = {\rm Tr}\left[Q_{{\rm f}k}\exp\left(-i\left(-i\beta+\frac{t}{\hbar}\right)\hat{H}_{\rm i}\right)\exp\left(-i\frac{-t}{\hbar}\hat{H}_{\rm f}\right)\right], \tag{2.106}$$

$$\sigma_{\rm abs}^{\rm HT}(\omega) = \frac{2\pi\omega}{3\hbar cZ_{\rm i}}\sum_{kl}\vec{\mu}_k\cdot\vec{\mu}_l\int dt\ e^{-i\omega t}e^{i\omega_{\rm fi}t}\rho_{{\rm abs},kl}^{\rm HT}(t,T), \tag{2.107}$$

$$\rho_{{\rm abs},kl}^{\rm HT}(t,T) = {\rm Tr}\left[Q_{{\rm f}k}\exp\left(-i\left(-i\beta+\frac{t}{\hbar}\right)\hat{H}_{\rm i}\right)Q_{{\rm f}l}\exp\left(-i\frac{-t}{\hbar}\hat{H}_{\rm f}\right)\right]. \tag{2.108}$$

The expression of the fluorescence spectrum can be obtained in a similar manner to the Franck–Condon approximation. The important point is that the analytical formula of these correlation functions are formulated in the previous studies;[8,60] the analytical expressions are shown later.

Finally, integration of the fluorescence spectrum gives the radiative decay rate constant.

$$k_{\rm r} = \int_0^\infty {\rm d}\omega\ \sigma_{\rm ems}(\omega). \tag{2.109}$$

(2) Internal conversion

In this section, the correlation function formalism proposed in Refs. 60,69, and 8 is shown. The rate constant of the internal conversion can be derived from the 1st-order perturbation to the time-dependent Schrödinger equation as,[8,60,68,69]

$$k_{\rm ic} = \frac{2\pi}{\hbar}\sum_{v,u}\frac{\exp(-\beta E_{{\rm i}v})}{Z_{\rm i}}\left|H_{{\rm f}u,{\rm i}v}^{\rm nBO}\right|^2\delta\left(-E_{\rm fi}+E_{{\rm i}v}-E_{{\rm f}u}\right). \tag{2.110}$$

According to Ref. 60, $H^{\rm nBO}$ can be written under the Condon approximation as,

$$\begin{aligned}\left\langle\Phi_{\rm f}\Theta_{{\rm f}u}|\hat{H}^{\rm nBO}|\Phi_{\rm i}\Theta_{{\rm i}v}\right\rangle &= -\hbar^2\sum_k\left\langle\Phi_{\rm f}\Theta_{{\rm f}u}\left|\frac{\partial\Phi_{\rm i}}{\partial Q_{{\rm f}k}}\frac{\partial\Theta_{{\rm i}v}}{\partial Q_{{\rm f}k}}\right.\right\rangle \\ &\approx\sum_k\left\langle\Phi_{\rm f}|\hat{P}_{{\rm f}k}|\Phi_{\rm i}\right\rangle\left\langle\Theta_{{\rm f}u}|\hat{P}_{{\rm f}k}|\Theta_{{\rm i}v}\right\rangle.\end{aligned} \tag{2.111}$$

The first bracket in the right side of Eqn. 2.111 is the off-diagonal element of the momentum with respect to electronic wavefunction, which can be computed by multiplying $-i\hbar$

to derivative coupling (or nonadiabatic coupling) in QM calculations. The latter one is the off-diagonal element with respect to vibrational wavefinctions. Substitution of Eqn. 2.111 into 2.110 yields,

$$k_{\mathrm{ic}} = \sum_{kl} k_{\mathrm{ic},kl}, \tag{2.112}$$

$$R_{kl} = \langle \Phi_{\mathrm{f}} | \hat{P}_{\mathrm{f}k} | \Phi_{\mathrm{i}} \rangle \langle \Phi_{\mathrm{i}} | \hat{P}_{\mathrm{f}l} | \Phi_{\mathrm{f}} \rangle , \tag{2.113}$$

$$k_{\mathrm{ic},kl} = \frac{2\pi}{\hbar} R_{kl} \sum_{v,u} \frac{\exp(-\beta E_{\mathrm{i}v})}{Z_{\mathrm{i}}} \langle \Theta_{\mathrm{f}} | \hat{P}_{\mathrm{f}k} | \Theta_{\mathrm{i}} \rangle \langle \Theta_{\mathrm{i}} | \hat{P}_{\mathrm{f}l} | \Theta_{\mathrm{f}} \rangle \, \delta \left(-E_{\mathrm{fi}} + E_{\mathrm{i}v} - E_{\mathrm{f}u} \right). \tag{2.114}$$

Fourier transformation of the delta function in Eqn. 2.115 yields,

$$k_{\mathrm{ic},kl} = \frac{1}{\hbar^2 Z_{\mathrm{i}}} R_{kl} \int dt \; e^{-i\omega_{\mathrm{fi}} t} \rho_{\mathrm{ic},kl}(t,T), \tag{2.115}$$

$$\rho_{\mathrm{ic},kl}(t,T) = \mathrm{Tr} \left[\hat{P}_{\mathrm{f}k} \exp\left(-i \left(-i\beta - \frac{t}{\hbar} \right) \hat{H}_{\mathrm{i}} \right) \hat{P}_{\mathrm{f}l} \exp\left(-i \frac{t}{\hbar} \hat{H}_{\mathrm{f}} \right) \right], \tag{2.116}$$

or simply,

$$k_{\mathrm{ic}} = \frac{1}{\hbar^2 Z_{\mathrm{i}}} \int dt \; e^{-i\omega_{\mathrm{fi}} t} \sum_{kl} R_{kl} \rho_{\mathrm{ic},kl}(t,T). \tag{2.117}$$

Note that the thermal vibration correlation function shown in Eqn. 2.116 contains the operator of the momentum $\hat{P}_{\mathrm{f}k}$, rather than normal coordinate $Q_{\mathrm{f}k}$; hence, $\rho_{\mathrm{ic},kl}(t,T)$ is different from $\rho_{kl}^{\mathrm{HT}}(t,T)$ in Eqn. 2.108. Eqn. 2.117 indicates that k_{ic} can be theoretically estimated by computing the time-propagation of $\sum_{kl} R_{kl} \rho_{\mathrm{ic},kl}(t,T)$ and subsequent Fourier transformation. To satisfy $\omega_{\mathrm{fi}} > 0$ for the use of Numpy.fft.fft, times for vibrational Hamiltonian are chosen as,

$$\tau_{\mathrm{i}} = \begin{cases} -i\beta + \frac{t}{\hbar} & (\omega_{\mathrm{fi}} < 0) \\ -i\beta - \frac{t}{\hbar} & (\omega_{\mathrm{fi}} > 0) \end{cases}, \; \tau_{\mathrm{f}} = \begin{cases} -\frac{t}{\hbar} & (\omega_{\mathrm{fi}} < 0) \\ +\frac{t}{\hbar} & (\omega_{\mathrm{fi}} > 0) \end{cases}, \tag{2.118}$$

$$\rho_{\mathrm{ic},kl}(t,T) = \mathrm{Tr} \left[P_{\mathrm{f}k} \exp\left(-i\tau_{\mathrm{i}} \hat{H}_{\mathrm{i}} \right) P_{\mathrm{f}l} \exp\left(-i\tau_{\mathrm{f}} \hat{H}_{\mathrm{f}} \right) \right]. \tag{2.119}$$

This selection corresponds to the sign in the delta function in Eqn. 2.114; when $\omega_{\mathrm{fi}} < 0$, manipulation in Eqn. 2.92 is conducted for changing $e^{-i\omega_{\mathrm{fi}} t} \rightarrow e^{i\omega_{\mathrm{fi}} t} = e^{-i|\omega_{\mathrm{fi}}|t}$. The analytical expression of this correlation function has also been derived,[8,60,69] as shown later.

(3) Intersystem crossing

This section is also based on the correlation function formalism in Refs. 61, and 8, while information of spin-sublevels is included in accordance with other papers.[70–72] The rate constant of intersystem crossing between the singlet and triplet states can be separated by the spin-sublevel of the corresponding triplet state as,[70,72]

$$k_{\mathrm{isc}}(\mathrm{S} \rightarrow \mathrm{T}) = \sum_{M}^{1,0,-1} k_{\mathrm{isc}}(\mathrm{S} \rightarrow \mathrm{T}^{M}) \equiv \sum_{M}^{1,0,-1} k_{\mathrm{isc}}^{M}, \tag{2.120}$$

$$k_{\mathrm{isc}}(\mathrm{T} \rightarrow \mathrm{S}) = \frac{1}{3} \sum_{M}^{1,0,-1} k_{\mathrm{isc}}(\mathrm{T}^{M} \rightarrow \mathrm{S}) \equiv \frac{1}{3} \sum_{M}^{1,0,-1} k_{\mathrm{isc}}^{M}. \tag{2.121}$$

The rate constant of the intersystem crossing can be obtained by a 2nd-order perturbation to the time-dependent Schrödinger equation as,[61,68]

$$k_{\mathrm{isc}}^{M} = \frac{2\pi}{\hbar}\sum_{v,u}\frac{\exp(-\beta E_{\mathrm{i}v})}{Z_{\mathrm{i}}}\left|H'^{,M}_{\mathrm{f}u,\mathrm{i}v} + \sum_{\mathrm{n},w}\frac{H'^{,M}_{\mathrm{f}u,\mathrm{n}w}H'^{,M}_{\mathrm{n}w,\mathrm{i}v}}{E_{\mathrm{i}v}-E_{\mathrm{n}w}}\right|^2 \delta\left(-E_{\mathrm{fi}}+E_{\mathrm{i}v}-E_{\mathrm{f}u}\right), \tag{2.122}$$

where $H'^{,M}$ is the interaction Hamiltonian composed of non-Born–Oppenheimer coupling and spin-orbit coupling as,

$$\hat{H}'^{,M}\Psi_{\mathrm{i}v} = \hat{H}^{\mathrm{nBO}}\Phi_{\mathrm{i}}(\mathbf{r};\mathbf{Q})\Theta_{\mathrm{i}v}(\mathbf{Q}) + \hat{H}^{\mathrm{SO},M}\Phi_{\mathrm{i}}(\mathbf{r};\mathbf{Q})\Theta_{\mathrm{i}v}(\mathbf{Q}). \tag{2.123}$$

Eqn. 2.122 contains the matrix elements of H' involving the intermediate states, such as the element between the final and intermediate states ($H'_{\mathrm{f}u,\mathrm{n}w}$) or the element between the intermediate and initial states ($H'_{\mathrm{n}w,\mathrm{i}v}$). Expansion of Eqn. 2.122 yields,

$$k_{\mathrm{isc}}^{M} = k_{\mathrm{isc}}^{M,(0)} + k_{\mathrm{isc}}^{M,(1)} + k_{\mathrm{isc}}^{M,(2)}, \tag{2.124}$$

$$\begin{aligned} k_{\mathrm{isc}}^{M,(0)} &= \frac{2\pi}{\hbar}\sum_{v,u}\frac{\exp(-\beta E_{\mathrm{i}v})}{Z_{\mathrm{i}}}\left|H'^{,M}_{\mathrm{f}u,\mathrm{i}v}\right|^2\delta\left(-E_{\mathrm{fi}}+E_{\mathrm{i}v}-E_{\mathrm{f}u}\right) \\ &= \frac{2\pi}{\hbar}\sum_{v,u}\frac{\exp(-\beta E_{\mathrm{i}v})}{Z_{\mathrm{i}}}\left|\langle\Phi_{\mathrm{f}}|H^{\mathrm{SO},M}|\Phi_{\mathrm{i}}\rangle\right|^2\left|\langle\Theta_{\mathrm{f}u}|\Theta_{\mathrm{i}v}\rangle\right|^2\delta\left(-E_{\mathrm{fi}}+E_{\mathrm{i}v}-E_{\mathrm{f}u}\right) \\ &\equiv \frac{2\pi}{\hbar}\sum_{v,u}\frac{\exp(-\beta E_{\mathrm{i}v})}{Z_{\mathrm{i}}}\left|H^{\mathrm{SO},M}_{\mathrm{fi}}\right|^2\left|\langle\Theta_{\mathrm{f}u}|\Theta_{\mathrm{i}v}\rangle\right|^2\delta\left(-E_{\mathrm{fi}}+E_{\mathrm{i}v}-E_{\mathrm{f}u}\right). \end{aligned} \tag{2.125}$$

The term in Eqn. 2.125 comes from the 1st-order perturbation, where NAC vanishes due to the different spin multiplicity between the initial and final states. Similarly, Fourier transformation of the delta function in Eqn. 2.125 yields,

$$k_{\mathrm{isc}}^{M,(0)} = \frac{1}{\hbar^2 Z_{\mathrm{i}}}\left|H^{\mathrm{SO},M}_{\mathrm{fi}}\right|^2\int dt\; e^{-i\omega_{\mathrm{fi}}t}\rho^{\mathrm{FC}}(t,T). \tag{2.126}$$

Again, depending on the sign of E_{fi}, τ_{i} and τ_{f} are chosen according to Eqn. 2.98. The estimation of k_{isc} using Eqn. 2.126 can be reasonable when the direct SOC ($\left|H^{\mathrm{SO},M}_{\mathrm{fi}}\right|$) is large enough. In other words, when direct SOC is not so large, other terms can show a major contribution.

The second and third terms in Eqn. 2.124 arise from the 2nd-order perturbation; and they are evaluated via intermediate electronc state. In order to expand Eqn. 2.122, $H'^{,M}_{\mathrm{f}u,\mathrm{n}w}$ is expanded as,

$$\begin{aligned} H'^{,M}_{\mathrm{f}u,\mathrm{n}w} &= \langle\Phi_{\mathrm{f}}\Theta_{\mathrm{f}u}|\hat{H}^{\mathrm{nBO}} + \hat{H}^{\mathrm{SO},M}|\Phi_{\mathrm{n}}\Theta_{\mathrm{n}w}\rangle \\ &\approx H^{\mathrm{SO},M}_{\mathrm{fn}}\langle\Theta_{\mathrm{f}u}|\Theta_{\mathrm{n}w}\rangle + \sum_{k}\langle\Phi_{\mathrm{f}}|\hat{P}_{\mathrm{f}k}|\Phi_{\mathrm{n}}\rangle\langle\Theta_{\mathrm{f}u}|\hat{P}_{\mathrm{f}k}|\Theta_{\mathrm{n}w}\rangle. \end{aligned} \tag{2.127}$$

Then, the second-order term in Eqn. 2.122 is expanded as,

$$\begin{aligned}
&\sum_{\mathrm{n},w} \frac{H'^{,M}_{\mathrm{f}u,\mathrm{n}w} H'^{,M}_{\mathrm{n}w,\mathrm{i}v}}{E_{\mathrm{i}v} - E_{\mathrm{n}w}} \\
&\approx \sum_{\mathrm{n}w} \frac{1}{E_{\mathrm{i}v} - E_{\mathrm{n}w}} \Big(H^{\mathrm{SO},M}_{\mathrm{fn}} H^{\mathrm{SO},M}_{\mathrm{ni}} \langle \Theta_{\mathrm{f}u} | \Theta_{\mathrm{n}w} \rangle \langle \Theta_{\mathrm{n}w} | \Theta_{\mathrm{i}v} \rangle \\
&\qquad + H^{\mathrm{SO},M}_{\mathrm{fn}} \langle \Theta_{\mathrm{f}u} | \Theta_{\mathrm{n}w} \rangle \sum_k \langle \Phi_{\mathrm{n}} | \hat{P}_{\mathrm{f}k} | \Phi_{\mathrm{i}} \rangle \langle \Theta_{\mathrm{n}w} | \hat{P}_{\mathrm{f}k} | \Theta_{\mathrm{i}v} \rangle \\
&\qquad + H^{\mathrm{SO},M}_{\mathrm{ni}} \langle \Theta_{\mathrm{n}w} | \Theta_{\mathrm{i}v} \rangle \sum_k \langle \Phi_{\mathrm{f}} | \hat{P}_{\mathrm{f}k} | \Phi_{\mathrm{n}} \rangle \langle \Theta_{\mathrm{f}u} | \hat{P}_{\mathrm{f}k} | \Theta_{\mathrm{n}w} \rangle \\
&\qquad + \sum_{kl} \langle \Phi_{\mathrm{f}} | \hat{P}_{\mathrm{f}k} | \Phi_{\mathrm{n}} \rangle \langle \Theta_{\mathrm{f}u} | \hat{P}_{\mathrm{f}k} | \Theta_{\mathrm{n}w} \rangle \langle \Phi_{\mathrm{n}} | \hat{P}_{\mathrm{f}l} | \Phi_{\mathrm{i}} \rangle \langle \Theta_{\mathrm{n}w} | \hat{P}_{\mathrm{f}l} | \Theta_{\mathrm{i}v} \rangle \Big) . \qquad (2.128)
\end{aligned}$$

In the case of the intersystem crossing, the spin multiplicity of the final state is different from that of the initial state; hence, either $\langle \Phi_{\mathrm{f}} | \hat{P}_{\mathrm{f}k} | \Phi_{\mathrm{n}} \rangle$ of $\langle \Phi_{\mathrm{n}} | \hat{P}_{\mathrm{f}l} | \Phi_{\mathrm{i}} \rangle$ is equal to 0, resulting in the vanish of the last line of Eqn. 2.128. Because the spin-orbit coupling between triplet electronic states can be nonzero, the term in the second line in Eqn. 2.128 do not vanish; however, this term is assumed to be smaller than terms in the third and fourth lines, resulting in the vanish of the term in the second line of Eqn. 2.128. In this way, Eqn. 2.128 can be written as,

$$\begin{aligned}
\sum_{\mathrm{n},w} \frac{H'^{,M}_{\mathrm{f}u,\mathrm{n}w} H'^{,M}_{\mathrm{n}w,\mathrm{i}v}}{E_{\mathrm{i}v} - E_{\mathrm{n}w}} &\approx \sum_{\mathrm{n}w,k} \frac{H^{\mathrm{SO},M}_{\mathrm{fn}} \langle \Theta_{\mathrm{f}u} | \Theta_{\mathrm{n}w} \rangle \langle \Phi_{\mathrm{n}} | \hat{P}_{\mathrm{f}k} | \Phi_{\mathrm{i}} \rangle \langle \Theta_{\mathrm{n}w} | \hat{P}_{\mathrm{f}k} | \Theta_{\mathrm{i}v} \rangle}{E_{\mathrm{i}v} - E_{\mathrm{n}w}} \\
&\quad + \sum_{\mathrm{n}w,k} \frac{H^{\mathrm{SO},M}_{\mathrm{ni}} \langle \Theta_{\mathrm{n}w} | \Theta_{\mathrm{i}v} \rangle \langle \Phi_{\mathrm{f}} | \hat{P}_{\mathrm{f}k} | \Phi_{\mathrm{n}} \rangle \langle \Theta_{\mathrm{f}u} | \hat{P}_{\mathrm{f}k} | \Theta_{\mathrm{n}w} \rangle}{E_{\mathrm{i}v} - E_{\mathrm{n}w}} . \qquad (2.129)
\end{aligned}$$

Furture, application of the Placzek approximation, where the difference in energies of the initial and intermediate vibronic states are approximated as the vertical excitation energies, and the resolution-of-identity of the complete set $|\Theta_{\mathrm{n}w}\rangle$ yields,

$$\begin{aligned}
\sum_{\mathrm{n},w} \frac{H'^{,M}_{\mathrm{f}u,\mathrm{n}w} H'^{,M}_{\mathrm{n}w,\mathrm{i}v}}{E_{\mathrm{i}v} - E_{\mathrm{n}w}} &\approx \sum_k \langle \Theta_{\mathrm{f}u} | \hat{P}_{\mathrm{f}k} | \Theta_{\mathrm{i}v} \rangle \sum_{\mathrm{n}} \left(H^{\mathrm{SO},M}_{\mathrm{fn}} \frac{\langle \Phi_{\mathrm{n}} | \hat{P}_{\mathrm{f}k} | \Phi_{\mathrm{i}} \rangle}{E_{\mathrm{i}} - E_{\mathrm{n}}} + \frac{\langle \Phi_{\mathrm{f}} | \hat{P}_{\mathrm{f}k} | \Phi_{\mathrm{n}} \rangle}{E_{\mathrm{i}} - E_{\mathrm{n}}} H^{\mathrm{SO},M}_{\mathrm{ni}} \right) \qquad (2.130) \\
&\equiv \sum_k \langle \Theta_{\mathrm{f}u} | \hat{P}_{\mathrm{f}k} | \Theta_{\mathrm{i}v} \rangle \, t^M_k . \qquad (2.131)
\end{aligned}$$

In practice, again because the spin multiplicity of the final state is different from that of the initial state, either the first or second term in the parenthesis of Eqn. 2.130 becomes zero.

Using Eqn. 2.131, the second term in Eqn. 2.124 is written as,

$$\begin{aligned}
k^{M,(1)}_{\mathrm{isc}} = \frac{2\pi}{\hbar} \sum_{v,u} \frac{\exp(-\beta E_{\mathrm{i}v})}{Z_{\mathrm{i}}} \Big(& H^{\mathrm{SO},M*}_{\mathrm{fi}} \langle \Theta_{\mathrm{f}u} | \Theta_{\mathrm{i}v} \rangle^* \sum_k \langle \Theta_{\mathrm{f}u} | \hat{P}_{\mathrm{f}k} | \Theta_{\mathrm{i}v} \rangle \, t^M_k \\
& + H^{\mathrm{SO},M}_{\mathrm{fi}} \langle \Theta_{\mathrm{f}u} | \Theta_{\mathrm{i}v} \rangle \sum_k \langle \Theta_{\mathrm{f}u} | \hat{P}_{\mathrm{f}k} | \Theta_{\mathrm{i}v} \rangle^* \, t^{M*}_k \Big) \, \delta \left(-E_{\mathrm{fi}} + E_{\mathrm{i}v} - E_{\mathrm{f}u} \right) . \qquad (2.132)
\end{aligned}$$

As is shown in Ref. 70, this term sometimes vanishes. Summation of Eqn. 2.132 with respect to spin-sublevel M yields,

$$k_{\mathrm{isc}}^{(1)} = \frac{1}{\hbar^2}\int dt\ e^{-i\omega_{\mathrm{fi}}t}\sum_{k,M}\left(w_k^M \rho_{\mathrm{isc},k}^{(1)\ \prime}(t,T) + w_k^{M*}\rho_{\mathrm{isc},k}^{(1)}(t,T)\right), \tag{2.133}$$

where $\mathbf{w}^M$ and correlation functions are given as,

$$\mathbf{w}^M = H_{\mathrm{fi}}^{\mathrm{SO},M*}\mathbf{t}^M, \tag{2.134}$$

$$\rho_{\mathrm{isc},k}^{(1)\ \prime}(t,T) = \mathrm{Tr}\left[P_{\mathrm{f}k}\exp\left(-i\tau_{\mathrm{i}}\hat{H}_{\mathrm{i}}\right)\exp\left(-i\tau_{\mathrm{f}}\hat{H}_{\mathrm{f}}\right)\right], \tag{2.135}$$

$$\rho_{\mathrm{isc},k}^{(1)}(t,T) = \mathrm{Tr}\left[\exp\left(-i\tau_{\mathrm{i}}\hat{H}_{\mathrm{i}}\right)P_{\mathrm{f}k}\exp\left(-i\tau_{\mathrm{f}}\hat{H}_{\mathrm{f}}\right)\right]. \tag{2.136}$$

Path-integration of these correlation functions gives the same analytical solution; then, Eqn. 2.133 yields,

$$k_{\mathrm{isc}}^{(1)} = \frac{2}{\hbar^2}\int dt\ e^{-i\omega_{\mathrm{fi}}t}\sum_{k}\mathrm{Re}\left[\sum_M w_k^M\right]\rho_{\mathrm{isc},k}^{(1)}(t,T). \tag{2.137}$$

Using the property of the singlet-triplet spin-orbit coupling, $H_{\mathrm{fi}}^{\mathrm{SO},1} = -H_{\mathrm{fi}}^{\mathrm{SO},-1*}$, and momentum, $\hat{P}_k^* = -\hat{P}_k$, a relation between w_k is obtained as,

$$w_k^{1*} = -w_k^{-1}. \tag{2.138}$$

This means that $w_k^1 + w_k^{-1}$ is purely imaginary for all vibrational modes. Thus, when $H^{\mathrm{SO},0}$ and momentum are purely imaginary, $w_k^1 + w_k^{-1} + w_k^0$ is purely imaginary for all vibrational modes, resulting in the vanish of term in Eqn. 2.137. Note that I found that the SOC between excited singlet state and excited triplet state produced by Q-Chem satisfies $H_{\mathrm{fi}}^{\mathrm{SO},1} = -H_{\mathrm{fi}}^{\mathrm{SO},-1*}$, while that between ground singlet and triplet state or SOC produced by ORCA satisfies $H_{\mathrm{fi}}^{\mathrm{SO},1} = H_{\mathrm{fi}}^{\mathrm{SO},-1*}$. In this case, similar manipulation leads to $w_k^1 + w_k^{-1} + w_k^0 \in \mathrm{Re}$ as well; and this term vanishes in such a case as well in Eqn. 2.132.

Using Eqn. 2.131, the third term in Eqn. 2.124 is written as,

$$\begin{aligned} k_{\mathrm{isc}}^{(2)} &= \frac{2\pi}{\hbar}\sum_{v,u}\frac{\exp(-\beta E_{\mathrm{i}v})}{Z_{\mathrm{i}}}\sum_{kl}\sum_{M}^{1,0,-1}\langle\Theta_{\mathrm{i}v}|\hat{P}_{\mathrm{f}k}|\Theta_{\mathrm{f}u}\rangle\, t_k^{M*}\,\langle\Theta_{\mathrm{i}v}|\hat{P}_{\mathrm{f}l}|\Theta_{\mathrm{f}u}\rangle^*\, t_l^M\,\delta\left(-E_{\mathrm{fi}} + E_{\mathrm{i}v} - E_{\mathrm{f}u}\right) \\ &= \frac{2\pi}{\hbar}\sum_{v,u}\frac{\exp(-\beta E_{\mathrm{i}v})}{Z_{\mathrm{i}}}\sum_{kl}T_{kl}\,\langle\Theta_{\mathrm{i}v}|\hat{P}_{\mathrm{f}k}|\Theta_{\mathrm{f}u}\rangle\,\langle\Theta_{\mathrm{f}u}|\hat{P}_{\mathrm{f}l}|\Theta_{\mathrm{i}v}\rangle\,\delta\left(-E_{\mathrm{fi}} + E_{\mathrm{i}v} - E_{\mathrm{f}u}\right), \end{aligned} \tag{2.139}$$

where a matrix $\mathbf{T}$ was introduced as,

$$\mathbf{T} \equiv \sum_M^{1,0,-1}\mathbf{t}^M\mathbf{t}^{M\dagger}. \tag{2.140}$$

Note that substitution of $\mathbf{T}$ into $\mathbf{R}$ in Eqn. 2.113 yields the rate constant of internal conversion (Eqn. 2.114); hence, the Fourier transformation of Eqn. 2.139 can be written by using the thermal vibration correlation function for internal conversion as,

$$k_{\mathrm{isc}}^{(2)} = \frac{1}{\hbar^2 Z_{\mathrm{i}}}\int dt\ e^{-i\omega_{\mathrm{fi}}t}\sum_{kl}T_{kl}\rho_{\mathrm{ic},kl}(t,T). \tag{2.141}$$

To sum up, all the terms in Eqn. 2.124 were shown.

(4) Intersystem crossing including the Herzberg–Teller term

In the formulations above, the intersystem crossing in the molecules with small direct SOC can be handled by considering the intermediate states in the expansion of the interaction Hamiltonian. On the other hand, the inclusion of the derivatives of SOC like HT approximation is another approach to handle the molecule with small direct SOC. Some previous studies have applied HT approximation to the SOC,[64,72–76] because SOCMEs of usual organic molecules are so small that its 1st-order derivatives tend to show the major contribution.[77] Although Shuai et al. did not handle the HT contribution to the intersystem crossings as far as I know, I tried to implement this level of computation. Including the Herzberg–Teller terms, SOC between triplet state with spin-sublevel of M and singlet state is given as,

$$H_{\mathrm{fi}}^{\mathrm{SO},M,\mathrm{FCHT}} = H_{\mathrm{fi}}^{\mathrm{SO},M,\mathrm{FC}} + \sum_k \frac{\partial H_{\mathrm{fi}}^{\mathrm{SO},M,\mathrm{FC}}}{\partial Q_{\mathrm{f}k}} Q_{\mathrm{f}k} \equiv H_{\mathrm{fi}}^{\mathrm{SO},M,\mathrm{FC}} + \sum_k H_{\mathrm{fi},k}^{\mathrm{SO},M} Q_{\mathrm{f}k}, \tag{2.142}$$

where the subscript FC was added to $H_{\mathrm{fi}}^{\mathrm{SO},M}$ for clarity. Similar manipulation to Eqn. 2.101 yields,

$$\begin{aligned}\left|\langle \Psi_{\mathrm{f}u}|H_{\mathrm{fi}}^{\mathrm{SO},M,\mathrm{FCHT}}|\Psi_{\mathrm{i}v}\rangle\right|^2 \approx{}& \left|\langle \Phi_{\mathrm{f}}|H_{\mathrm{fi}}^{\mathrm{SO},M,\mathrm{FC}}|\Phi_{\mathrm{i}}\rangle \langle \Theta_{\mathrm{f}u}|\Theta_{\mathrm{i}v}\rangle\right|^2 \\ &+ 2\mathrm{Re}\left[\sum_k H_{\mathrm{fi}}^{\mathrm{SO},M,\mathrm{FC}*} H_{\mathrm{fi},k}^{\mathrm{SO},M} \langle \Theta_{\mathrm{f}u}|\Theta_{\mathrm{i}v}\rangle \langle \Theta_{\mathrm{i}v}|Q_{\mathrm{f}k}|\Theta_{\mathrm{f}u}\rangle\right] \\ &+ \sum_{kl} H_{\mathrm{fi},k}^{\mathrm{SO},M*} H_{\mathrm{fi},l}^{\mathrm{SO},M} \langle \Theta_{\mathrm{f}u}|Q_{\mathrm{f}k}|\Theta_{\mathrm{i}v}\rangle \langle \Theta_{\mathrm{i}v}|Q_{\mathrm{f}l}|\Theta_{\mathrm{f}u}\rangle . \end{aligned} \tag{2.143}$$

Note that $\sum_M H_{\mathrm{fi},k}^{\mathrm{SO},M*} H_{\mathrm{fi},l}^{\mathrm{SO},M}$ is real when $H_{\mathrm{fi}}^{\mathrm{SO},0,\mathrm{FC}}$ is purely imaginary, because $H_{\mathrm{fi}}^{\mathrm{SO},1,\mathrm{FC}} = -H_{\mathrm{fi}}^{\mathrm{SO},-1,\mathrm{FC}*}$. Again, in case with $H_{\mathrm{fi}}^{\mathrm{SO},1} = H_{\mathrm{fi}}^{\mathrm{SO},-1*}$, $\sum_M H_{\mathrm{fi},k}^{\mathrm{SO},M*} H_{\mathrm{fi},l}^{\mathrm{SO},M}$ is real. Substitution of Eqn. 2.143 as the interaction Hamiltonian in Eqn. 2.125 yields,

$$k_{\mathrm{isc}}^{M,\mathrm{FCHT}} = k_{\mathrm{isc}}^{M,\mathrm{FC}} + k_{\mathrm{isc}}^{M,\mathrm{FC/HT}} + k_{\mathrm{isc}}^{M,\mathrm{HT}}, \tag{2.144}$$

$$k_{\mathrm{isc}}^{M,\mathrm{FC}} = \frac{2\pi}{\hbar} \sum_{v,u} \frac{\exp(-\beta E_{\mathrm{i}v})}{Z_{\mathrm{i}}} \left|H_{\mathrm{f}u,\mathrm{i}v}^{\mathrm{SO},M,\mathrm{FC}}\right|^2 |\langle \Theta_{\mathrm{f}u}|\Theta_{\mathrm{i}v}\rangle|^2 \, \delta\left(-E_{\mathrm{fi}} + E_{\mathrm{i}v} - E_{\mathrm{f}u}\right), \tag{2.145}$$

$$\begin{aligned} k_{\mathrm{isc}}^{M,\mathrm{FC/HT}} = \frac{4\pi}{\hbar} \sum_{v,u} \frac{\exp(-\beta E_{\mathrm{i}v})}{Z_{\mathrm{i}}} &\mathrm{Re}\left[\sum_k H_{\mathrm{fi}}^{\mathrm{SO},M,\mathrm{FC}*} H_{\mathrm{fi},k}^{\mathrm{SO},M} \langle \Theta_{\mathrm{f}u}|\Theta_{\mathrm{i}v}\rangle \langle \Theta_{\mathrm{i}v}|Q_{\mathrm{f}k}|\Theta_{\mathrm{f}u}\rangle\right] \\ &\times \delta\left(-E_{\mathrm{fi}} + E_{\mathrm{i}v} - E_{\mathrm{f}u}\right), \end{aligned} \tag{2.146}$$

$$\begin{aligned} k_{\mathrm{isc}}^{M,\mathrm{HT}} = \frac{4\pi}{\hbar} \sum_{v,u} \frac{\exp(-\beta E_{\mathrm{i}v})}{Z_{\mathrm{i}}} &\sum_{kl} H_{\mathrm{fi},k}^{\mathrm{SO},M*} H_{\mathrm{fi},l}^{\mathrm{SO},M} \langle \Theta_{\mathrm{f}u}|Q_{\mathrm{f}k}|\Theta_{\mathrm{i}v}\rangle \langle \Theta_{\mathrm{i}v}|Q_{\mathrm{f}l}|\Theta_{\mathrm{f}u}\rangle \\ &\times \delta\left(-E_{\mathrm{fi}} + E_{\mathrm{i}v} - E_{\mathrm{f}u}\right). \end{aligned} \tag{2.147}$$

Eqn. 2.145 is the same as Eqn. 2.125. Eqn. 2.146 and 2.147 are quite simlar to those for absorption/fluorescence spectrum at the FCHT level (Eqn. 2.103 and 2.104); hence, the Fourier transformation of them can be written by using the same vibrartional correlation

functions as,

$$k_{\mathrm{isc}}^{M,\mathrm{FC/HT}} = \frac{2}{\hbar^2 Z_{\mathrm{i}}} \sum_k \mathrm{Re}\left[H_{\mathrm{fi}}^{\mathrm{SO},M,\mathrm{FC}^*} H_{\mathrm{fi},k}^{\mathrm{SO},M}\right] \int dt\ e^{-i\omega_{\mathrm{fi}}t} \rho_k^{\mathrm{FC/HT}}(t,T), \tag{2.148}$$

$$k_{\mathrm{isc}}^{M,\mathrm{HT}} = \frac{1}{\hbar^2 Z_{\mathrm{i}}} \sum_{kl} H_{\mathrm{fi},k}^{\mathrm{SO},M^*} H_{\mathrm{fi},l}^{\mathrm{SO},M} \int dt\ e^{-i\omega_{\mathrm{fi}}t} \rho_{kl}^{\mathrm{HT}}(t,T). \tag{2.149}$$

Broadening of delta function

In the formulations above, the delta function is employed to ensure energy conservation in the vibronic transitions. The use of delta function may suppress the convergence of correlation function with low temperature or small vibronic coupling;[60,65,78,79] instead, other functions, such as the Gaussian, Lorentzian, and Voigt functions are employed. This change introduces a broadening of the energy conservation in the vibronic transition. The use of the Gaussian function causes inhomogeneous broadening, which corresponds to the fluctuation of the solvent-solute interaction.[78,79] On the other hand, the use of the Lorentzian function cause homogeneous broadening, which comes from the finite lifetime of vibrational states, resulting from the Heisenberg uncertainty principle.[78] The use of the Voigt function includes both inhomogeneous and homogeneous broadening. Theoretically, the use of the Voigt function may be better; however, the inclusion of homogeneous broadening may show a large effect on computed results.[78] In my code, only the Gaussian broadening is considered. Note that I found that the use of Gaussian function is recommended in the manual of ORCA 5.0.1.[76]

The inclusion of the broadening effect introduces the Fourier transformation of the broadening function. This effect is handled by multiplying a factor to the time domain. The Gaussian function is given as[60]

$$G(\omega', \omega, \sigma) \equiv \frac{1}{\sigma\sqrt{2\pi}} \exp\left(-\frac{(\omega-\omega')^2}{2\sigma^2}\right), \tag{2.150}$$

where σ is the standard deviation, which is related to the half width at half maximum (HWHM) as HWHM $= \sigma\sqrt{2\ln 2}$. To include the broadening by Gaussian function, the function to be Fourier transformed is multiplied by $\exp(-\sigma^2 t^2/2)$. This factor ensures the convergence to 0 at the long time region.

2.5.4 Analytical expression of correlation functions under harmonic approximation

Shift vector and Duschinsky matrix

There are 5 types of thermal vibration correlation functions in previous sections: $\rho^{\mathrm{FC}}(t,T)$ in Eqn. 2.99, $\rho_k^{\mathrm{FC/HT}}(t,T)$ in Eqn. 2.106, $\rho_{kl}^{\mathrm{HT}}(t,T)$ in Eqn. 2.108, $\rho_{\mathrm{ic},kl}(t,T)$ in Eqn. 2.119, and $\rho_{\mathrm{isc},k}^{(1)}(t,T)$ in Eqn. 2.136. The analytical formula for them under the harmonic oscillator framework have been derived.[60,61,69–72,80,81] In these expressions, displacements along the normal modes (Shift vector) and the transformation matrix between normal modes at the initial and final PESs (Duschincky matrix) are employed. In this section, Shift vector and

Duschinsky matrix are introduced before showing the analytical expression of the correlation functions.[60,61,69–72,80,81] In addition, the transformation of derivatives, such as NAC and derivatives of transition dipole moment or SOC, from the cartesian to normal coordinate system is also discussed. These derivatives may be given as the derivative with respect to cartesian coordinate by QM calculations, while the derivatives with respect to normal coordinate are required for the calculation of correlation function.

In the vibronic transitions, how much the harmonic oscillators move in the transition is an important element, because it is related to the overlaps of the vibrational wavefunctions (Franck–Condon factors). To compute the Franck–Condon factors, the normal coordinates at the initial state should be expanded using those at the final state. This transformation, which is called Duschinsky transformation, is given by,

$$Q_{\mathrm{i}l} = \sum_k S_{lk} Q_{\mathrm{f}k} + D_l, \tag{2.151}$$

where $\mathbf{S}$ and $\mathbf{D}$ are the Duschinsky matrix and the Shift vector, respectively. The Duschinsky matrix represents the transformation of the normal modes, which can be determined based on the cartesian coordinate as,

$$\mathbf{S} = \mathbf{L}_{\mathrm{i}}^{\mathrm{T}} \mathbf{L}_{\mathrm{f}}, \tag{2.152}$$

where $\mathbf{L}_{\mathrm{i/f}}$ is a matrix composed of the normal modes at the initial/final PES. The shift vector represents the displacements along the normal modes at the initial state, which can be determined based on the cartesian coordinate as,

$$\mathbf{D} = \mathbf{L}_{\mathrm{i}}^{\mathrm{T}} \mathbf{M}^{\frac{1}{2}} \left(\mathbf{R}_{\mathrm{f}} - \mathbf{R}_{\mathrm{i}} \right), \tag{2.153}$$

where $\mathbf{M}$ is a $3N \times 3N$ diagonal matrix of the atomic masses.

The normal vibrational modes $\mathbf{L}_{\mathrm{i/f}}$ in cartesian representation can be computed from the second-order derivative matrix of the energy (Hessian matrix, $\mathbf{H}$) in accordance with Gaussian,[38,82] and the vibrational partition function Z_{i} can be computed using their frequencies.[83] To compute the vibrational modes, first $\mathbf{H}$ in Cartesian coordinate is converted to the representation in the mass-weighted coordinate as,

$$H_{ij}^{\mathrm{mwc}} = \frac{H_{ij}}{\sqrt{M_i M_j}}, \tag{2.154}$$

where M_i is the mass of the i-th atom. Remember to convert the mass from the atomic mass unit into the atomic unit. Because $\mathbf{H}_{ij}^{\mathrm{mwc}}$ is a $(3N \times 3N)$ matrix, translational (3 dimensions) and rotational (3 dimensions) components must be projected out to reduce to $3N - 6$ dimension. To conduct that, the origin of the geometry should be set to the center of mass; this translation do not affect the $\mathbf{H}_{ij}^{\mathrm{mwc}}$ itself. When the origin of the geometry is the center of mass, the translational vector for x, y, and z direction before normalization are given as,

$$\mathbf{c}_1^{\mathrm{T}} = \mathbf{c}_{\mathrm{trx}}^{\mathrm{T}} = (\sqrt{M_1}, 0, 0, \sqrt{M_2}, 0, 0, \cdots, \sqrt{M_N}, 0, 0), \tag{2.155}$$

$$\mathbf{c}_2^{\mathrm{T}} = \mathbf{c}_{\mathrm{try}}^{\mathrm{T}} = (0, \sqrt{M_1}, 0, 0, \sqrt{M_2}, 0, \cdots, 0, \sqrt{M_N}, 0), \tag{2.156}$$

$$\mathbf{c}_3^{\mathrm{T}} = \mathbf{c}_{\mathrm{trz}}^{\mathrm{T}} = (0, 0, \sqrt{M_1}, 0, 0, \sqrt{M_2}, \cdots, 0, 0, \sqrt{M_N}). \tag{2.157}$$

Note that replacing the diagonal mass matrix with a unit matrix results in the translational vectors used for geometry optimization in Cartesian coordinate. To obtain the rotational vector, the matrix to diagonalize the moment of inertia tensor is required. Using the coordinate with the center of mass as origin, the moment of inertia tensor $\mathbf{I}$ is given as,

$$\mathbf{I} = \begin{pmatrix} I_{xx} & I_{xy} & I_{xz} \\ I_{yx} & I_{yy} & I_{yz} \\ I_{zx} & I_{zy} & I_{zz} \end{pmatrix} = \begin{pmatrix} \sum_i M_i(y_i^2+z_i^2) & -\sum_i M_i(x_i y_i) & -\sum_i M_i(x_i z_i) \\ -\sum_i M_i(x_i y_i) & \sum_i M_i(x_i^2+z_i^2) & -\sum_i M_i(y_i z_i) \\ -\sum_i M_i(x_i z_i) & -\sum_i M_i(y_i z_i) & \sum_i M_i(x_i^2+y_i^2) \end{pmatrix}. \tag{2.158}$$

Because the assignment of indeces in Ref. 82 looks confusing,[7] here the matrix to diagonalize $\mathbf{I}$ is explicitly defined as $\mathbf{X}$, where $\mathbf{IX} = \mathbf{Xi}$. Then, elements of the rotational vectors $(\mathbf{c}_4, \mathbf{c}_5, \mathbf{c}_6)$ before normalization are given as,

$$\mathbf{P} = \mathbf{RX}, \tag{2.159}$$

$$\mathbf{c}_4[3(i-1)+(j-1)+1] = \sqrt{M_i}\left(P_{i2}X_{j3} - P_{i3}X_{j2}\right), \tag{2.160}$$

$$\mathbf{c}_5[3(i-1)+(j-1)+1] = \sqrt{M_i}\left(P_{i3}X_{j1} - P_{i1}X_{j3}\right), \tag{2.161}$$

$$\mathbf{c}_6[3(i-1)+(j-1)+1] = \sqrt{M_i}\left(P_{i1}X_{j2} - P_{i2}X_{j1}\right), \tag{2.162}$$

where $i = 1, 2, 3, \cdots$ and $j = 1, 2, 3$ are the indices of the atoms and eigenvectors in $\mathbf{X}$, respectively. Then, a projector to remove translation and rotation is constructed by normalized $\mathbf{c}$ vectors as,

$$\mathbf{P} = \mathbf{1} - \sum_{k=1}^{6} \mathbf{c}_k \mathbf{c}_k^{\mathrm{T}}. \tag{2.163}$$

Then, the normal modes are obtained by diagonalizing projected Hessian in a similar way for geometry optimization[40] as,

$$\tilde{\mathbf{H}}^{\mathrm{mwc}} = \mathbf{P}\mathbf{H}^{\mathrm{mwc}}\mathbf{P} + 1000(\mathbf{1}-\mathbf{P})\mathbf{H}^{\mathrm{mwc}}(\mathbf{1}-\mathbf{P}), \tag{2.164}$$

$$\tilde{\mathbf{H}}^{\mathrm{mwc}}\mathbf{L} = \mathbf{L}\mathbf{h}. \tag{2.165}$$

Note that $\tilde{\mathbf{H}}^{\mathrm{mwc}}$ has 6 eigenvalues equal to 1000; corresponding eigenvectors are characterized as rotation or translation. The other $3N-6$ eigenvalues and eigenvectors are force constants and normal vibrational modes, respectively. Then, angular frequencies are obtained as the square root of the force constants. This projection treatment is quite similar to the one in the geometry optimization, where atomic masses are not considered. Finally, the partition function of molecular vibration can be computed using angular frequencies by,[83]

$$\Theta_{\mathrm{v},i} = \frac{\hbar\omega_i}{k_{\mathrm{B}}}, \tag{2.166}$$

$$Z_{\mathrm{v}} = \prod_{i=1}^{3N-6} \frac{\exp(-\frac{\Theta_{\mathrm{v},i}}{2T})}{1-\exp(-\frac{\Theta_{\mathrm{v},i}}{T})}, \tag{2.167}$$

where $\Theta_{\mathrm{v},i}$ are the vibrational temperatures.

In using Cartesian coordinate, however, the geometry at the final state must be superposed onto the one at the initial state before computing the Duschinsky matrix and shift vector

so as to minimize the displacements in the mass-weighted coordinate. In my code, rotation using quaterion[84,85] was employed in accordance with FCClasses.[7] For a given quaternion, $\mathbf{q}^{\mathrm{T}} = (q_0, q_1, q_2, q_3)$, where q_0 is a scalar part and (q_1, q_2, q_3) is a vector part, its corresponding rotation matrix $\mathbf{U}^{\mathrm{Rot}}(\mathbf{q})$ is given by,

$$\mathbf{U}^{\mathrm{Rot}}(\mathbf{q}) = \begin{pmatrix} q_0^2+q_1^2-q_2^2-q_3^2 & 2(-q_0q_3+q_1q_2) & 2(q_0q_2+q_1q_3) \\ 2(q_0q_3+q_1q_2) & q_0^2-q_1^2+q_2^2-q_3^2 & 2(-q_0q_1+q_2q_3) \\ 2(-q_0q_2+q_1q_3) & 2(q_0q_1+q_2q_3) & q_0^2-q_1^2-q_2^2+q_3^2 \end{pmatrix}. \tag{2.168}$$

Suppose the Cartesian coordinate at the final state $\mathbf{R}_{\mathrm{f}}(N \times 3)$ is rotated as $\mathbf{R}_{\mathrm{f}}^{\mathrm{Rot}} = \mathbf{R}_{\mathrm{f}}\mathbf{U}^{\mathrm{Rot}}(\mathbf{q})^{\mathrm{T}}$ so as to minimize the deviation of the mass-weighted coordinate with the Cartesian coordinate at the initial state $\mathbf{R}_{\mathrm{i}}$. Deviation of the mass-weighted coordinate is given by,

$$m(\mathbf{q}) = \sum_{\alpha}^{N} M_\alpha \left| \mathbf{R}_{\mathrm{f},\alpha}\mathbf{U}^{\mathrm{Rot}}(\mathbf{q}) - \mathbf{R}_{\mathrm{i},\alpha} \right|^2, \tag{2.169}$$

where $\mathbf{R}_{\mathrm{f/i},\alpha}$ is the α-th row of $\mathbf{R}_{\mathrm{f/i}}$ and M_α is the mass of the α-th atom. The quaternion $\mathbf{q}$ for minimizing $m(\mathbf{q})$ is obtained as the eigenvector with the smallest eigenvalue of a matrix $\mathbf{M}_+$ as,

$$\mathbf{M}_+ = \sum_{\alpha=1}^{N} \left(M_\alpha \left(|\mathbf{R}_{\mathrm{f},\alpha}|^2 - |\mathbf{R}_{\mathrm{i},\alpha}|^2 \right) \mathbf{1} - 2\mathbf{F} \right), \tag{2.170}$$

where a (4×4) matrix $\mathbf{F}$ is given by,

$$\mathbf{F} = \sum_{\alpha=1}^{N} M_\alpha \begin{pmatrix} \mathbf{R}_{\mathrm{f},\alpha}\mathbf{R}_{\mathrm{i},\alpha}^{\mathrm{T}} & (\mathbf{R}_{\mathrm{f},\alpha} \times \mathbf{R}_{\mathrm{i},\alpha}) \\ (\mathbf{R}_{\mathrm{f},\alpha} \times \mathbf{R}_{\mathrm{i},\alpha})^{\mathrm{T}} & \mathbf{P}_\alpha - (\mathbf{R}_{\mathrm{f},\alpha}^{\mathrm{T}}\mathbf{R}_{\mathrm{i},\alpha})\mathbf{1} \end{pmatrix}, \tag{2.171}$$

$$\mathbf{P}_\alpha = \mathbf{R}_{\mathrm{f},\alpha}^{\mathrm{T}}\mathbf{R}_{\mathrm{i},\alpha} + \mathbf{R}_{\mathrm{i},\alpha}^{\mathrm{T}}\mathbf{R}_{\mathrm{f},\alpha}. \tag{2.172}$$

Note that $\mathbf{R}_{\mathrm{f/i},\alpha}$ is a row vector and $\mathbf{R}_{\mathrm{f/i},\alpha}^{\mathrm{T}}$ is a column vector. Using the quaternion $\mathbf{q}$ thus obtained, $\mathbf{U}^{\mathrm{Rot}}(\mathbf{q})$ is computed to rotate $\mathbf{R}_{\mathrm{f}}$. As well as the geometry, other vectors related to $\mathbf{R}_{\mathrm{f}}$, such as gradient $\mathbf{g}_{\mathrm{f}}$, normal modes $\mathbf{L}_{\mathrm{f}}$ *etc.*, must be rotated as,

$$\mathbf{g}_{\mathrm{f}}^{\mathrm{Rot}} = \mathbf{g}_{\mathrm{f}}\mathbf{U}^{\mathrm{Rot}}(\mathbf{q})^{\mathrm{T}}, \tag{2.173}$$

$$\mathbf{L}_{\mathrm{f}}^{\mathrm{Rot}} = \mathbf{U}^{\mathrm{RotL}}(\mathbf{q})\mathbf{L}_{\mathrm{f}}, \tag{2.174}$$

where the $(3N \times 3N)$ matrix $\mathbf{U}^{\mathrm{RotL}}(\mathbf{q})$ to rotate $\mathbf{L}_{\mathrm{f}}$ is given as,

$$\mathbf{U}^{\mathrm{RotL}} = \begin{pmatrix} \mathbf{U}^{\mathrm{Rot}}(\mathbf{q}) & \mathbf{0} & \cdots & \mathbf{0} \\ \mathbf{0} & \mathbf{U}^{\mathrm{Rot}}(\mathbf{q}) & \cdots & \mathbf{0} \\ \vdots & \vdots & \ddots & \vdots \\ \mathbf{0} & \mathbf{0} & \cdots & \mathbf{U}^{\mathrm{Rot}}(\mathbf{q}) \end{pmatrix}. \tag{2.175}$$

Then, the Duschinsky matrix and shift vector is given as,

$$\mathbf{S} = \mathbf{L}_{\mathrm{i}}^{\mathrm{T}}\mathbf{L}_{\mathrm{f}}^{\mathrm{Rot}} \tag{2.176}$$

$$\mathbf{D} = \mathbf{L}_{\mathrm{i}}^{\mathrm{T}}\mathrm{M}^{\frac{1}{2}} \left(\mathbf{R}_{\mathrm{f}}^{\mathrm{Rot}} - \mathbf{R}_{\mathrm{i}} \right). \tag{2.177}$$

Finally, derivetives with respect to cartesian coordinates ($\mathbf{d}_R(3N \times 1)$) is transformed into normal coordinate space at the final state PES ($\mathbf{d}_{Q_\mathrm{f}}(\mathrm{Nvib} \times 1)$) as,

$$\mathbf{d}_{Q_\mathrm{f}} = \mathbf{S}^\mathrm{T}\mathbf{L}_\mathrm{i}^\mathrm{T}\mathbf{M}^{\frac{1}{2}}\mathbf{d}_R = \mathbf{L}_\mathrm{f}^\mathrm{T}\mathbf{M}^{\frac{1}{2}}\mathbf{d}_R. \tag{2.178}$$

The normal modes can also be computed in the internal coordinate space. In this study, the redundant internal coordinate system[43,46,86] composed of stretch, bend, and torsions, was employed. In our implementation, the module for handling internal coordinates and building matrices, such as Wilson's B matrix,[45] was inserted from Psi4 program.[6] Operation of the matrices was coded in accordance with the beta version of FCClasses 3.0.[7] The use of internal coordinate in this context was discussed in previous studies.[9,44,66,87] In the case of flexible molecules, the use of internal coordinates is considered to improve the accuracy of the line shape of the predicted spectrum.[87]

Due to the chain rule in the derivatives, the use of internal coordinate requires Wilson's B matrix,[45] and G matrix,

$$B_{ij} = \frac{\partial q_i}{\partial R_j}, \tag{2.179}$$

$$\mathbf{G} = \mathbf{B}\mathbf{M}^{-1}\mathbf{B}^\mathrm{T}, \tag{2.180}$$

where q_i is i-th internal coordinate, R_j is the j-th cartesian coordinate, and $\mathbf{M}$ is a $3N \times 3N$ diagonal matrix of the atomic masses, respectively. Note that the B matrix here is constructed using cartesian coordinate, not mass-weighted coordinate; instead, the G matrix contains atomic masses. In the usual case where the internal coordinates are redundant, the B matrix is a rectangular matrix and the G matrix is a square, but singular matrix. Because the G matrix is singular, its inverse cannot be obtained; instead, psuedo inverse (or generalized inverse) matrix $\mathbf{G}^-$ can be defined. Using the generalized inverse of G matrix, that of B matrix is obtained as,

$$\mathbf{B}^- = \left(\mathbf{G}^-\mathbf{B}\mathbf{M}^{-1}\right)^\mathrm{T} = \mathbf{M}^{-1}\mathbf{B}^\mathrm{T}\mathbf{G}^{-\mathrm{T}}. \tag{2.181}$$

Because Hessian in cartesian coordinate $\mathbf{H}_R$ is computed at the minimum of PES here, which is known as Adiabatic Hessian model PES, Hessian in internal coordinate is given as,

$$\mathbf{H}_q = \mathbf{B}^{-\mathrm{T}}\mathbf{H}_R\mathbf{B}^-. \tag{2.182}$$

Then, normal coordinates in internal coordinate space $\mathbf{L}_q$ are expressed as,

$$\mathbf{G}\mathbf{H}_q\mathbf{L}_q = \mathbf{L}_q\mathbf{h} \tag{2.183}$$

After multiplying $\mathbf{G}^{-\frac{1}{2}}$ from left side of Eqn. 2.183, substitution of $\mathbf{L}_q = \mathbf{G}^{\frac{1}{2}}\mathbf{L}'_q$ like orthogonalization of Roothaan equation yields,

$$\mathbf{G}^{\frac{1}{2}}\mathbf{H}_q\mathbf{G}^{\frac{1}{2}}\mathbf{L}'_q = \mathbf{L}'_q\mathbf{h}. \tag{2.184}$$

Eqn. 2.184 indicates that $\mathbf{L}'_q$ is obtained by diagonalizing $\mathbf{G}^{\frac{1}{2}}\mathbf{H}_q\mathbf{G}^{\frac{1}{2}}$;[7] then, the normal modes are obtained by $\mathbf{L}_q = \mathbf{G}^{\frac{1}{2}}\mathbf{L}'_q$. This means that the normal modes $\mathbf{L}_q$ are not orthonormal,

while $\mathbf{L}'_q$ are orthonormal. Note that there are nonzero Nvib eigenvalues, while the others are zero. Only the eigenvectors in $\mathbf{L}'_q$ with nonzero eigenvalues are used to obtain normal modes $\mathbf{L}_q$. Using the normal modes thus obtained, the Duschinsky matrix and shift vector are given as,[87,88]

$$\mathbf{S} = {\mathbf{L}'_{q\mathrm{i}}}^{\mathrm{T}} \mathbf{G}_{\mathrm{i}}^{-\frac{1}{2}} \mathbf{G}_{\mathrm{f}}^{\frac{1}{2}} \mathbf{L}'_{q\mathrm{f}}, \tag{2.185}$$

$$\mathbf{D} = {\mathbf{L}'_{q\mathrm{i}}}^{\mathrm{T}} \mathbf{G}_{\mathrm{i}}^{-\frac{1}{2}} \left(\mathbf{q}_{\mathrm{f}} - \mathbf{q}_{\mathrm{i}}\right). \tag{2.186}$$

Note that this definition employed in FCClasses and my code is slightly different from that by Barone et al..[44] Finally, derivetives with respect to cartesian coordinates ($\mathbf{d}_R(3N \times 1)$) is transformed into normal coordinate space at the final state PES ($\mathbf{d}_{Q_\mathrm{f}}(\mathrm{Nvib} \times 1)$) as,

$$\mathbf{d}_{Q_\mathrm{f}} = \mathbf{S}^{\mathrm{T}} \mathbf{L}_{q\mathrm{i}}^{\mathrm{T}} {\mathbf{B}^{-1}}^{\mathrm{T}} \mathbf{d}_R. \tag{2.187}$$

To sum up, computation of the Duschinsky matrix, shift vector, and how to convert cartesian derivatives into normal coordinate space was presented both for cartesian coordinate and internal coordinate space.

Using the shift vector thus obtained, Huang–Rhys factor S_j and reorganization energy E_j^{reorg} along j-th mode are given as,

$$S_j = \frac{\omega_j D_j^2}{2\hbar}, \tag{2.188}$$

$$E_j^{\mathrm{reorg}} = \hbar \omega_j S_j. \tag{2.189}$$

The Huang–Rhys factor is related to overlap of vibrational wavefunction, i.e. the Franck–Condon factor. The Franck–Condon factor of j-th vibrational mode between vibrational groud state at the initial state $\chi_{\mathrm{i}0}$ and vibrational state at the final state $\chi_{\mathrm{f}a_j}$ is expressed under the harmonic approximation as,[89]

$$\left|\langle \chi_{\mathrm{f}a_j} | \chi_{\mathrm{i}0} \rangle\right|^2 = \frac{S_j^{a_j}}{a_j!} \exp(-S_j). \tag{2.190}$$

In case with $a_j = 0$ and $a_j = 1$, Eqn. 2.190 yields,

$$\left|\langle \chi_{\mathrm{f}0} | \chi_{\mathrm{i}0} \rangle\right|^2 = \frac{1}{0!} \exp(-S_j), \tag{2.191}$$

$$\left|\langle \chi_{\mathrm{f}1} | \chi_{\mathrm{i}0} \rangle\right|^2 = \frac{S_j}{1!} \exp(-S_j). \tag{2.192}$$

This means that the ratio between Franck–Condon factors with $a_j = 0$ and $a_j = 1$ is given as S_j. This relation reflects the intensity of peaks in the spectrum between 0-0 and 0-1 transitions.

Analytical expression of thermal vibration correlation functions

In this section, the analytical expression of the thermal vibration correlation function derived in previous studies[60,61,69–73,80,81] are shown. In this study, formulation by Shuai et al. is employed, while there are similar studies based on time-dependent formalism.[62–65,90]

Some studies say that formulation by Shuai et al. is numerically unstable,[62,65] probably due to the small vibrational partition function and small determinants.[65] However, I think my code works except for low temperature; I failed to compute the correlation function of Ito's molecule[91] at 5 K, while succeeded in it at 10 K. A similar problem was reported by Marian et al.,[64] where computation at the extremely low temperature was avoided by employing the formula at 0 K.

As menthioned above, there are 5 types of thermal vibration correlation functions in the computation of vibronic transitions: $\rho^{\mathrm{FC}}(t,T)$ in Eqn. 2.99, $\rho_k^{\mathrm{FC/HT}}(t,T)$ in Eqn. 2.106, $\rho_{kl}^{\mathrm{HT}}(t,T)$ in Eqn. 2.108, $\rho_{\mathrm{ic},kl}(t,T)$ in Eqn. 2.119 and $\rho_{\mathrm{isc},k}^{(1)}(t,T)$ in Eqn. 2.136. Their analytical formula under the harmonic approximation are derived by path-integration; the details are shown in previous studies.[60,61,69–73,80,81] The simplest case, correlation function at the Franck–Condon level is given as,

$$\rho^{\mathrm{FC}}(t,T) = \sqrt{\frac{\det\left[\mathbf{a}_{\mathrm{f}}\mathbf{a}_{\mathrm{i}}\right]}{\det[\mathbf{K}]}} \exp\left\{-\frac{i}{\hbar}\left[\frac{1}{2}\mathbf{F}^{\mathrm{T}}\mathbf{K}^{-1}\mathbf{F} - \mathbf{D}^{\mathrm{T}}\mathbf{E}\mathbf{D}\right]\right\}. \tag{2.193}$$

The definition of the matrices in Eqn. 2.193 are given by,

$$a_{\mathrm{i/f},kl}(\tau_{\mathrm{i/f}}) = \delta_{kl}\frac{\omega_{\mathrm{i/f},k}}{\sin(\omega_{\mathrm{i/f},k}\tau_{\mathrm{i/f}})} \qquad (\mathrm{Nvib}\times\mathrm{Nvib}), \tag{2.194}$$

$$b_{\mathrm{i/f},kl}(\tau_{\mathrm{i/f}}) = \delta_{kl}\frac{\omega_{\mathrm{i/f},k}}{\tan(\omega_{\mathrm{i/f},k}\tau_{\mathrm{i/f}})} \qquad (\mathrm{Nvib}\times\mathrm{Nvib}), \tag{2.195}$$

$$\mathbf{A} = \mathbf{a}_{\mathrm{f}} + \mathbf{S}^{\mathrm{T}}\mathbf{a}_{\mathrm{i}}\mathbf{S} \qquad (\mathrm{Nvib}\times\mathrm{Nvib}), \tag{2.196}$$

$$\mathbf{B} = \mathbf{b}_{\mathrm{f}} + \mathbf{S}^{\mathrm{T}}\mathbf{b}_{\mathrm{i}}\mathbf{S} \qquad (\mathrm{Nvib}\times\mathrm{Nvib}), \tag{2.197}$$

$$\mathbf{E} = \mathbf{b}_{\mathrm{i}} - \mathbf{a}_{\mathrm{i}} \qquad (\mathrm{Nvib}\times\mathrm{Nvib}), \tag{2.198}$$

$$\mathbf{K} = \begin{bmatrix} \mathbf{B} & \text{-}\mathbf{A} \\ \text{-}\mathbf{A} & \mathbf{B} \end{bmatrix} \qquad (2\mathrm{Nvib}\times 2\mathrm{Nvib}), \tag{2.199}$$

$$\mathbf{F} = \begin{bmatrix} \mathbf{D}^{\mathrm{T}}\mathbf{E}\mathbf{S} & \mathbf{D}^{\mathrm{T}}\mathbf{E}\mathbf{S} \end{bmatrix}^{\mathrm{T}} \qquad (2\mathrm{Nvib}\times 1), \tag{2.200}$$

where $\boldsymbol{\omega}_{\mathrm{i/f}}$ is the angular frequency of normal nodes at the initial/final state PES, $\mathbf{D}$ is the shift vector, and $\mathbf{S}$ is the Duschinsky matrix, respectively, and the size of each matrix is shown using the number of vibrational modes denoted as Nvib. Note that the prefactor in Eqn. 2.193 is a complex value since τ_{i} is a complex. In the implementation, this term must be handled very carefully. Then, correlation function of FC/HT and HT terms are,

$$\rho_k^{\mathrm{FC/HT}}(t,T) = -\rho^{\mathrm{FC}}(t,T)\left\{\left(\mathbf{H}_k^{\mathrm{FC/HT}}\right)^{\mathrm{T}}\mathbf{K}^{-1}\mathbf{F}\right\}, \tag{2.201}$$

$$\rho_k^{\mathrm{HT}}(t,T) = \rho^{\mathrm{FC}}(t,T)\left\{i\hbar\mathrm{Tr}\left[\mathbf{G}_{kl}^{\mathrm{HT}}\mathbf{K}^{-1}\right] + \left(\mathbf{K}^{-1}\mathbf{F}\right)^{\mathrm{T}}\mathbf{G}_{kl}^{\mathrm{HT}}\left(\mathbf{K}^{-1}\mathbf{F}\right)\right\}, \tag{2.202}$$

where the auxilialy matrices are given as,

$$H_k^{\mathrm{FC/HT}}{}_i = \delta_{ik} \qquad (2\mathrm{Nvib}\times 1), \tag{2.203}$$

$$G_{kl}^{\mathrm{FC/HT}}{}_{ij} = \delta_{ik}\delta_{j(l+\mathrm{Nvib})} \qquad (2\mathrm{Nvib}\times 2\mathrm{Nvib}). \tag{2.204}$$

These auxiliary matrices are so sparse that actual operation is simpler than Eqn. 2.201 or

2.202. The other correlation functions are given by,

$$\rho_{\mathrm{ic},kl}(t,T) = \quad \rho^{\mathrm{FC}}(t,T)\left\{i\hbar\mathrm{Tr}\left[\mathbf{G}^{\mathrm{ic}}_{kl}\mathbf{K}^{-1}\right] + \left(\mathbf{K}^{-1}\mathbf{F}\right)^{\mathrm{T}}\mathbf{G}^{\mathrm{ic}}_{kl}\left(\mathbf{K}^{-1}\mathbf{F}\right) - \left(\mathbf{H}^{\mathrm{ic}}_{kl}\right)^{\mathrm{T}}\left(\mathbf{K}^{-1}\mathbf{F}\right)\right\}, \tag{2.205}$$

$$\rho^{(1)}_{\mathrm{isc},k}(t,T) = -\rho^{\mathrm{FC}}(t,T)\left\{\left(\mathbf{H}^{\mathrm{isc}(1)}_{k}\right)^{\mathrm{T}}\mathbf{K}^{-1}\mathbf{F}\right\}, \tag{2.206}$$

where the auxilialy matrices are given as,

$$\mathbf{H}^{\mathrm{ic}}_{kl} = \begin{bmatrix} \mathbf{H}^{\mathrm{ic}}_{kl,1} \\ \mathbf{H}^{\mathrm{ic}}_{kl,2} \end{bmatrix} \quad (2\mathrm{Nvib}\times 1), \tag{2.207}$$

$$H^{\mathrm{ic}}_{kl,1_i} = \quad b_{\mathrm{fk}}\delta_{ki}\left(\mathbf{D}^{\mathrm{T}}\mathbf{ES}\right)_l \quad (\mathrm{Nvib}\times 1), \tag{2.208}$$

$$H^{\mathrm{ic}}_{kl,2_i} = -a_{\mathrm{fk}}\delta_{ki}\left(\mathbf{D}^{\mathrm{T}}\mathbf{ES}\right)_l \quad (\mathrm{Nvib}\times 1), \tag{2.209}$$

$$\mathbf{G}^{\mathrm{ic}}_{kl} = \begin{bmatrix} \mathbf{G}^{\mathrm{ic}}_{kl,11} & \mathbf{G}^{\mathrm{ic}}_{kl,12} \\ \mathbf{G}^{\mathrm{ic}}_{kl,21} & \mathbf{G}^{\mathrm{ic}}_{kl,22} \end{bmatrix} \quad (2\mathrm{Nvib}\times 2\mathrm{Nvib}), \tag{2.210}$$

$$G^{\mathrm{ic}}_{kl,11_{ij}} = -b_{\mathrm{fk}}\delta_{ki}\left(\mathbf{S}^{\mathrm{T}}\mathbf{a}_{\mathrm{i}}\mathbf{S}\right)_{lj} \quad (\mathrm{Nvib}\times\mathrm{Nvib}), \tag{2.211}$$

$$G^{\mathrm{ic}}_{kl,12_{ij}} = \quad b_{\mathrm{fk}}\delta_{ki}\left(\mathbf{S}^{\mathrm{T}}\mathbf{b}_{\mathrm{i}}\mathbf{S}\right)_{lj} \quad (\mathrm{Nvib}\times\mathrm{Nvib}), \tag{2.212}$$

$$G^{\mathrm{ic}}_{kl,21_{ij}} = \quad a_{\mathrm{fk}}\delta_{ki}\left(\mathbf{S}^{\mathrm{T}}\mathbf{a}_{\mathrm{i}}\mathbf{S}\right)_{lj} \quad (\mathrm{Nvib}\times\mathrm{Nvib}), \tag{2.213}$$

$$G^{\mathrm{ic}}_{kl,22_{ij}} = -a_{\mathrm{fk}}\delta_{ki}\left(\mathbf{S}^{\mathrm{T}}\mathbf{b}_{\mathrm{i}}\mathbf{S}\right)_{lj} \quad (\mathrm{Nvib}\times\mathrm{Nvib}), \tag{2.214}$$

$$\mathbf{H}^{\mathrm{isc}(1)}_{k} = \begin{bmatrix} \mathbf{H}^{\mathrm{isc}(1)}_{k,1} \\ \mathbf{H}^{\mathrm{isc}(1)}_{k,2} \end{bmatrix} \quad (2\mathrm{Nvib}\times 1), \tag{2.215}$$

$$H^{\mathrm{isc}(1)}_{k,1\ i} = b_{\mathrm{fk}}\delta_{ki} \quad (\mathrm{Nvib}\times 1), \tag{2.216}$$

$$H^{\mathrm{isc}(1)}_{k,1\ i} = -a_{\mathrm{fk}}\delta_{ki} \quad (\mathrm{Nvib}\times 1). \tag{2.217}$$

Again, these auxiliary matrices are so sparse that actual operation is simpler than Eqn. 2.201 or 2.202. To sum up, the analytical formulas of the correlation functions are given. It should be noteworthy that all formula contains $\rho^{\mathrm{FC}}(t,T)$ as a prefactor, resulting in the simpler calculation of correlation function at each time. Using Eqn. 2.94, 2.102, 2.105-2.108, 2.193, 2.201, and 2.202, absorption spectrum at the FCHT level including broadening effect is given as,[8,60]

$$\sigma^{\mathrm{FCHT}}_{\mathrm{abs}}(\omega) = \frac{2\pi\omega}{3\hbar c}\int dt\ e^{-i\omega t}e^{i\omega_{\mathrm{fi}}t}e^{-\frac{\sigma^2t^2}{2}}\frac{1}{Z_{\mathrm{i}}}\tilde{\mu}^2(t,T)\rho^{\mathrm{FC}}(t,T), \tag{2.218}$$

$$\begin{aligned}\tilde{\mu}^2(t,T) \equiv{}& \left|\vec{\mu}^{\mathrm{FC}}_{\mathrm{fi}}\right|^2 - \sum_k \vec{\mu}^{\mathrm{FC}}_{\mathrm{fi}}\cdot\vec{\mu}_k\left\{\left(\mathbf{H}^{\mathrm{FC/HT}}_{k}\right)^{\mathrm{T}}\mathbf{K}^{-1}\mathbf{F}\right\} \\ &+ \sum_{kl}\vec{\mu}_k\cdot\vec{\mu}_l\left\{i\hbar\mathrm{Tr}\left[\mathbf{G}^{\mathrm{HT}}_{kl}\mathbf{K}^{-1}\right] + \left(\mathbf{K}^{-1}\mathbf{F}\right)^{\mathrm{T}}\mathbf{G}^{\mathrm{HT}}_{kl}\left(\mathbf{K}^{-1}\mathbf{F}\right)\right\}.\end{aligned} \tag{2.219}$$

Eqn. 2.218 indicates that the Herzberg–Teller contribution can be treated by making μ time-dependent, and that only once of the Fourier transformation is required. Similarly, rate constant of internal conversion is given as,

$$\begin{aligned}k_{\mathrm{ic}} = {}& \frac{1}{\hbar^2}\int dt\ e^{-i\omega_{\mathrm{fi}}t}e^{-\frac{\sigma^2t^2}{2}}\frac{1}{Z_{\mathrm{i}}}\rho^{\mathrm{FC}}(t,T) \\ &\times\sum_{kl}R_{kl}\left\{i\hbar\mathrm{Tr}\left[\mathbf{G}^{\mathrm{ic}}_{kl}\mathbf{K}^{-1}\right] + \left(\mathbf{K}^{-1}\mathbf{F}\right)^{\mathrm{T}}\mathbf{G}^{\mathrm{ic}}_{kl}\left(\mathbf{K}^{-1}\mathbf{F}\right) - \left(\mathbf{H}^{\mathrm{ic}}_{kl}\right)^{\mathrm{T}}\left(\mathbf{K}^{-1}\mathbf{F}\right)\right\}.\end{aligned} \tag{2.220}$$

Rate constant of intersystem crossing from singlet to triplet state based on 2nd-order perturbation is given by,

$$\sum_{M}^{1,0,-1} k_{\mathrm{isc}}^{M} = \frac{1}{\hbar^2}\int dt\ e^{-i\omega_{\mathrm{fi}}t}e^{-\frac{\sigma^2 t^2}{2}}\frac{1}{Z_{\mathrm{i}}}\rho^{\mathrm{FC}}(t,T) \times\left[\sum_{M}\left|H_{\mathrm{fi}}^{\mathrm{SO},M,\mathrm{FC}}\right|^2+\sum_{k}\mathrm{Re}\left(\sum_{M}w_k^M\right)\left\{\left(\mathbf{H}_k^{\mathrm{isc}(1)}\right)^{\mathrm{T}}\mathbf{K}^{-1}\mathbf{F}\right\} +\sum_{kl}T_{kl}\left\{i\hbar\mathrm{Tr}\left[\mathbf{G}_{kl}^{\mathrm{ic}}\mathbf{K}^{-1}\right]+\left(\mathbf{K}^{-1}\mathbf{F}\right)^{\mathrm{T}}\mathbf{G}_{kl}^{\mathrm{ic}}\left(\mathbf{K}^{-1}\mathbf{F}\right)-\left(\mathbf{H}_{kl}^{\mathrm{ic}}\right)^{\mathrm{T}}\left(\mathbf{K}^{-1}\mathbf{F}\right)\right\}\right], \tag{2.221}$$

while Rate constant of intersystem crossing from singlet to triplet state at the FCHT level is,

$$\sum_{M}^{1,0,-1} k_{\mathrm{isc}}^{M,\mathrm{FCHT}} = \frac{1}{\hbar^2}\int dt\ e^{-i\omega_{\mathrm{fi}}t}e^{-\frac{\sigma^2 t^2}{2}}\frac{1}{Z_{\mathrm{i}}}\rho^{\mathrm{FC}}(t,T) \times\left[\sum_{M}\left|H_{\mathrm{fi}}^{\mathrm{SO},M,\mathrm{FC}}\right|^2-\sum_{k}\mathrm{Re}\left[\sum_{M}H_{\mathrm{fi}}^{\mathrm{SO},M,\mathrm{FC}*}H_{\mathrm{fi},k}^{\mathrm{SO},M}\right]\left\{\left(\mathbf{H}_k^{\mathrm{FC/HT}}\right)^{\mathrm{T}}\mathbf{K}^{-1}\mathbf{F}\right\} +\sum_{kl}\sum_{M}\left(H_{\mathrm{fi},k}^{\mathrm{SO},M*}H_{\mathrm{fi},l}^{\mathrm{SO},M}\right)\left\{i\hbar\mathrm{Tr}\left[\mathbf{G}_{kl}^{\mathrm{HT}}\mathbf{K}^{-1}\right]+\left(\mathbf{K}^{-1}\mathbf{F}\right)^{\mathrm{T}}\mathbf{G}_{kl}^{\mathrm{HT}}\left(\mathbf{K}^{-1}\mathbf{F}\right)\right\}\right]. \tag{2.222}$$

2.5.5 Implementation

Overview

I implemented a module for rate constant calculation based on correlation function formalism using Python 3. Numerical operation including matrix operation and discrete Fourier transformation is conducted using Numpy module.[10] In accordance with MOMAP,[8] three files are coded; one contains the main part, another is "evc.py" for handling data from QM calculations to obtain input for computing correlation function, and the other is "abs_ems.py" for computing correlation functions. The rate constant of radiative decay, internal conversion, and intersystem crossing can be estimated through my code; however, $\rho_{\mathrm{isc},k}^{(1)}(t,T)$ is NOT implemented, because this term vanishes in usual cases.

Molecular geometry, energy, gradient, nonadiabatic coupling, and Hessian at the initial/final states must be given in fchk format for my code. A tool for producing an fchk file using user-defined data is also coded. Change in the adiabatic energy can be defined by users; if not, adiabatic energy is computed from energies in the fchk files. Because the working equation in my code depends on the sign of adiabatic energy, users MUST be careful of the sign. Adiabatic energy in my code is defined as $E_{\mathrm{f}} - E_{\mathrm{i}}$ for any calculation types. Because the rate constant of internal conversion and intersystem crossing is very sensitive to the adiabatic energy, higher-level methods, such as domain-based local pair natural orbital similarity transformed equation of motion-coupled cluster singles and doubles (DLPNO-STEOM-CCSD)[76,92–94] may help with a reasonable estimation of the adiabatic energy.

The derivatives for computing the Herzberg–Teller terms can be obtained numerically (SOC) or analytically (transition dipole moment). The analytical derivative of the transition dipole moment can be obtained from the gaussian log file for TD-DFT calculation with "#p" and freq in the root section. A Python code to get the derivative from the gaussian log file was written (anal_tdip.py). As well as analytical one, some codes for performing numerical differentiation were coded. Because the sign of the term related to the transition density may be changed by the slight geometric change, that at the distorted geometry is chosen so that it resembles the term at the original geometry. To correctly differentiate the value, the terms should be extracted from the output file in an exponential format. Use "#p" for transition dipole by Gaussian 16, while "%tddft printlevel 3" for SOC by ORCA.

Users can choose the coordinate type (Cartesian or internal coordinate) and whether or not including vibrational mode-mixing. The exclusion of the mode-mixing is done by substituting a unit matrix as the Duschinsky matrix, which is called the adiabatic shift frequency model.[78] Conceptually, the use of internal coordinate and inclusion of mode-mixing is better.

The range of time for computing the correlation function must be chosen so that the correlation function reaches convergence. In the usual case, the maximum time of 1000 fs with dt of 0.01 fs may work well. In a difficult case, computation with the maximum time of 10000 fs with dt of 0.1 fs may be better. Now, I would like to recommend the latter setting, because the use of the small dt results in a wide range of the energy domain, while users may have interest on the small energy range. This selection of the time range is also affected by the magnitude of dephasing. Note that $\rho^{\mathrm{FC}}(t,T)$ is computed for $t = [0.5\times dt, t_{\max}+0.5\times dt]$ because $\mathbf{a}_{\mathrm{i/f}}$ diverges when $t = 0$. In addition, to reduce the computational cost, $\rho(t,T)$ at negative time is evaluated by,

$$\rho(-t,T) = \rho(t,T)^{*}. \tag{2.223}$$

This may cause problems when treating SOC with a specific M value.

Smoothening correlation function

Almost all of the equations I implemented was already shown above; the exception is the treatment of $\rho^{\mathrm{FC}}(t,T)$. As already written, the computation of $\rho^{\mathrm{FC}}(t,T)$ is numerically unstable,[62,65] probably due to the small vibrational partition function and small determinants. In addition, because $\rho^{\mathrm{FC}}(t,T)$ contains the square root of a complex value, its phase must be taken care of. Here, the detail of my treatment of $\rho^{\mathrm{FC}}(t,T)$ is shown.

Because the vibrational partition function and determinants in $\rho^{\mathrm{FC}}(t,T)$ (Eqn. 2.193) are small, not the values themselves but the logarithm of them are used. For example, the vibrational partition function of the silepin molecule (**noPh**) in this thesis has the order of 10^{-118}; division by such a small value is unfavorable. Considering the square-root in Eqn. 2.193 contains complex values, the logarithm of Eqn. 2.193 yields,

$$X = \left[\frac{1}{2}\mathbf{F}^{\mathrm{T}}\mathbf{K}^{-1}\mathbf{F} - \mathbf{D}^{\mathrm{T}}\mathbf{E}\mathbf{D}\right], \tag{2.224}$$

$$\det[\mathbf{Y}] = |\det[\mathbf{Y}]|\exp(i\theta_{\mathbf{Y}}), \tag{2.225}$$

$$\ln\left(\frac{\rho^{\mathrm{FC}}(t,T)}{Z_{\mathrm{i}}}\right) = -\ln(Z_{\mathrm{i}}) - \frac{i}{\hbar}\mathrm{Re}[X] + \frac{1}{\hbar}\mathrm{Im}[X] + \frac{\ln(|\det[\mathbf{a}_{\mathrm{i}}]|) + \ln(|\det[\mathbf{a}_{\mathrm{f}}]|) - \ln(|\det[\mathbf{K}]|)}{2} + \frac{\theta_{\mathbf{a}_{\mathrm{i}}} + \theta_{\mathbf{a}_{\mathrm{f}}} - \theta_{\mathbf{K}}}{2} i. \quad (2.226)$$

Then, the real and imaginary parts of Eqn. 2.226 are,

$$\mathrm{Re}\left[\ln\left(\frac{\rho^{\mathrm{FC}}(t,T)}{Z_{\mathrm{i}}}\right)\right] = \frac{\ln(|\det[\mathbf{a}_{\mathrm{i}}]|) + \ln(|\det[\mathbf{a}_{\mathrm{f}}]|) - \ln(|\det[\mathbf{K}]|) - 2\ln Z_{\mathrm{i}}}{2} + \frac{\mathrm{Im}[X]}{\hbar}, \quad (2.227)$$

$$\mathrm{Im}\left[\ln\left(\frac{\rho^{\mathrm{FC}}(t,T)}{Z_{\mathrm{i}}}\right)\right] = \frac{\theta_{\mathbf{a}_{\mathrm{i}}} + \theta_{\mathbf{a}_{\mathrm{f}}} - \theta_{\mathbf{K}}}{2} - \frac{\mathrm{Re}[X]}{\hbar}. \quad (2.228)$$

By using logarithm, division by an extremely small value was avoided. In addition, this manipulation is effective to treat the phase of $\rho^{\mathrm{FC}}(t,T)$. Because the angle of a complex is usually expressed by its principal value, the angle has a range ($\pi \leq \theta < \pi$). Similarly, the angle of $\det[\mathbf{a}_{\mathrm{f}}\mathbf{a}_{\mathrm{i}}] / \det[\mathbf{K}]$ should be a principal value, resulting in $-\pi \leq \theta_{\mathbf{a}_{\mathrm{i}}} + \theta_{\mathbf{a}_{\mathrm{f}}} - \theta_{\mathbf{K}} < \pi$. In this case, the square-root in Eqn. 2.193 causes,

$$-\frac{\pi}{2} \leq \frac{\theta_{\mathbf{a}_{\mathrm{i}}} + \theta_{\mathbf{a}_{\mathrm{f}}} - \theta_{\mathbf{K}}}{2} < \frac{\pi}{2}. \quad (2.229)$$

This range of angle causes discontinuity in $\rho^{\mathrm{FC}}(t,T)$. To make $\rho^{\mathrm{FC}}(t,T)$ smooth, this angle must be smoothened so that,[7]

$$-\pi \leq \frac{\theta_{\mathbf{a}_{\mathrm{i}}} + \theta_{\mathbf{a}_{\mathrm{f}}} - \theta_{\mathbf{K}}}{2} < \pi. \quad (2.230)$$

This comes from that the actual square-root of a complex is given as,

$$\sqrt{\exp(i\theta)} = \exp\left(i\frac{\theta + 2n\pi}{2}\right) \quad (n = 0, 1). \quad (2.231)$$

The proper square-root can be chosen by properly choosing n in Eqn. 2.231. In my implementation, to compute $\rho^{\mathrm{FC}}(t,T)$ in parallel, terms in Eqn. 2.227 and 2.228, instead of $\rho^{\mathrm{FC}}(t,T)$ itself, are computed at each time, then angle in Eqn. 2.229 is smoothened so as to satisfy Eqn. 2.230 by detecting its discontinuity. Finally, $\rho^{\mathrm{FC}}(t,T)$ is comuted as,

$$\frac{\rho^{\mathrm{FC}}(t,T)}{Z_{\mathrm{i}}} = \exp\left(\mathrm{Re}\left[\ln\left(\frac{\rho^{\mathrm{FC}}(t,T)}{Z_{\mathrm{i}}}\right)\right]\right)\exp\left(\mathrm{Im}\left[\ln\left(\frac{\rho^{\mathrm{FC}}(t,T)}{Z_{\mathrm{i}}}\right)\right]i\right). \quad (2.232)$$

In this way, $\rho^{\mathrm{FC}}(t,T)$ can be computed in parallel except for the part for smoothening the angle.

Validation of my code

I validated my code using data produced by MOMAP[8] and the β version of FCClasses 3.0.[7] First, through comparison of the fluorescence spectrum of azulene and corresponding correlation function computed using the Cartesian coordinate with those by MOMAP, the validity of $\rho^{\mathrm{FC}}(t,T)$ was checked. Then, the internal conversion rate of silepin molecules was compared with FCClasses to check $\rho_{\mathrm{ic},kl}(t,T)$. Finally, through comparison of the fluorescence spectrum of free-base porphyrin at the FCHT level, $\rho^{\mathrm{FC/HT}}(t,T)$ and $\rho^{\mathrm{HT}}(t,T)$ are checked.

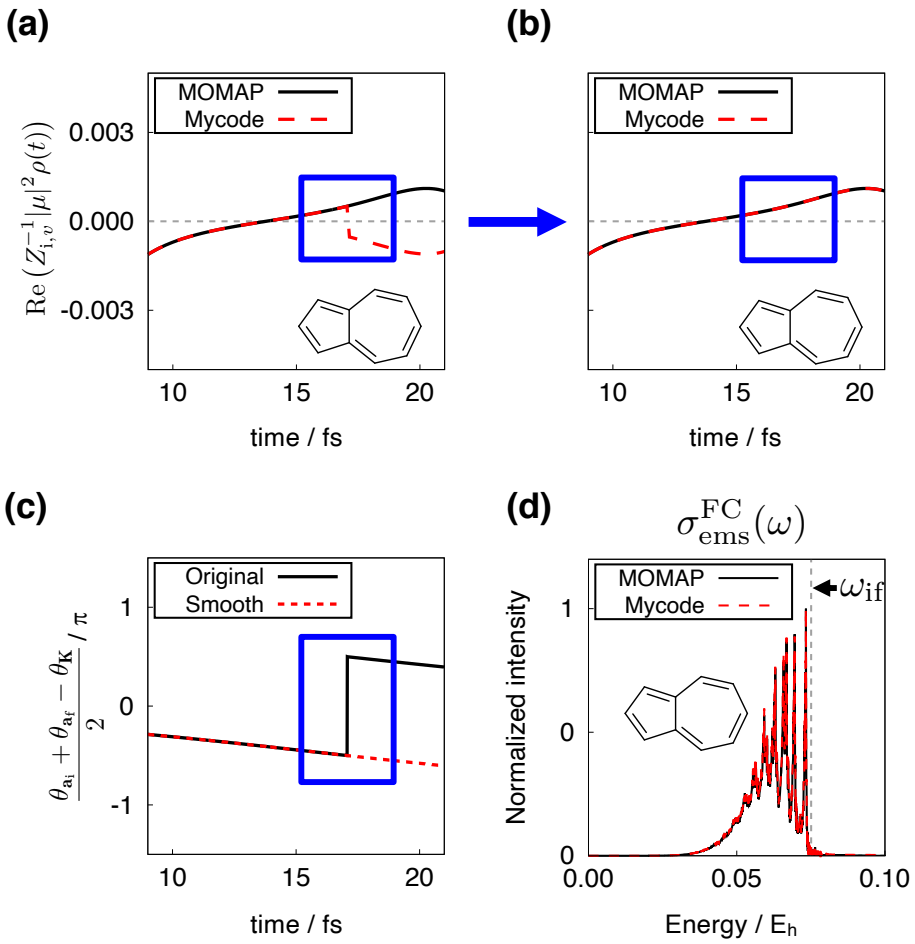

Fig. 2.2: Comparison of data concerning fluorescence of azulene at the Franck–Condon level using Cartesian coordinate produced by mycode with that by MOMAP. The real part of the correlation function without smoothening (a) and that with smoothening (b) are compared with MOMAP data. The change in angle by smoothening is shown in (c). The fluorescence spectrum produced by my code is compared with that by MOMAP in (d).

As the first validation, I tried computing the fluorescence spectrum of azulene molecule at the Franck–Condon level. Quantum chemical calculations were conducted using Gaussian 16 at the (TD-)B3LYP/6-31G(d) level of theory, which was determined in accordance with the tutorial of MOMAP program. The fluorescence spectrum was computed using the transition dipole moment at the Franck–Condon level computed at the geometry optimized at the S_1 state. The time for computing the correlation function was set to [0, 1000 fs] with a time step of 0.01 fs, where the time in my code was automatically changed to [0.005 fs, 1000.005 fs]. The correlation function was computed based on Cartesian coordinate without including any dephasing to the delta function. A temperature of 300 K and pressure of 1.0 atm were employed while the scaling factor for vibrational frequency was unused.

In Fig. 2.2, the fluorescence spectrum and its corresponding data computed by my code are compared with that by MOMAP. The correlation function in Fig. 2.2(a) shows a discontinuity at ca. 17 fs. At the same time step, the angle in Fig. 2.2(c) shows a jump by π, which should cause a discontinuity in the sign of the correlation function. By smoothening this angle as

shown in Fig. 2.2(c), the smooth correlation function was obtained (Fig. 2.2(b)). Finally, the fluorescence spectrum thus obtained was in good agreement with that by MOMAP. Therefore, I concluded that I successfully implemented the calculation of the correlation function at the Franck–Condon level based on Cartesian coordinate.

Next, I computed the rate constant of fluorescent decay of a silepin molecule (**noph**) to validate the treatment of the internal coordinate system. The quantum chemical method employed was TDA-CAM-B3LYP/cc-pVDZ, which was slightly different from that in chapter 3. Molecular geometry was optimized using Gaussian 16 to obtain the Hessians and nonadiabatic coupling. The fluorescence spectrum was computed using transition dipole moment at the Franck–Condon level computed at the geometry optimized at the S_1 state. The time for computing correlation function was set to [0, 1000 fs] with the time step of 0.01 fs for my code, while the time step for FCClasses was set to 0.1 fs for technical reasons. To avoid the computation of the correlation function at t=0, the actual time step in my code was automatically changed to [0.005 fs, 1000.005 fs], while that for FCClasses was [0.05 fs, 1000 fs]. The correlation function was computed based on the internal coordinates by including a Gaussian dephasing with its HWHM at 0.005 eV. A temperature of 300 K and pressure of 1.0 atm were employed while the scaling factor for vibrational frequency was unused.

In Fig. 2.3(a), the correlation function using the internal coordinates produced by my code was compared with that by fcclasses 3.0. The correlation function produced by my code is quite similar to that by FCClasses. Hence, the resulting spectrum Fig. 2.3(b) is also in good agreement with FCClasses. Then, the rate constant was computed to be 3.72×10^8 s^{-1} by both my code and FCClasses. Because of these good agreements with FCClasses 3.0, I concluded that I successfully implemented the treatment in internal coordinate thanks to the modules in PSI4.[6]

In Fig. 2.3(c), the comparison of the spectrum in the internal coordinate system with that in the Cartesian coordinates is provided. The spectrums indicate that the choice of the coordinate system largely affects the lineshape of the simulated spectrum. This difference in lineshape can be explained by the difference in shift vector and Duschinsky matrix. The dashed lines in Fig. 2.3(c) are computed without including the Duschinsky mode-mixing. Hence, the comparison between dashed lines reflects the difference in the shift vector. The shift of peak top against the onset is larger in the Cartesian coordinate system than in the internal coordinate one. This peak shift can be explained by the reorganization energy at the final state PES. Fig. 2.3(d) shows that the reorganization energy of **noPh** estimated using Cartesian coordinate is almost twice of that using internal coordinate. I think this overestimation comes from the difficulty in evaluating the change in internal coordinates based on Cartesian coordinates. The geometry of this silepin molecule at the excited state is clearly different from that at the ground state, where the angle between two benzene rings changes from 150° to 120° (for details, see Chapter 3). Because the normal modes for the change in angle or dihedral are expressed by tangental line in Cartesian coordinate, large distortions cannot be effectively expressed. As a result, the shift vector along the C-H stretching mode gave a non-negligible contribution to the reorganization energy (Fig. 2.3(d)).

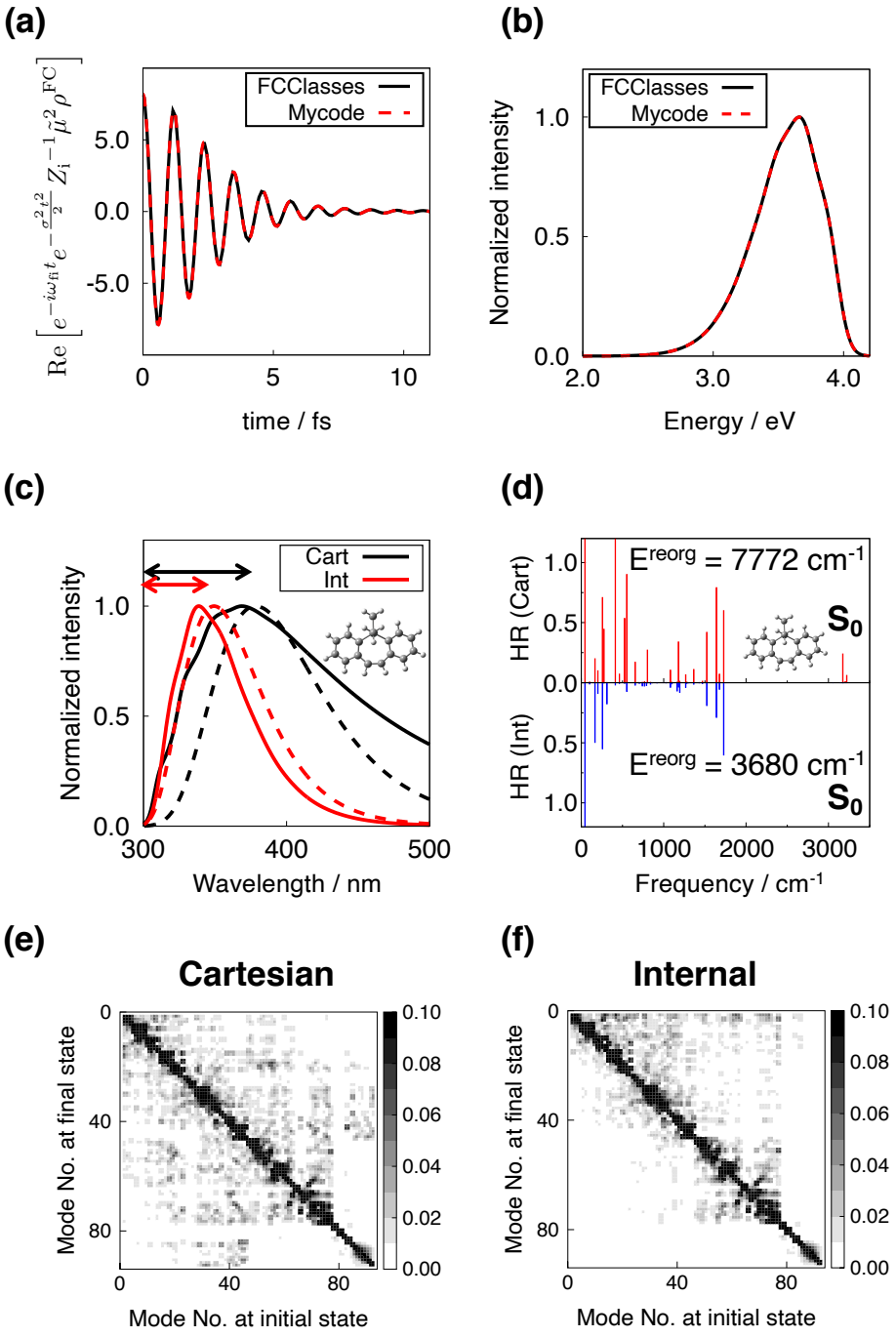

Fig. 2.3: Comparison of data concerning fluorescence of **noPh** at the Franck–Condon level. (a)Real part of the correlation function and (b)resulting fluorescence spectrum computed in internal coordinate system by my code are superposed on that by FCClasses 3.0. Fluorescence spectra computed in Cartesian (black) and internal coordinate (red) system are shown in (c), where solid lines were computed including vibrational mode-mixing, while dashed lines were without it. The Huang–Rhys factor and reorganization energy computed for the different coordinate systems are compared in (d). Discretized plots of the absolute value of the element of the Duschinsky matrix in (e)Cartesian and (f)internal coordinate systems are shown. To emphasize off-diagonal elements, the range for changing color was set to be [0.0, 0.10].

For other normal modes, Huang–Rhys factor is obviously different for the two coordinate systems.

A similar discussion can be applicable to the effect of the Duschinsky matrix. While the solid red line in Fig. 2.3(c) is somehow similar to the dashed red line, the solid black line is clearly different from the dashed black line. I think this black solid line is not reasonable because its lineshape is too broad. This strange lineshape reflects the poor performance of the Duschinsky matrix composed of normal modes in the questionable description in the Cartesian coordinate system. Absolute values of the Duschinsky matrices computed in the Cartesian and internal coordinate system are shown in Fig. 2.3(e) and (f). Obviously, the Duschinsky matrix based on internal coordinates is sparser than that based on Cartesian coordinates. Especially, the difference is located on off-diagonal elements related to modes with numbers larger than 80. Because the vibrational modes with numbers larger than 77 are assigned to be C-H stretching in this molecule, C-H stretching mode in Cartesian coordinate can be considered to be contaminated by other types of modes. Probably this is involved in the contribution of C-H stretching modes in Fig. 2.3(d). From these strange behaviors of Cartesian coordinate, I concluded that fluorescence spectrum should be computed based on internal coordinate if possible.

To check the validity of the correlation function for internal conversion, I computed the internal conversion rate constant of **noPh** at the same quantum mechanical calculation level. The nonadiabatic coupling employed was obtained from the fchk file produced by Gaussian 16, which is different from the scheme in MOMAP User guide. Other conditions were the same as those for the fluorescence spectrum.

In Fig. 2.4(a), the function to be Fourier transformed computed using internal coordinate by my code was compared with that by FCClasses. The function produced by my code is quite similar to that by FCClasses. Hence, the resulting k_{ic}-adiabatic energy plot (Fig. 2.4(b)) is also in good agreement with FCClasses. The internal conversion rate constant can be obtained by picking up the value with $E = |E_{\mathrm{f}} - E_{\mathrm{i}}|$. Because the adiabatic energy in this calculation was |-4.133| eV (gray dashed line in Fig. 2.4(b)), the rate constant was estimated to be 1.68×10^2 s^{-1} by both my code and FCClasses 3.0. Because of these good agreements with FCClasses 3.0, I concluded that I successfully implemented the computation of the internal conversion rate constant.

In Fig. 2.4(c), the comparison of k_{ic}-adiabatic energy plot in internal coordinate with that in Cartesian coordinate is provoded. As with the fluorescence spectrum, the choice of the coordinate system and Duschinsky mode-mixing largely affected the lineshape of the plot. While the computation based on internal coordinate gave a similar plot regardless of the Duschinsky mode-mixing, the Duschinsky mode-mixing drastically changed the plot computed in Cartesian coordinate. Even though input data is the same for all computations in Fig. 2.4(c), the resulting rate constant varies from 3.47×10^1 s^{-1} to 5.13×10^9 s^{-1}. Because of this numerical instability against the coordinate system, I concluded that the use of internal coordinates is highly recommended in the calculation of internal conversion rate constants.

In Fig. 2.4(d), nonadiabatic coupling along the normal modes at the final state PES is

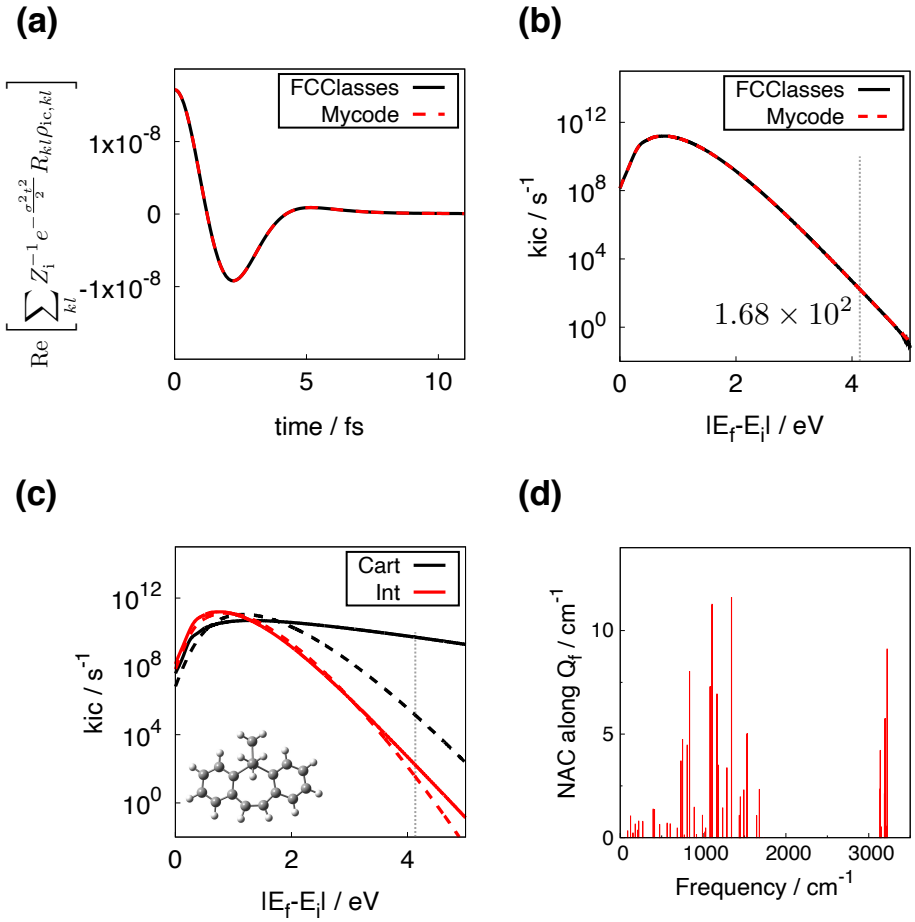

Fig. 2.4: Comparison of data concerning the internal conversion of **noPh**. (a)Real part of the function to be Fourier transformed and (b)resulting k_{ic}-adiabatic energy plot computed in internal coordinate system by my code are superposed on that by FCClasses 3.0. k_{ic}-adiabatic energy plot computed in Cartesian (black) and internal coordinate (red) system are shown in (c), where solid lines are computed including vibrational mode-mixing, while dashed lines without it. The nonadiabatic coupling along dimensionless normal mode at the initial state PES is shown (d).

shown. Because the normal modes has dimension of mass-weighted coordinate, nonadiabatic coulping along dimensionless normal modes[8,68] (nacm_lin in MOMAP) is employed; its mathmatical expression is given as,

$$\mathrm{NACME(lin)}_l \equiv \sqrt{\frac{\omega_l}{2\hbar}} \left| -\hbar^2 \left\langle \Phi_{\mathrm{f}} \left| \frac{\partial \Phi_{\mathrm{i}}}{\partial Q_l} \right\rangle \right| = \frac{\hbar\omega_l}{\sqrt{2}} \left| \left\langle \Phi_{\mathrm{f}} \left| \frac{\partial \Phi_{\mathrm{i}}}{\partial \sqrt{\frac{\omega_l}{\hbar}} Q_l} \right\rangle \right| , \tag{2.233}$$

where $\sqrt{\frac{\omega_l}{\hbar}} Q_l$ is the dimensionless normal mode. The NAC along normal modes is not so large; the maximum value is 11.6 cm^{-1} along the 62nd normal mode whose frequency is 1343 cm^{-1}.

To check the validity of the correlation function for the fluorescence spectrum at the FCHT level, I computed the fluorescence spectrum of free-base porphyrin (H_2P). This molecule was chosen as the test molecule in previous studies.[58,60] Quantum chemical calculations

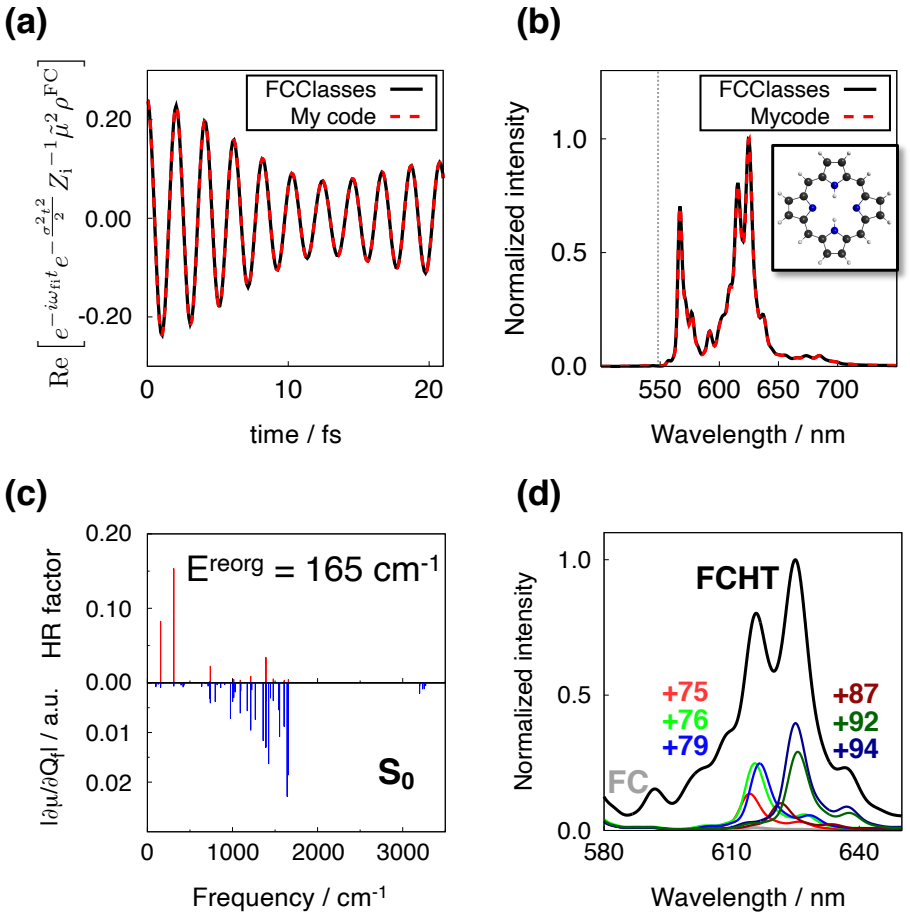

Fig. 2.5: Comparison of data related to the fluorescence of H_2P at the Franck–Condon and Herzberg–Teller (FCHT) level. (a)Real part of the function to be Fourier transformed and (b)resulting fluorescence spectrum computed in internal coordinate system by my code are superposed on that by FCClasses 3.0. The wavelength at the adiabatic energy was represented by the dashed gray line in (b). The structure of the H_2P molecule is depicted in (b). The Huang–Rhys factor, total reorganization energy, and the norm of the derivative of transition dipole moment along the normal modes at the final state PES are shown in (c). The contributions of the representative vibrational modes to the FCHT spectrum were shown in a range from 580 to 650 nm in (d).

were conducted using Gaussian 16 at the (TD-)B3LYP/6-31G(d) level of theory, which was determined in accordance with the tutorial of MOMAP program. Fluorescence spectrum was computed using transition dipole moment at the Franck–Condon and Herzberg-Teller level computed at the geometry optimized at the S_1 state. The derivative of transition dipole moment was obtained by numerical differentiation; to compute that I wrote a Python code. The time for computing correlation function was set to [0, 1000 fs] with the time step of 0.01 fs for my code, while the time step for FCClasses was set to 0.1 fs for technical reasons. To avoid the computation of the correlation function at t=0, the actual time step in my code was automatically changed to [0.005 fs, 1000.005 fs], while that for FCClasses was [0.05 fs, 1000 fs]. The option for dipole moment in FCClasses was set "HTf", while the derivative

employed was prepared around the geometry at the initial state. The correlation function was computed based on internal coordinate by including Gaussian dephasing with its HWHM of 0.005 eV. A temperature of 300 K and pressure of 1.0 atm were employed while the scaling factor for vibrational frequency was unused.

In Fig. 2.5(a), the function to be Fourier transformed computed using internal coordinate by my code was compared with that by FCClasses. Obviously, the function produced by my code is quite similar to that by FCClasses. Hence, the resulting fluorescence spectrum (Fig. 2.5(b)) is also in good agreement with FCClasses. The integration of this spectrum resulted in the radiative decay constant of 2.11×10^6 s^{-1} by my code, while 2.12×10^6 s^{-1} by FCClasses. Although the rate constant estimated by my code was slightly different from that by FCClasses, I concluded that I successfully implemented the computation of fluorescence spectrum at the FCHT level.

Because the fluorescence of H_2P is a weakly dipole-allowed transition, Herzberg–Teller term shows a large contribution.[58,60] Actually, the oscillator strength and norm of transition dipole moment at my computational condition were estimated to be 0.0012 and 0.148 a.u., respectively. The Huang–Rhys factor and total reorganization energy in Fig. 2.5(c) indicate that this free-base porphyrin is highly rigid in the S_1-S_0 transition. This means that vibronic transition enabled by transition dipole moment at the Franck–Condon level is dominated by 0-0 transition for vibrational modes with high frequency, because the vibrational overlap $\langle \Theta_{\mathrm{f}u} | \Theta_{\mathrm{i}v} \rangle$ becomes almost 0 for other transitions. This results in a small peak shift against the onset of the spectrum at the Franck–Condon level. The spectrum at the Franck–Condon level has a peak at 567 nm, which contributes to the peak at 567 nm at the FCHT level (Fig. 2.5(b)).

On the other hand, the vibrational overlap of Herzberg–Teller term is $\langle \Theta_{\mathrm{f}u} | Q_{\mathrm{f}k} | \Theta_{\mathrm{i}v} \rangle$. Because $Q_{\mathrm{f}k}$ is an odd function and the wavefunction of the vibrational ground state is even function, 0-0 transition is prohibited; instead, 0-1 transition is allowed. This means that the major vibrational state at the final state is the lowest excited state for mode $Q_{\mathrm{f}k}$ in contributing Herzberg–Teller term related to $Q_{\mathrm{f}k}$, resulting in the red-shift of spectrum by $\hbar\omega_{\mathrm{f}k}$. The fluorescence spectrum in Fig. 2.5(b) has two another peaks at 616 and 625 nm. The shift of these peaks from peak at 567 nm corresponds to 1399 and 1639 cm^{-1}, respectively, suggesting the contribution of vibrational modes with frequency in this area. Actually, the derivative of the transition dipole moment along modes with frequency of ca. 1400 cm^{-1} and ca. 1600 cm^{-1} have relatively large magnitude (Fig. 2.5(c)), where the former ones contain $\omega_{75} = 1360$, $\omega_{76} = 1393$, and $\omega_{79} = 1424$ cm^{-1}, while the latter ones contain $\omega_{87} = 1553$, $\omega_{92} = 1643$, and $\omega_{94} = 1656$ cm^{-1}. The contrubution of the derivative along these modes to the FCHT spectrum is shown in Fig. 2.5(d). The 76th and 79th modes turn out to contribute to the peak at 616 nm, whereas the 92nd and 94th modes contribute to the one at 625 nm. Similar analysis has already been provided in previous studies.[58,60]

Through these comparisons with MOMAP and FCClasses, I concluded that I successfully implemented the computation of correlation functions and the treatment for internal coordinates. The treatment for SOC has not been validated yet. Because the correlation functions

employed in the intersystem crossing were already checked, I think the rate constant of the intersystem crossings can be computed using my Python code.

Application to the rISC in an MR-TADF molecule

To check the performance of the intersystem crossing rate constant calculation, I computed the reverse intersystem crossing rate constant of DABNA,[95] which is known as an organic dye molecule with the multi-resonance type thermally activated delayed fluorescence (MR-TADF).

Organic dyes with the thermally activated decayed fluorescence were applied to the organic light-emitting diodes (OLEDs) by Adachi et al.[96] to improve the electroluminescence efficiency. There, the rate constant of the transition from the T_1 to S_1 state, i.e. the reverse intersystem crossing (rISC), affects the efficiency. To accelerate the rISC, the mechanism of the rISC have been intensively studied in recent years.[70,71,75,80,97–99]

Because DABNA is one of the characteristic TADF molecules, Kim et al. computed its rISC rate constant.[71] They applied the second-order formalism (Eqn. 2.122); there, they concluded that the T_1-T_3 non-Born–Oppenheimer coupling and T_3-S_1 SOCMEs mainly contributed to the rISC at its S-T gap region. On the other hand, the study including the Herzberg–Teller effect on SOCMEs of DABNA was not reported, to my knowledge. Here, I tried applying the method including HT effect (Eqn. 2.144) to DABNA.

The geometries and Hessians were computed at the TD-PBE0/6-31G(d) level, in accordance with the work by Penfold et al.[81] Note that Penfold et al. employed Q-Chem program, while I used Gaussian 16 program.[38] SOCMEs were computed at the ZORA-TD-PBE0/def2-TZVP level[100–102] with RI-SOMF(1X) Hamiltonian[103] using ORCA 5.0.2 program,[76] where resolution-of-identity approximation using SARC/J basis[104] to the Coulomb term and the chain-of-sphere exchange[105] to the exchange term were employed. The 1st-order derivatives of the SOCMEs were computed using numerical differentiation in the Cartesian space. To reliably estimate the S_1-T_1 gap, the DLPNO-STEOM-CCSD/def2-TZVP level[92–94] calculations were conducted at the optimized geometries at the TD-PBE0 level using ORCA 5.0.1 program.

I computed the rate constants of the fluorescent decay (k_r) and the T_1-S_1 rISC (k_risc), where the transition dipole moment and SOCMEs were both treated at the FCHT level. Both of the transition dipole moment and SOCMEs were expanded around the minimum of the initial state. The time for computing correlation function was set to [0.05, 10000.05 fs] with the time step of 0.1 fs. The correlation function was computed by using the shift vector and Duschinsky matrix in the internal coordinate space and including Gaussian dephasing with its HWHM at 0.005 eV. A temperature of 300 K and pressure of 1.0 atm were employed while the scaling factor for vibrational frequency was unused. The computed rate constants were compared with the result by Kim et al. and experimental data by Hatakeyama et al.

The natural transition orbitals(NTOs)[59] at the optimized S_1 and T_1 geometries were depicted in Fig. 2.6. Both of the S_1 and T_1 states were well characterized by the HOMO-LUMO transition, resulting in the similar highest occupied NTO (HONTO) and lowest unoccupied

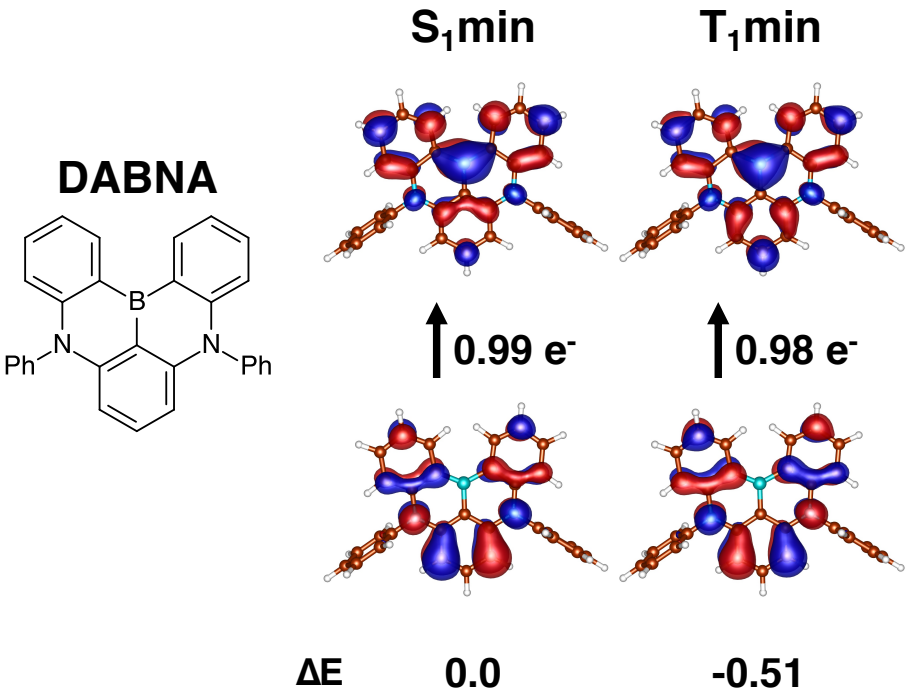

Fig. 2.6: The NTOs of DABNA for the S_1 and T_1 states at each optimized geometry. The figures at the lower and upper lines represent the HONTOs and LUNTOs, respectively. The eigenvalue of the transition from the HONTO to LUNTO was shown between them. The relative energy, i.e. S-T gap, was shown below the HONTOs in eV unit.

NTO (LUNTO) between them. This similarity in the excitation character resulted in the small SOCMEs in accordance with the El-Sayed rule, where the SOCME between the S_1 and T_1 states for spin-sublevel M=0 was predicted to be -0.040i cm^{-1}, while those for the other sublevels were less than 10^{-4} cm^{-1} at the minimum of the T_1 state. Hence, the intersystem crossing at the FC level should be ineffective; instead, higher-level treatment, such as the inclusion of the intermediate state or HT expansion of the SOCMEs, should be required.

To reliably estimate the relative energies, the STEOM-DLPNO-CCSD calculations were conducted at the TD-PBE0 level geometries. The $S_1 \rightarrow S_0$ and $S_1 \rightarrow T_1$ adiabatic energies and fluorescence and phosphorescence energies were compared in Table 2.1. In Ref. 95, the S-T gap was estimated to be 0.15 eV using the maxima of the fluorescence and phosphorescence spectra, although I guess the correct value was 0.14. Using the computed vertical energies instead of the maxima of the spectrum, the S-T gap was estimated to be 0.46 eV at the TD-PBE0 level. This overestimation of the S-T gap probably comes from the overestimation of the fluorescence energy. On the contrary, the DLPNO-STEOM-CCSD calculations at the same geometries predicted the S-T gap at 0.14 eV, which was in good agreement with the experimental value. However, the S-T gap employed in the rate constant calculation should be the adiabatic energy. The adiabatic S-T gap was predicted to be 0.51 eV at the TD-PBE0 level, while it was predicted to be 0.18 eV at the DLPNO-STEOM-CCSD level. The effect of the difference in the adiabatic S-T gap will be discussed later.

The computed rate constants were compared with the predicted value by Kim et al.[71]

Table 2.1: Comparison of the computationally estimated relative energies with experimentally estimated ones of DABNA in eV unit.

	PBE0[a]	STEOM[b]	Exp.[c]
$E(S_1\text{-}S_0)$	3.145[d]	2.923[d]	—
$E(S_1\text{-}T_1)$	0.507[d]	0.183[d]	—
E(Flu)	3.024[e]	2.799[e]	2.737
E(Pho)	2.568[e]	2.663[e]	2.594
E(Flu)-E(Pho)	0.456	0.136	0.143[f]

[a] Energies and geometries at the TD-PBE0/6-31G(d) level

[b] Geometries at the TD-PBE0/6-31G(d) level and energies at the DLPNO-STEOM-CCSD/cc-pVTZ level

[c] Taken from Ref. 95

[d] Adiabatic energy

[e] Vertical energy

[f] Estimation of S-T gap in Ref. 95

Table 2.2: Comparison of the computationally estimated rate constants with experimentally obtained ones of DABNA.

	PBE0[ab]	STEOM[bc]	Kim et al.[d]	Exp.[e]
k_r [s^{-1}]	6.9×10^7	5.4×10^7	—	9.6×10^7
k_risc [s^{-1}]	6.8×10^{-4}	5.9×10^3	1.05×10^4	9.9×10^3
E_{ST}[f] [eV]	0.507	0.183	0.144	—

[a] Energies and geometries at the TD-PBE0/6-31G(d) level

[b] SOCMEs at the ZORA-TD-PBE0/def2-TZVP level

[c] Geometries at the TD-PBE0/6-31G(d) level and energies at the DLPNO-STEOM-CCSD/cc-pVTZ level

[d] Taken from Ref. 71, where 2nd-order method was employed.

[e] Taken from Ref. 95

[f] Adiabatic energy

and experimentally observed value by Hatakeyama et al.[95] in Table 2.2 The predicted k_r were in good agreement with the experimentally obtained one regardless of the correction at the STEOM-DLPNO-CCSD level. On the contrary, the predicted k_risc turned out to be highly sensitive to the predicted adiabatic S-T gap. With the correction at the DLPNO-STEOM-CCSD level, the predicted k_risc at 5.9×10^3 s^{-1} was in good agreement with the experimentally obtained value at 9.9×10^3 s^{-1}. However, that without the correction was too small at 6.8×10^{-4} s^{-1}, indicating the importance of the reliable estimation of the S-T gap. Note that FC contribution with the adiabatic S-T gap at 0.183 eV was negligible; the

predicted value was 7.6×10^1 s^{-1}, which was less than 1% of the value at the FCHT level. This negligible contribution of the FC term indicated that inclusion of the higher-level term was essential, as pointed out by Kim et al. They reasonably predicted the k_{risc} using the 2nd-order perturbation formalism. On the contrary, my calculations suggested that the expansion of SOCMEs at the FCHT level also be able to reasonably predict it when the adiabatic S-T gap was reliably estimated.

Bibliography

[1] T. Shiozaki, W. Győrffy, P. Celani, and H.-J. Werner, J. Chem. Phys. **135**, 081106 (2011).

[2] T. Yanai et al., J. Chem. Theory Comput. **13**, 4829 (2017).

[3] J. W. Park and T. Shiozaki, J. Chem. Theory Comput. **13**, 2561 (2017).

[4] J. W. Park, R. Al-Saadon, N. E. Strand, and T. Shiozaki, J. Chem. Theory Comput. **15**, 4088 (2019).

[5] T. Shiozaki, WIREs Comput. Mol. Sci. **8**, e1331 (2018).

[6] D. G. A. Smith et al., J. Chem. Phys. **152**, 184108 (2020).

[7] *FCclasses 3.0 beta release*, http://www.pi.iccom.cnr.it/fcclasses.

[8] Y. Niu et al., Mol. Phys. **116**, 1078 (2018).

[9] J. R. Reimers, J. Chem. Phys. **115**, 9103 (2001).

[10] C. R. Harris et al., Nature **585**, 357 (2020).

[11] C. C. J. Roothaan, Rev. Mod. Phys. **23**, 69 (1951).

[12] A. Szabo and N. S. Ostlund, *Modern quantum chemistry: introduction to advanced electronic structure theory*, Courier Corporation, 2012.

[13] J. A. Pople, R. Seeger, and R. Krishnan, Int. J. Quantum Chem. **12**, 149 (1977).

[14] G. E. Scuseria, C. L. Janssen, and H. F. Schaefer Iii, J. Chem. Phys. **89**, 7382 (1988).

[15] B. O. Roos et al., Chem. Phys. **48**, 157 (1980).

[16] *QSimulate-QM. Quantum Simulation Technologies, Inc. 2020*, https://qsimulate.com/.

[17] T. Yanai, Y. Kurashige, D. Ghosh, and G. K.-L. Chan, Int. J. Quantum Chem. **109**, 2178 (2009).

[18] K. Andersson, P.-Å. Malmqvist, and B. O. Roos, J. Chem. Phys. **96**, 1218 (1992).

[19] K. Hirao, Chem. Phys. Lett. **190**, 374 (1992).

[20] C. Angeli, R. Cimiraglia, S. Evangelisti, T. Leininger, and J.-P. Malrieu, J. Chem. Phys. **114**, 10252 (2001).

[21] C. Angeli, R. Cimiraglia, and J.-P. Malrieu, Chem. Phys. Lett. **350**, 297 (2001).

[22] C. Angeli, R. Cimiraglia, and J.-P. Malrieu, J. Chem. Phys. **117**, 9138 (2002).

[23] J. Finley, P.-Å. Malmqvist, B. O. Roos, and L. Serrano-Andrés, Chem. Phys. Lett. **288**, 299 (1998).

[24] H. Nakano, J. Chem. Phys. **99**, 7983 (1993).

[25] C. Angeli, S. Borini, M. Cestari, and R. Cimiraglia, J. Chem. Phys. **121**, 4043 (2004).

[26] A. A. Granovsky, J. Chem. Phys. **134**, 214113 (2011).

[27] P. J. Knowles and H.-J. Werner, Theor. Chim. Acta **84**, 95 (1992).
[28] N. Forsberg and P.-Å. Malmqvist, Chem. Phys. Lett. **274**, 196 (1997).
[29] S. R. White, Phys. Rev. Lett. **69**, 2863 (1992).
[30] S. R. White, Phys. Rev. B **48**, 10345 (1993).
[31] D. Ghosh, J. Hachmann, T. Yanai, and G. K.-L. Chan, J. Chem. Phys. **128**, 144117 (2008).
[32] T. Yanai, Mol. Sci. **8**, A0069 (2014).
[33] K. Yamazaki, Monograph Series of Physical Chemistry **23** (2015).
[34] J. Nocedal and S. J. Wright, *Numerical optimization*, Springer Science & Business Media, second edition, 2006.
[35] A. Banerjee, N. Adams, J. Simons, and R. Shepard, J. Phys. Chem. **89**, 52 (1985).
[36] E. Besalú and J. M. Bofill, Theor. Chem. Acc. **100**, 265 (1998).
[37] H. B. Schlegel, J. Comput. Chem. **3**, 214 (1982).
[38] M. J. Frisch et al., Gaussian 16 Revision B.01, 2016, Gaussian Inc. Wallingford CT.
[39] S. Maeda, Lecture note at Nagoya University **1**, 1 (2018).
[40] C. Peng, P. Y. Ayala, H. B. Schlegel, and M. J. Frisch, J. Comput. Chem. **17**, 49 (1996).
[41] R. M. Badger, J. Chem. Phys. **2**, 128 (1934).
[42] T. H. Fischer and J. Almlof, J. Phys. Chem. **96**, 9768 (1992).
[43] V. Bakken and T. Helgaker, J. Chem. Phys. **117**, 9160 (2002).
[44] A. Baiardi, J. Bloino, and V. Barone, J. Chem. Phys. **144**, 084114 (2016).
[45] E. B. Wilson Jr, J. Chem. Phys. **9**, 76 (1941).
[46] P. Pulay and G. Fogarasi, J. Chem. Phys. **96**, 2856 (1992).
[47] H. B. Schlegel, Theor. Chim. Acta **66**, 333 (1984).
[48] S. Maeda, K. Ohno, and K. Morokuma, J. Chem. Theory Comput. **6**, 1538 (2010).
[49] T. W. Keal, A. Koslowski, and W. Thiel, Theor. Chem. Acc. **118**, 837 (2007).
[50] M. R. Manaa and D. R. Yarkony, The Journal of chemical physics **99**, 5251 (1993).
[51] Y. Nishimoto, Chem. Phys. Lett. **744**, 137219 (2020).
[52] S. Gozem et al., J. Chem. Theory Comput. **10**, 3074 (2014).
[53] C. Ciminelli, G. Granucci, and M. Persico, Chem.–Eur. J. **10**, 2327 (2004).
[54] M. J. Bearpark, M. A. Robb, and H. B. Schlegel, Chem. Phys. Lett. **223**, 269 (1994).
[55] F. Sicilia, L. Blancafort, M. J. Bearpark, and M. A. Robb, J. Chem. Theory Comput. **4**, 257 (2008).
[56] S. Ruiz-Barragan, M. A. Robb, and L. Blancafort, J. Chem. Theory Comput. **9**, 1433 (2013).
[57] Y. Harabuchi, T. Taketsugu, and S. Maeda, Chem. Phys. Lett. **674**, 141 (2017).
[58] F. Santoro, A. Lami, R. Improta, J. Bloino, and V. Barone, J. Chem. Phys. **128**, 224311 (2008).
[59] R. L. Martin, J. Chem. Phys. **118**, 4775 (2003).
[60] Y. Niu, Q. Peng, C. Deng, X. Gao, and Z. Shuai, J. Phys. Chem. A **114**, 7817 (2010).
[61] Q. Peng, Y. Niu, Q. Shi, X. Gao, and Z. Shuai, J. Chem. Theory Comput. **9**, 1132 (2013).

[62] A. Baiardi, J. Bloino, and V. Barone, J. Chem. Theory Comput. **9**, 4097 (2013).
[63] M. Etinski, J. Tatchen, and C. M. Marian, J. Chem. Phys. **134**, 154105 (2011).
[64] M. Etinski, V. Rai-Constapel, and C. M. Marian, J. Chem. Phys. **140**, 114104 (2014).
[65] B. de Souza, F. Neese, and R. Izsák, The Journal of chemical physics **148**, 034104 (2018).
[66] J. Cerezo and F. Santoro, J. Chem. Theory Comput. **12**, 4970 (2016).
[67] V. Barone, J. Bloino, M. Biczysko, and F. Santoro, J. Chem. Theory Comput. **5**, 540 (2009).
[68] S. Lin et al., Adv. Chem. Phys. **121**, 1 (2002).
[69] Y. Niu, Q. Peng, and Z. Shuai, Sci. China Ser. B-Chem. **51**, 1153 (2008).
[70] I. Kim et al., J. Chem. Theory Comput. **16**, 621 (2020).
[71] I. Kim et al., JACS Au **1**, 987 (2020).
[72] T. J. Penfold, E. Gindensperger, C. Daniel, and C. M. Marian, Chem. Rev. **118**, 6975 (2018).
[73] C. M. Marian, WIREs Comput. Mol. Sci. **2**, 187 (2012).
[74] R. R. Valiev, V. N. Cherepanov, R. T. Nasibullin, D. Sundholm, and T. Kurten, Phys. Chem. Chem. Phys. **21**, 18495 (2019).
[75] L. Lv, K. Yuan, T. Zhao, and Y. Wang, J. Mater. Chem. C **8**, 10369 (2020).
[76] F. Neese, F. Wennmohs, U. Becker, and C. Riplinger, J. Chem. Phys. **152**, 224108 (2020).
[77] F. Metz, S. Friedrich, and G. Hohlneicher, Chem. Phys. Lett. **16**, 353 (1972).
[78] A. Humeniuk et al., J. Chem. Phys. **152**, 054107 (2020).
[79] J. Cerezo, F. J. Avila Ferrer, G. Prampolini, and F. Santoro, J. Chem. Theory Comput. **11**, 5810 (2015).
[80] J. Gibson, A. P. Monkman, and T. J. Penfold, ChemPhysChem **17**, 2956 (2016).
[81] T. Northey and T. J. Penfold, Org. Electron. **59**, 45 (2018).
[82] J. W. Ochterski, help@gaussian.com (1999).
[83] J. W. Ochterski, Gaussian Inc **1**, 1 (2000).
[84] E. A. Coutsias, C. Seok, and K. A. Dill, J. Comput. Chem. **25**, 1849 (2004).
[85] G. R. Kneller, J. Comput. Chem. **26**, 1660 (2005).
[86] J. Baker, A. Kessi, and B. Delley, J. Chem. Phys. **105**, 192 (1996).
[87] J. Cerezo, J. Zuniga, A. Requena, F. J. Avila Ferrer, and F. Santoro, J. Chem. Theory Comput. **9**, 4947 (2013).
[88] J. von Cosel et al., J. Chem. Phys. **147**, 164116 (2017).
[89] Q. Peng, Y. Yi, Z. Shuai, and J. Shao, J. Am. Chem. Soc. **129**, 9333 (2007).
[90] R. Borrelli, A. Capobianco, and A. Peluso, J. Phys. Chem. A **116**, 9934 (2012).
[91] M. Ito, M. Sakai, N. Ando, and S. Yamaguchi, Angew. Chem. - Int. Ed. **60**, 21853 (2021).
[92] R. Berraud-Pache, F. Neese, G. Bistoni, and R. Izsák, J. Chem. Theory Comput. **16**, 564 (2019).
[93] A. Sirohiwal, R. Berraud-Pache, F. Neese, R. Izsak, and D. A. Pantazis, J. Phys. Chem.

B **124**, 8761 (2020).

[94] R. Izsák, Int. J. Quantum Chem. **121**, e26327 (2021).

[95] T. Hatakeyama et al., Adv. Mater. **28**, 2777 (2016).

[96] H. Uoyama, K. Goushi, K. Shizu, H. Nomura, and C. Adachi, Nature **492**, 234 (2012).

[97] S. Lin, Z. Pei, B. Zhang, H. Ma, and W. Liang, J. Phys. Chem. A **126**, 239 (2022).

[98] L. Wang, Q. Ou, Q. Peng, and Z. Shuai, J. Phys. Chem. A **125**, 1468 (2021).

[99] A. Rodriguez-Serrano, F. Dinkelbach, and C. M. Marian, Phys. Chem. Chem. Phys. **23**, 3668 (2021).

[100] E. v. Van Lenthe, J. Snijders, and E. Baerends, J. Chem. Phys. **105**, 6505 (1996).

[101] C. van Wüllen, J. Chem. Phys. **109**, 392 (1998).

[102] F. Weigend and R. Ahlrichs, Phys. Chem. Chem. Phys. **7**, 3297 (2005).

[103] F. Neese, J. Chem. Phys. **122**, 034107 (2005).

[104] F. Weigend, Phys. Chem. Chem. Phys. **8**, 1057 (2006).

[105] F. Neese, F. Wennmohs, A. Hansen, and U. Becker, Chem. Phys. **356**, 98 (2009).

Chapter 3

Theoretical Investigation of the Nonradiative Decay of Silepins

3.1 Introduction

Photochemical properties of organic π-conjugated molecules have been applied to a variety of uses, such as fluorescent probes,[1–3] UV protection,[4–7] and organic light-emitting diodes.[8–10] To tune their performance, a deep understanding of their properties associated with the electronic states can promote elaborate design of photofunctional molecules.[10–15] Their electronic-level details can be investigated by physical-chemical methods, including spectroscopic measurements and theoretical approaches based on quantum chemical calculations.

Toward the theory-based design of functional organic molecules, the theoretical prediction of fluorescence quantum yield (Φ_{F}) is one of the attractive capabilities of computational approaches.[16–18] The quantum yield can be calculated as $\Phi_{\mathrm{F}} = k_{\mathrm{r}}/(k_{\mathrm{r}} + k_{\mathrm{nr}})$, where k_{r} and k_{nr} are the radiative and nonradiative decay rate constants, respectively. The computation of k_{nr} is considered a challenging task and thus has received increasing attention. For molecules in which nonradiative decay is much slower than the thermal equilibration upon vibrational relaxation, which is often tens-of-picosecond scale phenomena,[19] nonradiative processes after the thermal equilibration are a central topic of research.

One such process is thermally activated decay via internal conversion at the conical intersection seam. Some earlier theoretical studies have discussed the rate constant via first-principles computations of the potential energy curves (PECs) and the activation energy necessary for reaching the minimal energy conical intersection (MECI) point via the transition state (TS).[16,17,20] In the computational estimation of the activation energy in the excited state, reliable treatment for characterizing the excited states and their energies is highly important. Additionally, the structural determination of MECI and TS on such reliable potential energy surfaces (PESs) is similarly critical.

Quantum chemical calculations based on time-dependent density functional theory (TD-DFT) have been extensively used to obtain absorption or emission energies and investigate PESs of the ground and excited states. When the activation barrier point is located near the

minimum of the fluorescent state, which is often of singly excited character, single-reference (SR) methods, including TD-DFT and the equation-of-motion coupled-cluster method with single and double excitations (EOM-CCSD), may produce a reliable description of the electronic states. However, a reliable description of the complicated electronic state near MECI geometry tends to require a multireference (MR) method, such as complete active space self-consistent field (CASSCF)[21] and subsequent second-order perturbation correction (CASPT2)[22] methods.[23] Moreover, the quasi-degeneracy of those electronic states requires extended quasi-degenerate perturbation treatment, such as extended multi-configuration quasi-degenerate perturbation theory at the second-order (XMCQDPT2)[24] or extended multistate complete active space second-order perturbation theory (XMS-CASPT2).[25] Some previous studies have employed these MR methods to compute phenomena involving MECIs.[20,26–29]

For structural determination, the gradient of energy with respect to nuclear coordinates plays a central role. Analytical gradient of linear response TD-DFT, spin-flip TD-DFT,[30,31] and CASSCF[32–34] have been widely used to obtain the characteristic geometries including MECI points. Then, the energy profiles between key geometries have been computed by using relaxed scan[35–37] or linearly interpolated internal coordinates (LIIC).[20,27,32,37,38] In several studies that used LIIC, the activation energy was estimated without geometry optimization of the TS. Although geometry optimization at the MR perturbation theory (PT) level may give a better description of the energy profile, the number of studies that have employed the gradient of MRPT is still limited.[39]

The size of π-conjugated molecules with potential use as organic dyes has also prevented the use of the MR method. Even the size of the stilbene skeleton, which is one of the basic π-conjugated skeletons containing 14 π electrons in 14 valence π orbitals, is located near the upper bound of the applicability of the conventional CASSCF method when all valence π orbitals in the π-conjugated skeleton are included in the active space. Moreover, quasi-degeneracy in the excited states of the π-conjugated skeleton[35,40] requires inclusion of several electronic states in the state-averaged (SA) CASSCF calculation to treat the electronic state of interest, which increases the computational cost. This means that MR calculations of realistic π-conjugated molecules for materials with an active space containing the entire valence π orbitals in the π skeleton have been rarely conducted.

In the last two decades, several low-scaling quantum chemical calculation methods have been developed. Among the SR methods, coupled-cluster methods based on pair natural orbitals, such as back-transformed pair natural orbital based similarity transformed equation-of-motion coupled-cluster singles and doubles (*bt*-PNO-STEOM-CCSD)[41,42] and domain-based pair natural orbital (DLPNO-) STEOM-CCSD[43–45] both exhibit high accuracy and applicability to larger molecules. Among the MR methods, introduction of a density matrix renormalization group (DMRG)[46,47] to the CASSCF method resulted in establishment of the DMRG-CASSCF method,[48,49] which enabled application to the system with a larger active space. Then, second-order perturbation theories based on the DMRG-CASSCF method, such as DMRG-CASPT2[50] and DMRG-NEVPT2,[51,52] were developed. Recently, a combination

of DMRG-CASSCF and quasi-degenerate PT of XMS-CASPT2 was established as DMRG-XMS-CASPT2.[53] These recent SR and MR methods have the potential for application to realistic π-conjugated molecules that are larger than the stilbene skeleton. Moreover, analytical gradients for MR-QDPT methods have been developed,[54–57] some of which are publically available.[54,55,58] The use of these gradients for geometry optimization may provide a better description of the energy profile.

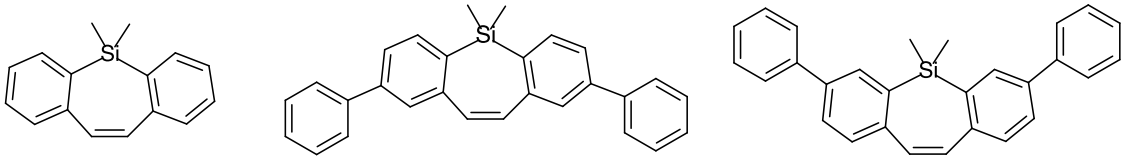

noPh (0.14) **p-Ph** (0.38) **m-Ph** (0.90)

Scheme 3.1: Chemical structures of **noPh**, ***p*-Ph**, and ***m*-Ph**. Their experimentally determined fluorescence quantum yields[59] are shown in parenthesis.

In this study, we applied SR and MRPT methods to thermally activated decay through the CI of an organic fluorescent molecule to determine the validity of the calculations. As molecules for computation, organic fluorescent 1,1-dimethyldibenzo[b,f]silepin derivatives **noPh**, ***p*-Ph** and ***m*-Ph** (Scheme Scheme 3.1) were chosen, whose fluorescence quantum yields were experimentally measured in ref. 59. k_{nr} of **noPh**, ***p*-Ph**, and ***m*-Ph** were also determined to be 57.3 $\times 10^8$ s^{-1}, 4.4 $\times 10^8$ s^{-1} and 0.63 $\times 10^8$ s^{-1}, respectively, which are directly related to the differences in their Φ_{F}. Because these nonradiative decays are much slower than thermal vibrational equilibration, their decay rate should be primarily determined by the energy barrier height in the reaction coordinate. Considering that these silepins have a *cis*-stilbene skeleton, which is known to undergo ultrafast decay through conical intersection triggered by the twisting of the central C-C bond in the excited state,[26,60] and that the $SiMe_2$-bridging may increase the energy to twist the central C-C bond by restricting the motion of the skeleton, decay through CI triggered by the twisting of the central C-C bond may act as the main nonradiative decay pathway of the silepins.

We first built a reaction coordinate by taking LIIC between the minimum of Franck-Condon state and the MECI point optimized by twisting the central C-C bond in the excited state. Then, single-point calculations on the coordinate of **noPh** at SR or MR level theories and the resultant PECs were compared to determine the validity of each method. Next, by comparing the PECs of **noPh**, ***p*-Ph**, and ***m*-Ph** at DMRG-XMS-CASPT2 level calculations with all valence π-orbitals and π-electrons in the active space, which were shown to be valid in this study, we confirmed whether there is any relationship between the experimentally determined fluorescence quantum yield and the computationally determined energy barrier height to reach MECI geometry of the silepins. Finally, the effect of geometry optimization of the TS at the MR-QDPT level was determined by comparing the PECs and estimated activation energy with/without the optimization. From these results, we confirmed that the main nonradiative

decay pathway of **noPh**, ***p*-Ph**, and ***m*-Ph** is thermally activated decay concerning the central C-C bond twisting, and geometry optimization of the TS using methods beyond TD-DFT, such as MR-QDPT methods, leads to a reasonable estimation of the activation energy.

3.2 Computational details

Quantum chemical calculation methods were used for investigating the molecular mechanism of the nonradiative decay of the photoexcited silepin derivatives and their electronic-level details. Below the computational setting and technical details of our quantum chemical approaches are presented.

3.2.1 Basis sets

Three kinds of basis sets were employed: (1) a mixture of the cc-pVDZ (for C and H) and cc-pV(D+d)Z (for Si) basis sets, hereafter referred to as CCD,[61–63] (2) its diffuse-basis augmented set consisting of aug-cc-pVDZ (for C and H) and aug-cc-pV(D+d)Z for Si, designated as ACCD,[62–64] and (3) the def2-SVP basis set.[65,66] To mitigate the high computational demands of XMS-CASPT2, DMRG-XMS-CASPT2, and *bt*-PNO-STEOM-CCSD calculations, we utilized the Resolution-of-Identity (RI) approximation technique to accelerate the two-electron integral evaluation. As the RI auxiliary basis sets, the def2-SVP/JK,[67] aug-cc-pVDZ/JK,[68] and aug-cc-pVDZ/C[69,70] basis were used for the XMS-CASPT2/def2-SVP, DMRG-XMS-CASPT2/ACCD, and *bt*-PNO-STEOM-CCSD/ACCD calculations, respectively.

3.2.2 Structural determinations at the DFT/TD-DFT level of theory

Throughout the quantum mechanical calculations, the silepin derivatives were each treated as an isolated molecule in the gas phase. In our model, with the silepin excited by photoabsorption, the excited molecule at the S_1 state nonradiatively decays at certain structures on the excited state PEC; thus, the determination of the PEC, which is calculated to be the energy of excited state as a function of the reaction coordinate, was an important task in this study. To deal with this, we first searched for the structures associated with the key steps of the decay process on the excited state PEC, which are schematically indicated as FC, Flu, TS, and Con in Fig. 3.1. The structure FC is defined as the minimum of the ground state (S_0) PEC, where the Franck-Condon transition to the excited state takes place. The minimum of the excited state PEC, denoted as Flu, is formed in the vicinity of FC by the structural relaxation, which is involved in the vibrational cooling in the excited electronic state. The fluorescence is emitted from this excited state with the Flu structure; thus, it is also referred to as the *fluorescent state*. With the progress of the twisting of the central C-C bond on the excited state PEC, there is assumed to be a MECI point between the ground and excited states, which corresponds to Con in Fig. 3.1. We examined the possibility of having

an energy barrier in PEC between Flu and Con that yields a TS; its structure corresponds to the TS in Fig. 3.1. The reaction coordinate in our model can thus be built upon the geometric parameters of Flu, TS, and Con. The geometry optimizations using the DFT/TD-DFT

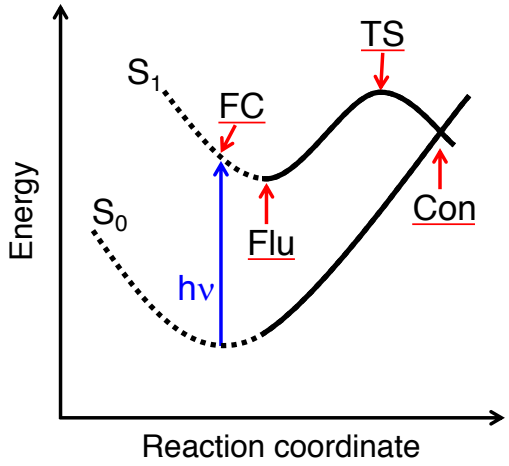

Fig. 3.1: Modeled potential energy curves (PECs) of the S_0 and S_1 states of silepins along the reaction coordinate of the radiative and nonradiative process. The area drawn by solid lines is primarily discussed.

methods were performed on the three silepin derivatives using the GAMESS 2012 program package.[71] The optimized structure of FC ($\mathbf{R}^{\mathrm{DFT}}$(FC)) was obtained by ground-state DFT calculations using the CAM-B3LYP[72] functional with the CCD basis, which is abbreviated as CAM-B3LYP/CCD. The geometries of Flu and Con, denoted as $\mathbf{R}^{\mathrm{DFT}}$(Flu) and $\mathbf{R}^{\mathrm{DFT}}$(Con), were determined at the TD-CAM-B3LYP/CCD level of theory with the Tamm-Dancoff approximation to TD's linear response treatment. The initial geometric parameters for the optimization of $\mathbf{R}^{\mathrm{DFT}}$(Con) were prepared by twisting the central C-C bond of $\mathbf{R}^{\mathrm{DFT}}$(Flu). The conical intersection search was conducted using the branching plane updating method.[73] The LIIC geometries linking $\mathbf{R}^{\mathrm{DFT}}$(Flu) and $\mathbf{R}^{\mathrm{DFT}}$(Con) were derived, resulting in a reaction coordinate set. The geometry of TS was chosen from PEC connecting $\mathbf{R}^{\mathrm{DFT}}$(Flu) and $\mathbf{R}^{\mathrm{DFT}}$(Con) as $\mathbf{R}^{\mathrm{DFT}}$(TS) without additional geometry optimization.

3.2.3 Excited state energy calculations along the DFT/TD-DFT level reaction coordinate

With the molecular geometries on the DFT/TD-DFT level reaction coordinate as written above, we performed single-point calculations on **noPh** using various quantum mechanical methods. A comparison of the resultant PECs allowed us to check the capability of the methods to properly describe the PECs of the radiative and nonradiative processes. We used TD-CAM-B3LYP/ACCD with/without the Tamm-Dancoff approximation level (TDA/TD), *bt*-PNO-STEOM-CCSD/ACCD level (STEOM), and 10SA-DMRG-XMS-CASPT2/ACCD level (XMS) methods to obtain the energies of the S_0 and S_1 states of **noPh** as a function of the reaction coordinate. The energy calculations for ***p*-Ph** and ***m*-Ph** along the reaction coordi-

nate were carried out only at the 10SA-DMRG-XMS-CASPT2/ACCD level of theory. The DMRG-XMS-CASPT2 and *bt*-PNO-STEOM-CCSD calculations were conducted using the ORZ program and ORCA 4.0.1.2 program package,[74] respectively, and the remaining calculations were performed using the Gaussian 16 Revision A.03 program package.[75] We used BLOCK 1.5[76] interfaced to ORZ for the DMRG calculations, which were performed by setting the number of spin-adapted renormalized basis states to 256. A variant of the CASPT2 treatment, referred to as the single-state single-reference (SS-SR) scheme,[55,77] was employed in conjunction with the extended multistate (XMS) formalism.[25,53] It is based on the zeroth-order Hamiltonian with the generalized Fock matrix constructed using state-specific density matrices. To circumvent intruder state problems in CASPT2, an IPEA shift of 0.25 a.u. and an imaginary level shift of 0.10 a.u. were employed. To avoid the high computational cost of handling a four-electron reduced density matrix (4-RDM), we used the cumulant approximation to it, with which 4-RDM can be decomposed into low-order RDMs of the DMRG wavefunctions.[78] The active spaces for the DMRG-CASSCF are composed of all valence π-orbitals and π-electrons, which corresponds to $(14e, 14o)$ for **noPh** and $(26e, 26o)$ for ***p*-Ph** and ***m*-Ph**, respectively. The localized molecular orbitals (LMOs) of these π-orbitals were employed as the DMRG correlation sites; Fig. 3.2 illustrates the LMOs of ***m*-Ph**. Among the S_1 state energies calculated on the PEC, the geometry that provides the highest energy is defined as $\mathbf{R}^{\mathrm{DFT}}$(TS), and this energy is used to estimate the activation energy.

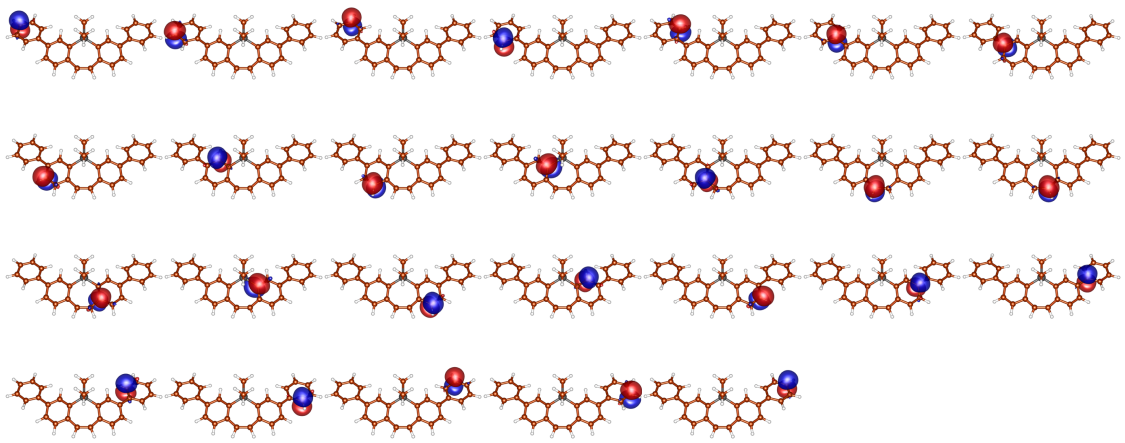

Fig. 3.2: Localized molecular orbitals used for the active space of the DMRG-XMS-CASPT2 calculation for ***m*-Ph** at $\mathbf{R}^{\mathrm{DFT}}$(Flu).

3.2.4 Geometry optimization with XMS-CASPT2 theory

As described above, the optimized geometries on the excited state PEC were obtained using the TD-DFT method. The adequacy of the TD-DFT treatment should be checked in particular for the intermediate TS structure, which is considered to often involve the MR nature of the wavefunction associated with quasi-degenerate orbital characters. Additionally,

neglecting the optimization of TS described above may lower the reliability of the activation energy. To assess the structures determined at the TD-DFT level, we again performed geometry optimizations on **noPh** at the MR level of theory using XMS-CASPT2 and its analytic nuclear derivative methods implemented in the BAGEL program.[58] This test serves as a way to highlight the effect of the level of theory on the structural determination for the TS and the related activation energy. The reference states for XMS-CASPT2 were set up with the SA-CASSCF method considering six states using $(10e, 10o)$ for the active space, which was derived by excluding the lowest and highest energy π-orbitals from the previously used CAS$(14e, 14o)$. The SS-SR contraction scheme of the XMS-CASPT2 treatment was used in conjunction with the real level shift of 0.3 a.u. to handle the intruder state problems and without the IPEA shift. With BAGEL, the Hessian matrices required for the TS geometry search were computed using the numerical differentiation method based on the central difference formula using the analytic XMS-CASPT2 energy gradients. The search for MECI geometry was performed using analytical derivative coupling of the XMS-CASPT2 method.[79]

We used the TD-DFT optimized structures as the starting geometric parameters to obtain the XMS-CASPT2 geometries for Flu, TS, and Con (see also Fig. 3.1), denoted as $\mathbf{R}^{\mathrm{XMS}}$(Flu), $\mathbf{R}^{\mathrm{XMS}}$(TS), and $\mathbf{R}^{\mathrm{XMS}}$(Con), respectively. The LIIC was formed by connecting $\mathbf{R}^{\mathrm{XMS}}$(Flu), $\mathbf{R}^{\mathrm{XMS}}$(TS), and $\mathbf{R}^{\mathrm{XMS}}$(Con), resulting in an alternative set of reaction coordinate geometries. On these geometries, the PEC calculations were conducted at the 10SA-DMRG-XMS-CASPT2/ACCD level of theory. Further, we attempted to re-optimize the geometry of TS for ***p*-Ph** and ***m*-Ph** at the XMS-CASPT2 level; however, the cost of obtaining the numerical Hessian matrix turned out to be exceedingly demanding and thus prevented us from achieving the optimized TS structure. Instead, the initial geometry was prepared by adding phenyl rings to the $\mathbf{R}^{\mathrm{XMS}}$(TS) of **noPh**. Then, the structural relaxation was accounted for at the TD-CAM-B3LYP/def2-SVP level of theory by constrained optimization with the skeleton of **noPh** fixed at the TS geometry determined at the XMS-CASPT2 level. The resultant geometry was denoted as $\mathbf{R}_c^{\mathrm{XMS}}$(TS). Geometry optimization in the fluorescent state was also conducted in a similar manner to obtain $\mathbf{R}_c^{\mathrm{XMS}}$(Flu). In addition, fully relaxed geometry optimization without the constraint was conducted, leading to the geometry denoted as $\mathbf{R}_r^{\mathrm{XMS}}$(Flu). The geometry search for the MECI point of ***p*-Ph** and ***m*-Ph** was not conducted at the XMS-CASPT2 level.

3.3 Results and discussion

3.3.1 Geometries obtained by TD-DFT level optimization

The geometries of **noPh** optimized at the DFT/TD-DFT level are shown in Fig. 3.3. The angles between two benzene rings in $\mathbf{R}^{\mathrm{DFT}}$(FC) and $\mathbf{R}^{\mathrm{DFT}}$(Flu) were estimated as 130° and 158°, respectively, which indicated that the stilbene skeleton became more planar in the geometry relaxation after photo-excitation. In this relaxation, the central C-C bond of the skeleton kept its planarity as dihedral C4-C3-C1-C2 retained its -180°. On the other hand,

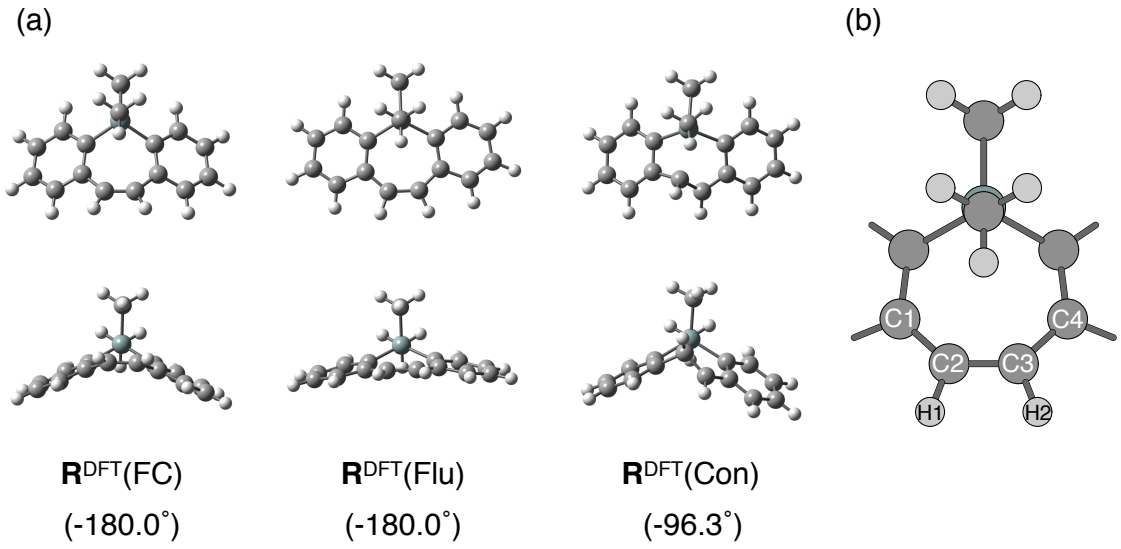

Fig. 3.3: (a) Optimized geometries of **noPh** and (b) atom labeling of the central 7-membered ring of the silepins. In (a), $\mathbf{R}^{\mathrm{DFT}}$(FC), $\mathbf{R}^{\mathrm{DFT}}$(Flu), and $\mathbf{R}^{\mathrm{DFT}}$(Con) represent the geometries optimized for the ground state, fluorescent state, and MECI point, respectively. The images show the top (upper line) and side (lower line) views of each geometry. The dihedral angle of C4-C3-C1-C2 defined in (b) is shown in parenthesis.

in the change from $\mathbf{R}^{\mathrm{DFT}}$(Flu) to $\mathbf{R}^{\mathrm{DFT}}$(Con), the stilbene skeleton lost its planarity with the change in dihedral C4-C3-C1-C2 from -180.0° to -96.3°; this dihedral was used to plot all PECs in this study. C2 in $\mathbf{R}^{\mathrm{DFT}}$(Con) showed a pyramidal structure, which is seen in the CI point of ethylene or stilbene.[26,79,80]

3.3.2 Validity of the DMRG-XMS-CASPT2 calculations

To check the validity of the DMRG-XMS-CASPT2 calculation, we computed the absorption and fluorescence energy of each silepin via the TDA and XMS calculations (Table 3.1). TDA and XMS gave similar results, and the XMS results were slightly closer to the experimental data. The maximum error in the estimation of fluorescence energy was 0.3 eV, which was smaller than that of the absorption energy. However, as shown in Table 3.1, the substituent dependence of Stokes shift was poorly predicted by DMRG-CASTP2. This may indicate the inadequacy of perturbative approaches in capturing the substituent effects in the Stokes shift. Because the main focus of this study was on the region from $\mathbf{R}^{\mathrm{DFT}}$(Flu) to $\mathbf{R}^{\mathrm{DFT}}$(Con), and the computed fluorescence energies reproduced the trend of experimentally obtained ones, we decided to conduct the XMS level calculations to describe the excited state wavefunction.

To analyze the effect of perturbative correction in the DMRG-XMS-CASPT2 calculation at $\mathbf{R}^{\mathrm{DFT}}$(Flu), the XMS-CASPT2 rotation matrix ($\mathbf{U}$) was analyzed, as shown in Table 3.2. Because the contribution of perturbative correction depends on the CASSCF eigenstate to be corrected, the order of the electronic state in XMS-CASPT2 may differ from that in CASSCF. Here, term U_{LM} represents the contribution of the S_L DMRG-CASSCF eigenstate to the S_M DMRG-XMS-CASPT2 wavefunction. For the fluorescent S_1 state at the DMRG-

Table 3.1: Absorption and fluorescence energies, and Stokes shift of **noPh**, ***p*-Ph**, and ***m*-Ph** in eV units

	E_{abs} [eV]			E_{flu} [eV]			Shift [eV]		
Name	TDA[a]	XMS[b]	exp.[c]	TDA[a]	XMS[b]	exp.[c]	TDA[a]	XMS[b]	exp.[c]
noPh	4.60	4.49	4.23	3.65	3.54	3.45	0.95	0.95	0.78
***p*-Ph**	4.55	4.49	4.07	3.60	3.52	3.34	0.95	0.97	0.72
***m*-Ph**	4.16	4.14	3.80	3.21	3.21	3.00	0.95	0.93	0.80

[a] TD-CAM-B3LYP/ACCD level under the Tamm-Dancoff approximation

[b] 10SA-DMRG-XMS-CASPT2/ACCD level

[c] peak top of experimentally obtained spectra of CH_2Cl_2 solution[59]

XMS-CASPT2 level, the most important DMRG-CASSCF eigenstate was the S_5 state for **noPh**, whereas it was the S_7 state for ***p*-Ph** and ***m*-Ph**. This indicated that perturbative correction can drastically change the order of the DMRG-CASSCF eigenstates and that the inclusion of a proper number of DMRG-CASSCF eigenstates is essential to handle the excited electronic state of interest.

Table 3.2: Characteristic elements in the second column of the XMS-CASPT2 rotation matrix obtained by fluorescence energy calculations of **noPh**, ***p*-Ph**, and ***m*-Ph** [a b c]

noPh	***p*-Ph**	***m*-Ph**
U_{51}(-0.810)	U_{71}(0.853)	U_{71}(-0.954)
U_{41}(-0.525)	U_{61}(0.466)	U_{31}(-0.260)
U_{21}(0.247)	U_{21}(0.233)	U_{41}(-0.125)

[a] Elements in the second column show the contribution to the S_1 state at the XMS-CASPT2 level.

[b] Elements with absolute values of more than 0.100 are shown.

[c] The values of the elements are shown in the parentheses.

3.3.3 PECs of noPh at several quantum chemical calculation methods

To determine the validity of the quantum mechanical calculation methods, we compared the PECs computed at the TDA, TD, STEOM, and XMS levels of theory along the LIIC between $\mathbf{R}^{\mathrm{DFT}}$(Flu) and $\mathbf{R}^{\mathrm{DFT}}$(Con), as depicted in Fig. 3.4. The computed PECs differed in the region around the TS in the S_1 state and the area close to $\mathbf{R}^{\mathrm{DFT}}$(Con). The dihedral C3-C2-C4-C1 of the TS estimated by TD-DFT calculations was -111°, which was apparently different from that by STEOM (-124°) and XMS (-126°). This result indicated that the geometry optimization of the TS via the TD-DFT level calculation is inadequate for estimation of the

activation energy of **noPh** by single-point calculations at the STEOM or XMS level.

In the estimation of activation energy ($\Delta E^{\ddagger}$), we defined it as the difference between the highest S_1 state energy in PEC and the S_1 state energy at $\mathbf{R}^{\mathrm{DFT}}$(Flu). The $\Delta E^{\ddagger}$ from the XMS and STEOM calculations were estimated at 15.8 and 14.8 kcal/mol, respectively, whereas those from the TDA and TD calculations were estimated at 24.5 and 19.5 kcal/mol, respectively, which were larger than those determined from the XMS and STEOM calculations. As well as the dihedral C3-C2-C4-C1 of the TS geometry, the activation energy estimated from the TD-DFT calculations apparently differed from that via the STEOM or XMS level calculations.

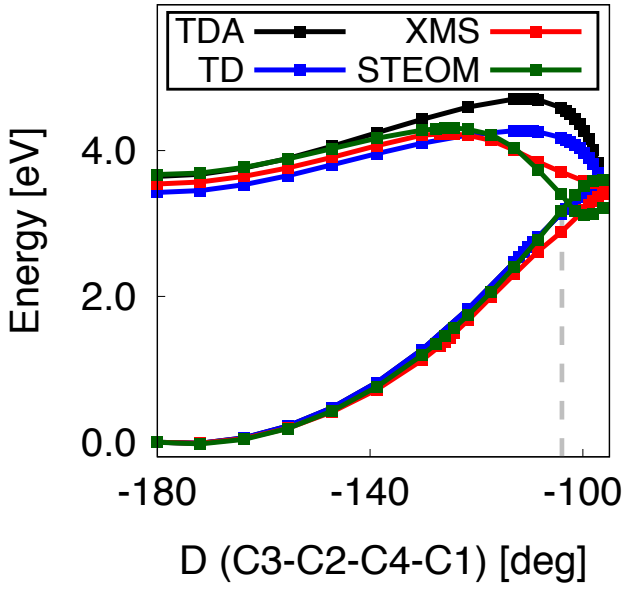

Fig. 3.4: Computed potential energy curves of the S_0 and S_1 state of **noPh**. Black, blue, red, and green lines show the curve given by TDA, TD, XMS, and STEOM level calculations, respectively. The energy values for plotting are given by the difference from that of the S_0 state at $\mathbf{R}^{\mathrm{DFT}}$(Flu). The gray dashed line represents the geometry denoted as $\mathbf{R}^{\mathrm{DFT}}$(D104), whose DMRG-CASSCF natural orbitals will be discussed later.

To elucidate the origin of the difference in PECs, we checked which DMRG-CASSCF eigenstate mainly contributed to the S_1 state at the DMRG-XMS-CASPT2 level. The weight of the DMRG-CASSCF eigenstate on the S_1 state at the DMRG-XMS-CASPT2 level was shown as a function along the LIIC in Fig. 3.5(a). At the $\mathbf{R}^{\mathrm{DFT}}$(Flu), where the dihedral C4-C3-C1-C2 is -180°, the DMRG-CASSCF S_4 and S_5 states showed large contributions. Contribution of the DMRG-CASSCF S_4 state there was probably due to the degeneracy of the DMRG-CASSCF eigenstates; the diagonalization of the multi-state Fock matrix to produce the reference states in the XMS-CASPT2 treatment mixed these DMRG-CASSCF eigenstates. In the region where the dihedral C4-C3-C1-C2 is smaller than 120°, the DMRG-CASSCF S_5 eigenstate showed the largest contribution to the DMRG-XMS-CASPT2 S_1 state. In the region where the dihedral C4-C3-C1-C2 is larger than that at the $\mathbf{R}^{\mathrm{DFT}}$(TS), the contribution of the DMRG-CASSCF S_5 eigenstate drastically decreased; instead, the contribution of the

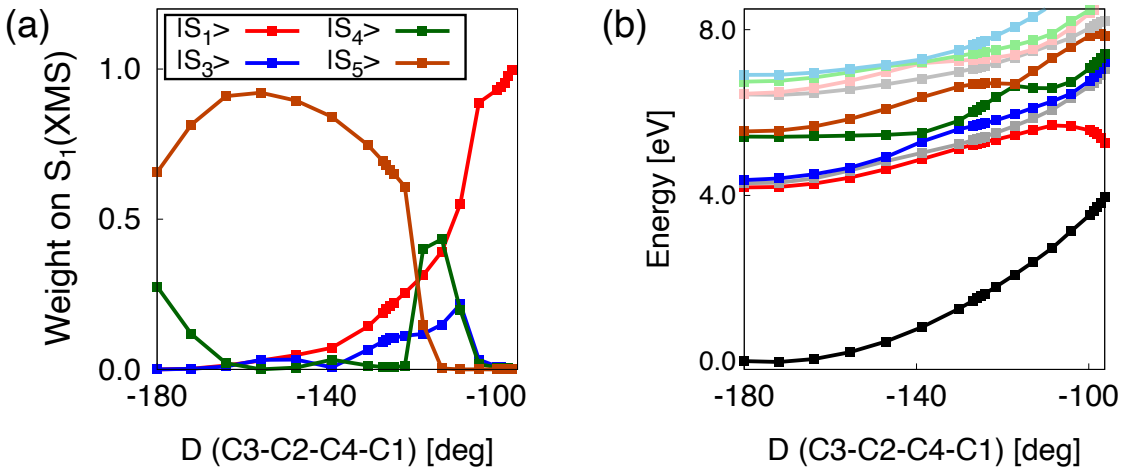

Fig. 3.5: (a) Contribution of the DMRG-CASSCF eigenstates to the S_1 state in the DMRG-XMS-CASPT2 calculations and (b) energies of the DMRG-CASSCF eigenstates along the LIIC linking $\mathbf{R}^{\mathrm{DFT}}$(Flu) and $\mathbf{R}^{\mathrm{DFT}}$(Con). In (a), contributions of the DMRG-CASSCF eigenstates which show more than 10 % contribution to the S_1 state at least at one geometry are shown. Contribution to the S_1 state was estimated by the square of the elements in the XMS-CASPT2 rotation matrix at each gometry. In (b), 10 lowest singlet eigenstates are shown.

DMRG-CASSCF S_4 state becomes large. This may come from the change in the ordering of S_4 and S_5 states as shown in Figure Fig. 3.5(b). Finally, in the area between $\mathbf{R}^{\mathrm{DFT}}$(D104) and $\mathbf{R}^{\mathrm{DFT}}$(CI), the DMRG-CASSCF S_1 eigenstate shows the largest contribution to the DMRG-XMS-CASPT2 S_1 state. These weights on the DMRG-XMS-CASPT2 S_1 state indicated that the important DMRG-CASSCF eigenstate gradually changed along the LIIC.

To analyze the character of the important DMRG-CASSCF eigenstates, we compared the DMRG-CASSCF natural orbitals at $\mathbf{R}^{\mathrm{DFT}}$(D104), which was the geometry with dihedral C3-C2-C4-C1 at -104.1° in LIIC between $\mathbf{R}^{\mathrm{DFT}}$(Flu) and $\mathbf{R}^{\mathrm{DFT}}$(Con), with those at the $\mathbf{R}^{\mathrm{DFT}}$(Flu). CASSCF natural orbitals are molecular orbitals obtained by diagonalizing the one-particle reduced density matrix of each CASSCF eigenstate, whose eigenvalues are the occupation number of electrons.

For the DMRG-CASSCF eigenstates with major contribution to the S_0 and S_1 states in the XMS-CASPT2 wavefunction at $\mathbf{R}^{\mathrm{DFT}}$(Flu) and $\mathbf{R}^{\mathrm{DFT}}$(D104), two DMRG-CASSCF natural orbitals whose occupation number is closest to 1.0 are depicted in Fig. 3.6. The character of the CASSCF S_0 state at $\mathbf{R}^{\mathrm{DFT}}$(Flu) is closed-shell because all occupation numbers are smaller than 0.2 or larger than 1.8. On the other hand, the CASSCF S_5 state there has two eigenvalues close to 1.0 because this state is mainly described by a singly excited configuration, which was assigned as a HOMO-LUMO excitation.

In contrast to $\mathbf{R}^{\mathrm{DFT}}$(Flu), the S_0 state at $\mathbf{R}^{\mathrm{DFT}}$(D104) has an open-shell (or biradical) character, whereas the character of S_1 state is closed-shell. Actually, the T_1 diagnostic[81] in the S_0 state DLPNO-CCSD calculations exceeded 0.02 at the geometry near $\mathbf{R}^{\mathrm{DFT}}$(D104).

This indicated that the S_0 state has a multi-configurational character. The difference in the S_0 state PECs may originate from the DLPNO-CCSD and DFT methods, which are categorized as SR methods and cannot reasonably describe multi-configurational S_0 states. The reason why the TD-DFT level S_1 state PEC differs from the XMS level one may be that expansion of the excited state wavefunction by singly excited determinants in the TD-DFT method cannot describe the closed-shell S_1 state. Considering that the S_1 state at $\mathbf{R}^{\mathrm{DFT}}$(TS) may be characterized as a mixture of that at $\mathbf{R}^{\mathrm{DFT}}$(Flu) and $\mathbf{R}^{\mathrm{DFT}}$(Con), the lack of doubly excited configurations in TD-DFT methods leads to poor estimation of $\mathbf{R}^{\mathrm{DFT}}$(TS).

From the results above, we concluded that a reasonable description of the entire PEC in this study requires MR-QDPT methods, such as DMRG-XMS-CASPT2.

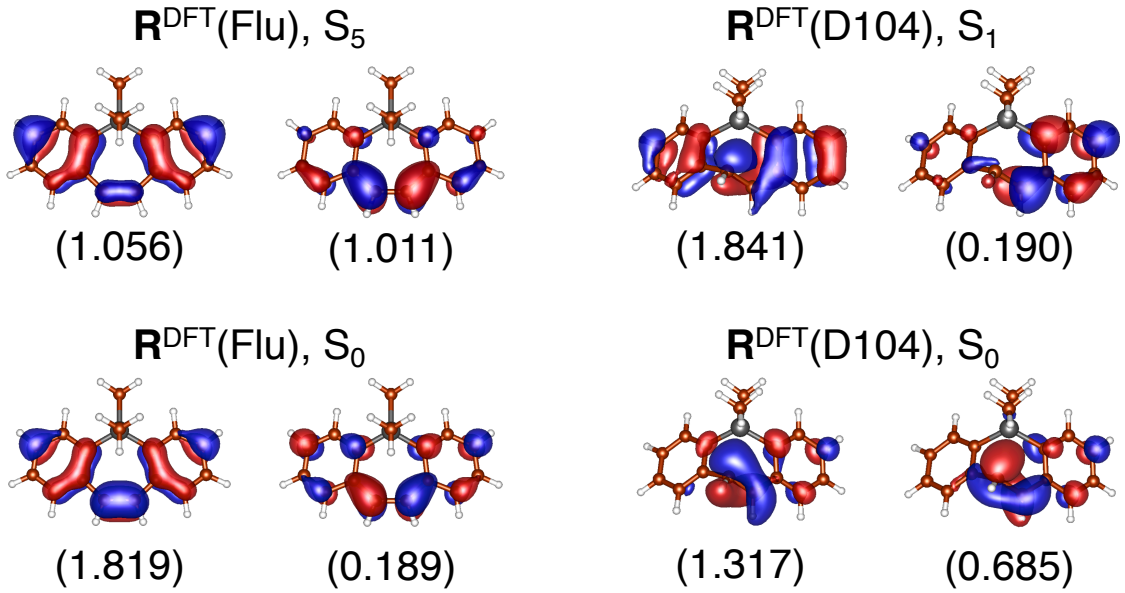

Fig. 3.6: Some of the DMRG-CASSCF natural orbitals of **noPh**. Two orbitals whose occupation numbers are the closest to 1.0 are shown for each electronic state. The orbitals on the left two columns were obtained at $\mathbf{R}^{\mathrm{DFT}}$(Flu), whereas those on the right two columns were at $\mathbf{R}^{\mathrm{DFT}}$(D104). The orbitals on the upper line correspond to the S_1 state at the XMS level, and those on the bottom line correspond to the S_0 state at the XMS level. The occupation number of each natural orbital is given in parentheses. Note that the DMRG-CASSCF S_5 state shows the main contribution to DMRG-XMS-CASPT2 S_1 state at $\mathbf{R}^{\mathrm{DFT}}$(Flu) (see Table Table 3.2).

3.3.4 Comparison of the PECs of noPh, *p*-Ph, and *m*-Ph

Because the XMS level computation can effectively describe all the PECs in this study, the XMS level PECs of **noPh**, ***p*-Ph**, and ***m*-Ph** were compared, as shown in Fig. 3.7. These three PECs had a similar shape with the existence of an activation barrier in the S_1 state. We estimated the $\Delta E^{\ddagger}$ of the three silepins using their PECs to confirm whether there is any relationship with the experimentally-determined Φ_{F}, as shown in Table 3.3. Generally,

larger activation energy results in a smaller nonradiative decay rate constant, which results in a larger fluorescence quantum yield. The trend shown in Table 3.3 implies the possibility that the nonradiative decay treated here is related to the magnitude of Φ_F.

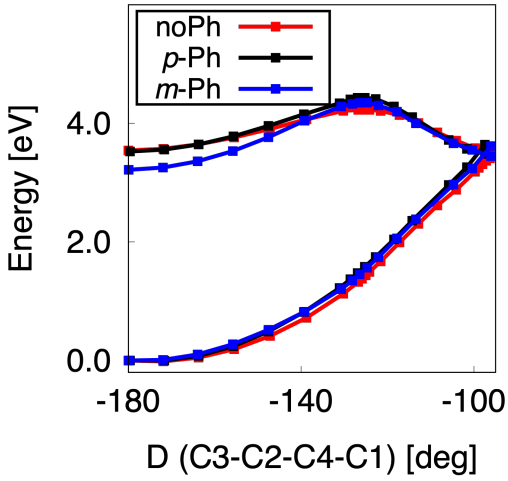

Fig. 3.7: 10SA-DMRG-XMS-CASPT2/ACCD level PECs of the S_0 and S_1 states of **noPh** (red), ***p*-Ph** (black), and ***m*-Ph** (blue). The energy values for plotting are given by the difference from that of the S_0 state at the $\mathbf{R}^{\mathrm{DFT}}$(Flu) for each molecule.

Table 3.3: Computationally estimated activation energies ($\Delta E^{\ddagger}$ [kcal/mol]) and experimentally determined fluorescence quantum yields (Φ_F) of the silepins[59]

	noPh	***p*-Ph**	***m*-Ph**
$\Delta E^{\ddagger}$	15.8	20.9	26.1
Φ_F	0.14	0.38	0.90

In this paragraph, we attempt to clarify the reason for the large $\Delta E^{\ddagger}$ of ***m*-Ph**. In Fig. 3.7, the main difference among silepins is located near $\mathbf{R}^{\mathrm{DFT}}$(Flu). Thus, the reason for the large $\Delta E^{\ddagger}$ of ***m*-Ph** seems to be the stabilization of the fluorescent state. A similar trend was reported for the difference in Φ_F between furan and dibenzofuran[31] and that in k_{nr} of distyrylbenzene derivatives.[33] Because the fluorescent state of silepins is mainly described as HOMO-LUMO excitation, we checked the HOMO-LUMO gap via CAM-B3LYP/ACCD level calculations; the **noPh**, ***p*-Ph**, and ***m*-Ph** gaps were computed to be 5.73, 5.69, and 5.15 eV, respectively. These gaps indicated that, while the name of ***m*-Ph** comes from the position of the phenyl ring from the $SiMe_2$ moiety, introduction of a phenyl ring at the *para*-position from the central C-C bond effectively extended the π conjugation,[59] which resulted in a high fluorescence quantum yield.

3.3.5 Geometries obtained by XMS-CASPT2 level optimization

To confirm the effect of geometry optimization of the TS on the activation energy estimation, we first conducted geometry optimization of the fluorescent state, MECI point, and TS

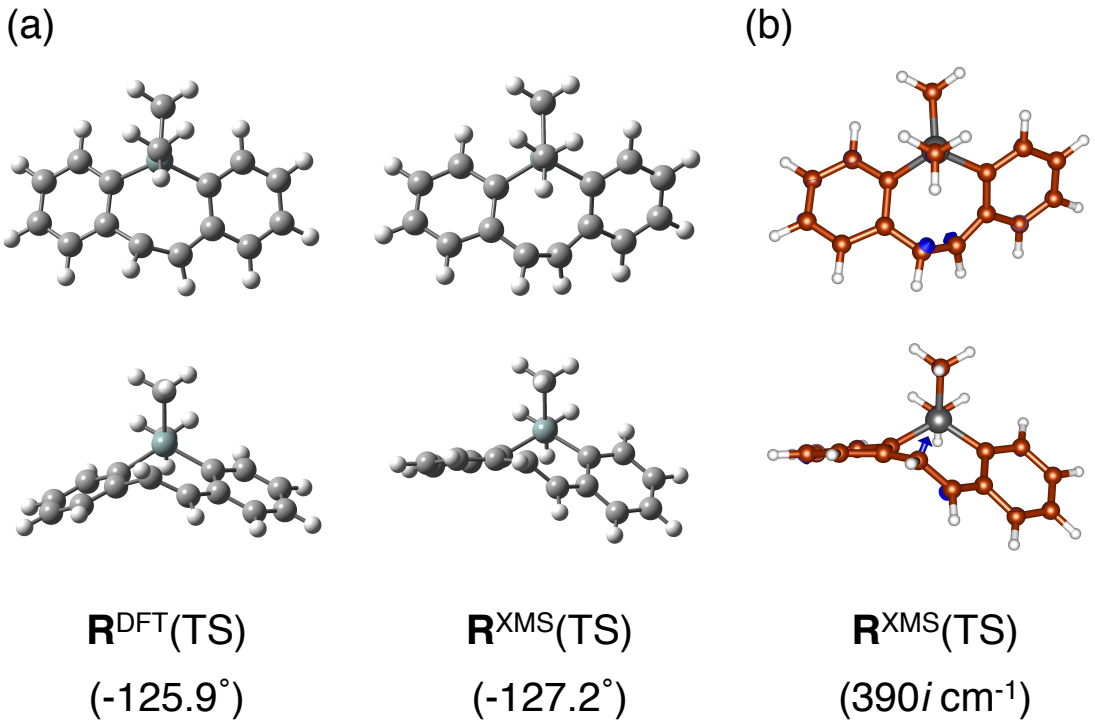

Fig. 3.8: (a) Comparison of $\mathbf{R}^{\mathrm{DFT}}$(TS) and $\mathbf{R}^{\mathrm{XMS}}$(TS) of **noPh** and (b) vibrational mode with the imaginary frequency at $\mathbf{R}^{\mathrm{XMS}}$(TS). The images show the top (first line) and side (second line) views for each geometry. In (a), the dihedral angle of C3-C2-C4-C1 from Fig. 3.3 (b) is shown in parenthesis. In (b), displacements of H atoms are omitted for clarity. The imaginary frequency is shown in parenthesis.

between them at the XMS-CASPT2/def2-SVP level using the BAGEL program; the resultant geometries are denoted as $\mathbf{R}^{\mathrm{XMS}}$(Flu), $\mathbf{R}^{\mathrm{XMS}}$(Con), and $\mathbf{R}^{\mathrm{XMS}}$(TS), respectively. $\mathbf{R}^{\mathrm{DFT}}$(TS) and $\mathbf{R}^{\mathrm{XMS}}$(TS) are shown in Fig. 3.8.$\mathbf{R}^{\mathrm{XMS}}$(TS) had a normal mode with an imaginary frequency of $390i$ cm^{-1}, whose displacement vector except for H atoms is located on the central C-C bond (Fig. 3.8 (b)). $\mathbf{R}^{\mathrm{XMS}}$(TS) has a similar dihedral C3-C2-C4-C1 as that of the geometry obtained from LIIC of the TD-DFT level geometries ($\mathbf{R}^{\mathrm{DFT}}$(TS)); however, the orientation of the left side phenyl ring is obviously different. The effect of this difference on the activation energy estimation will be discussed in the next subsection.

3.3.6 Effect of XMS-CASPT2 level optimization on the activation energy estimation

Next, we built a new reaction coordinate set by connecting LIIC between $\mathbf{R}^{\mathrm{XMS}}$(Flu) and $\mathbf{R}^{\mathrm{XMS}}$(TS) to LIIC between $\mathbf{R}^{\mathrm{XMS}}$(TS) and $\mathbf{R}^{\mathrm{XMS}}$(Con). Then, DMRG-XMS-CASPT2 calculations were conducted to the coordinate set, and the resultant PECs were compared with the PECs along the previous coordinate set as shown in Fig. 3.9. Although the two S_0 state PECs were similar, The S_1 state PECs differed in the heights of their activation barriers. The activation energy in this new PEC was estimated to be 7.9 kcal/mol, which was almost half of that in the PECs along the TD-DFT level LIIC at 15.8 kcal/mol. Additionally, this

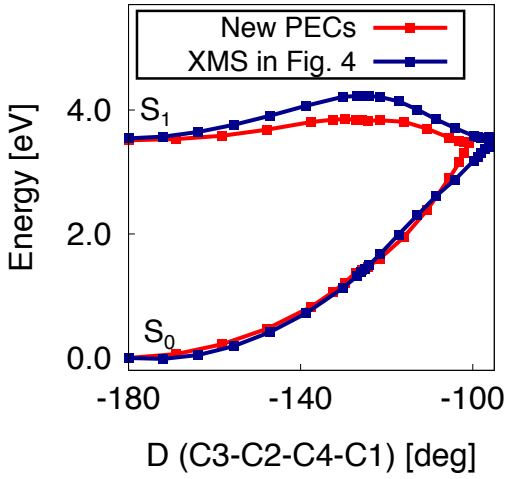

Fig. 3.9: Comparison of PECs of the S_0 and S_1 states of **noPh**. Blue lines were plotted using the same data as those used for XMS in Fig. 3.4. Red lines were computed along the coordinate defined in this subsection. The energies of the blue and red lines are given by the difference from that of the S_0 state at $\mathbf{R}^{\mathrm{DFT}}$(Flu) and at $\mathbf{R}^{\mathrm{XMS}}$(Flu), respectively.

activation energy of 7.9 kcal/mol was comparable to the difference between the energy at $\mathbf{R}^{\mathrm{XMS}}$(TS) and that at $\mathbf{R}^{\mathrm{XMS}}$(Flu) of 7.7 kcal/mol. These results indicated that geometry optimization of the TS using the XMS-CASPT2 calculation is critical to estimating the activation energy and that the approximation of the activation energy as the difference between the energy at $\mathbf{R}^{\mathrm{XMS}}$(TS) and that at $\mathbf{R}^{\mathrm{XMS}}$(Flu) was reasonable.

Finally, the activation energies of **noPh**, ***p*-Ph** and ***m*-Ph** were again compared. Because we could not obtain the fully relaxed geometry of the TS of ***p*-Ph** or ***m*-Ph**, we approximated the activation energy as the difference between the energy at $\mathbf{R}_c^{\mathrm{XMS}}$(Flu) and that at $\mathbf{R}_c^{\mathrm{XMS}}$(TS), which were optimized by fixing the skeleton of **noPh**. For **noPh**, 7.7 kcal/mol, as shown above, was chosen. The activation energies of ***p*-Ph** and ***m*-Ph** were estimated as 8.0 and 12.4 kcal/mol, respectively. These values are obviously smaller than those shown in Table 3.3. By adding the thermal correction using the XMS-CASPT2/def2-SVP level normal mode frequencies, the activation free energy ($\Delta G^{\ddagger}_{\mathrm{cal}}$) of **noPh** was estimated to be 6.9 kcal/mol.

To compare our results with the experimentally determined nonradiative decay rate constant, we estimated the activation free energy ($\Delta G^{\ddagger}_{\mathrm{exp}}$) by employing Eyring's equation[82] (Table 3.4). The computed $\Delta G^{\ddagger}_{\mathrm{cal}}$ of **noPh** of 6.9 kcal/mol was reasonable with the estimated $\Delta G^{\ddagger}_{\mathrm{exp}}$ of 4.1 kcal/mol. Of the silepins in this study, the value of $\Delta E^{\ddagger}$ is qualitatively consistent with $\Delta G^{\ddagger}_{\mathrm{exp}}$. Because $\Delta E^{\ddagger}$ in this study lacks zero-point correction, thermal correction, and a solvation effect, the comparison of $\Delta E^{\ddagger}$ with $\Delta G^{\ddagger}_{\mathrm{exp}}$ may be problematic. However, in the case of **noPh**, the value of $\Delta E^{\ddagger}$ was comparable to that of $\Delta G^{\ddagger}_{\mathrm{cal}}$. Thus, we concluded that the procedure in this section, which included XMS-CASPT2 level geometry optimization, a computation of the potential energy curve, and estimation of the activation energy, may be effective to treat the nonradiative decay of silepins.

Of note, estimation of the rate constant requires a more accurate estimation than that in our results. Our procedure may provide a reasonable estimation of the activation energy; however, the error in estimated Gibbs free energy of 2.8 kcal/mol corresponds to a factor of 8.9×10^{-3} in the estimation of rate constant using Eyring's equation at 298.15 K. This means that our estimation of activation energy cannot provide a quantitative evaluation of the rate constant. The inclusion of a solvation effect or employment of a larger basis set in quantum chemical calculations are some of the possible improvements to achieve higher accuracy.

From our obtained results, we concluded that the main nonradiative decay pathway of **noPh**, ***p*-Ph**, and ***m*-Ph** involves internal conversion via triggered by the twisting of the central C-C bond and that the height of the activation barrier to reach the MECI point is responsible for the differences in their fluorescence quantum yields. However, quantitative estimation of the rate constant is beyond the scope of this procedure.

Table 3.4: Computed activation energies ($\Delta E^{\ddagger}$), computed activation free energy ($\Delta G^{\ddagger}_{\mathrm{cal}}$) of **noPh**, and estimated activation free energies ($\Delta G^{\ddagger}_{\mathrm{exp}}$) in kcal/mol

	noPh	***p*-Ph**	***m*-Ph**
$\Delta E^{\ddagger}$	7.7	8.0	12.4
$\Delta G^{\ddagger}_{\mathrm{cal}}$	6.9	—	—
$\Delta G^{\ddagger}_{\mathrm{exp}}$ [a]	4.1	5.7	6.8

[a] Values were estimated by applying Eyring's equation to the experimentally determined nonradiative decay rate constant of silepins,[59] where a temperature of 298.15 K and a transmission coefficient, κ, of 1.0 were assumed.

3.4 Conclusions

In this chapter, we presented a theoretical analysis of the nonradiative decay process of three kinds of organic dyes, silepin derivatives **noPh**, ***p*-Ph**, and ***m*-Ph**, using recently introduced MR wavefunction approaches, XMS-CASPT2 analytic gradients, and DMRG-XMS-CASPT2 methods. The use of the DMRG method allowed us to handle all valence π orbitals in the active space. Comparisons of the results obtained with different electronic structure methods showed that the choice of method may have an impact on the description of the nonradiative decay triggered by the twisting of the central C-C bond.

With the (TD-)DFT calculations under the Tamm-Dancoff approximation, we found a MECI point, where the central part of the stilbene skeleton lost its planarity. PECs connecting the minimum of fluorescent state and MECI point showed an activation barrier in the S_1 state. Although SR and MR methods gave similar PECs in the region near the fluorescent state minimum, TD-DFT calculations could not reasonably describe the electronic state near the activation barrier geometry in contrast to *bt*-PNO-STEOM-CCSD and DMRG-XMS-CASPT2 calculations. In the region near the MECI point, only the MR method can handle

the complicated electronic state, where S_0 and S_1 states have open-shell and closed-shell characters, respectively. Consequently, we confirmed that geometry optimization of the TS at the TD-DFT level was inadequate for estimation of the activation energy by single-point calculations using higher-level methods and that our DMRG-XMS-CASPT2 calculation could reasonably describe the entire PECs in this study.

We next compared the PECs of three kinds of silepins to confirm whether there was any relationship between the computationally estimated activation energy and the experimentally determined fluorescence quantum yield. We found that the silepin with the larger fluorescence quantum yield gave a larger activation energy. In the case of ***m*-Ph**, whose π conjugation was effectively extended, the stabilization of the fluorescent state resulted in its large activation energy.

We then checked the effect of XMS-CASPT2 level geometry optimization of the TS on the estimation of the activation energy. The TS geometry of **noPh** in the XMS-CASPT2 level calculation showed an obvious difference from the activation barrier in LIIC based on DFT level geometries. The activation energy of **noPh** was estimated to be 7.9 kcal/mol, which was approximately half of the energy obtained with DFT level geometries. With the XMS-CASPT2-based TS geometries of ***p*-Ph** and ***m*-Ph**, their activation energies were predicted to similarly decrease. The activation free energy of **noPh** was computationally estimated to be 6.9 kcal/mol, which was comparable to the activation free energy estimated by applying Eyring's equation to the experimentally determined rate constant of 4.1 kcal/mol. Thus, our final procedure, which was composed of XMS-CASPT2 level geometry optimizations, computation of PECs, and estimation of the activation energy, may be effective to treat the nonradiative decay process of silepins. However, our approach cannot reproduce the experimentally determined nonradiative decay rate constant very accurately in the sense that even a small error in the predicted activation free energy, 2.8 kcal/mol, can affect the rate constant by a factor of 8.9×10^{-3}.

From these results, we concluded that the main nonradiative decay pathway of **noPh**, ***p*-Ph** and ***m*-Ph** is the internal conversion through the conical intersection triggered by the twisting of the central C-C bond and that the height of the activation barrier to reach the conical intersection point is responsible for the differences in their fluorescence quantum yields. To reach this conclusion, energy profiles and geometry optimizations with the proper level of quantum chemical methods played a critical role.

Bibliography

[1] T. Terai and T. Nagano, Pflugers Arch. – Eur. J. Physiol. **465**, 347 (2013).

[2] C. Wang et al., J. Am. Chem. Soc. **139**, 10374 (2017).

[3] G.-Y. Li and K.-L. Han, WIREs Comput. Mol. Sci. **8**, e1351 (2018).

[4] A. Gunia-Krzyżak et al., Int. J. Cosmet. Sci. **40**, 356 (2018).

[5] M. Lorigo, M. Mariana, and E. Cairrao, Steroids **131**, 46 (2018).

[6] A. R. Nunes et al., Adv. Pharmacol. Sci. **2018** (2018).

[7] H. Sadeghifar and A. Ragauskas, Polymers **12**, 1134 (2020).
[8] C. W. Tang and S. A. VanSlyke, Appl. Phys. Lett. **51**, 913 (1987).
[9] M. A. Baldo et al., Nature **395**, 151 (1998).
[10] H. Uoyama, K. Goushi, K. Shizu, H. Nomura, and C. Adachi, Nature **492**, 234 (2012).
[11] M. Godumala, S. Choi, M. J. Cho, and D. H. Choi, J. Mater. Chem. C **4**, 11355 (2016).
[12] Z. Shuai and Q. Peng, Natl. Sci. Rev. **4**, 224 (2017).
[13] X.-K. Chen, D. Kim, and J.-L. Brédas, Acc. Chem. Res. **51**, 2215 (2018).
[14] T. Hatakeyama et al., Adv. Mater. **28**, 2777 (2016).
[15] Y. Kondo et al., Nat. Photonics **13**, 678 (2019).
[16] A. W. Kohn, Z. Lin, and T. Van Voorhis, J. Phys. Chem. C **123**, 15394 (2019).
[17] Z. Lin, A. W. Kohn, and T. Van Voorhis, J. Phys. Chem. C **124**, 3925 (2020).
[18] A. Humeniuk et al., J. Chem. Phys. .
[19] T. Kumpulainen, B. Lang, A. Rosspeintner, and E. Vauthey, Chem. Rev. **117**, 10826 (2017).
[20] A. Datar and A. Hazra, J. Phys. Chem. A **121**, 2790 (2017).
[21] B. O. Roos, P. R. Taylor, and P. E. Si, Chem. Phys. **48**, 157 (1980).
[22] K. Andersson, P.-Å. Malmqvist, and B. O. Roos, J. Chem. Phys. **96**, 1218 (1992).
[23] H. Lischka et al., Chem. Rev. **118**, 7293 (2018).
[24] A. A. Granovsky, J. Chem. Phys. **134**, 214113 (2011).
[25] T. Shiozaki, W. Győrffy, P. Celani, and H.-J. Werner, J. Chem. Phys. **135**, 081106 (2011).
[26] I. N. Ioffe and A. A. Granovsky, J. Chem. Theory Comput. **9**, 4973 (2013).
[27] P. Ghosh and D. Ghosh, J. Phys. Chem. B **121**, 5988 (2017).
[28] C. Xu, F. L. Gu, and C. Zhu, Phys. Chem. Chem. Phys. **20**, 5606 (2018).
[29] I. Polyak, L. Hutton, R. Crespo-Otero, M. Barbatti, and P. J. Knowles, J. Chem. Theory Comput. **15**, 3929 (2019).
[30] Y. Harabuchi, T. Taketsugu, and S. Maeda, Phys. Chem. Chem. Phys. **17**, 22561 (2015).
[31] Y. Harabuchi, T. Taketsugu, and S. Maeda, Chem. Lett. **45**, 940 (2016).
[32] Y.-J. Gao et al., J. Phys. Chem. A **121**, 2572 (2017).
[33] J. Shi et al., Org. Chem. Front. **6**, 1948 (2019).
[34] M. A. Trachsel et al., J. Phys. Chem. Lett. **11**, 3203 (2020).
[35] F. Liu and K. Morokuma, J. Am. Chem. Soc. **134**, 4864 (2012).
[36] F. Liu and K. Morokuma, J. Am. Chem. Soc. **135**, 10693 (2013).
[37] X.-P. Chang, C.-X. Li, B.-B. Xie, and G. Cui, J. Phys. Chem. A **119**, 11488 (2015).
[38] G. Paternò et al., J. Mater. Chem. C **6**, 2778 (2018).
[39] J. W. Park, R. Al-Saadon, M. K. MacLeod, T. Shiozaki, and B. Vlaisavljevich, Chem. Rev. **120**, 5878 (2020).
[40] L. Gagliardi, G. Orlandi, V. Molina, P.-Å. Malmqvist, and B. Roos, J. Phys. Chem. A **106**, 7355 (2002).
[41] A. K. Dutta, F. Neese, and R. Izsák, J. Chem. Phys. **145**, 034102 (2016).
[42] A. K. Dutta, M. Nooijen, F. Neese, and R. Izsák, J. Chem. Theory Comput. **14**, 72

(2017).
[43] R. Izsák, Int. J. Quantum Chem. , e26327 (2020).
[44] R. Berraud-Pache, F. Neese, G. Bistoni, and R. Izsák, J. Chem. Theory Comput. **16**, 564 (2019).
[45] F. Neese, F. Wennmohs, U. Becker, and C. Riplinger, J. Chem. Phys. **152**, 224108 (2020).
[46] S. R. White, Phys. Rev. Lett. **69**, 2863 (1992).
[47] S. R. White, Phys. Rev. B **48**, 10345 (1993).
[48] D. Ghosh, J. Hachmann, T. Yanai, and G. K.-L. Chan, J. Chem. Phys. **128**, 144117 (2008).
[49] S. Sharma and G. K.-L. Chan, J. Chem. Phys. **136**, 124121 (2012).
[50] Y. Kurashige and T. Yanai, J. Chem. Phys. **135**, 094104 (2011).
[51] S. Guo, M. A. Watson, W. Hu, Q. Sun, and G. K.-L. Chan, J. Chem. Theory Comput. **12**, 1583 (2016).
[52] L. Freitag, S. Knecht, C. Angeli, and M. Reiher, J. Chem. Theory Comput. **13**, 451 (2017).
[53] T. Yanai et al., J. Chem. Theory Comput. **13**, 4829 (2017).
[54] M. K. MacLeod and T. Shiozaki, J. Chem. Phys. , 051103 (2015).
[55] B. Vlaisavljevich and T. Shiozaki, J. Chem. Theory Comput. **12**, 3781 (2016).
[56] J. W. Park, J. Chem. Theory Comput. **16**, 326 (2019).
[57] Y. Nishimoto, Chem. Phys. Lett. **744**, 137219 (2020).
[58] T. Shiozaki, WIREs Comput. Mol. Sci. **8**, e1331 (2018).
[59] L. G. Mercier et al., Organometallics **30**, 1719 (2011).
[60] Y. Harabuchi, K. Keipert, F. Zahariev, T. Taketsugu, and M. S. Gordon, J. Phys. Chem. A **118**, 11987 (2014).
[61] T. H. Dunning Jr, J. Chem. Phys. **90**, 1007 (1989).
[62] D. E. Woon and T. H. Dunning Jr, J. Chem. Phys. **98**, 1358 (1993).
[63] T. H. Dunning Jr, K. A. Peterson, and A. K. Wilson, J. Chem. Phys. **114**, 9244 (2001).
[64] R. A. Kendall, T. H. Dunning Jr, and R. J. Harrison, J. Chem. Phys. **96**, 6796 (1992).
[65] A. Schäfer, H. Horn, and R. Ahlrichs, J. Chem. Phys. **97**, 2571 (1992).
[66] K. Eichkorn, F. Weigend, O. Treutler, and R. Ahlrichs, Theor. Chem. Acc. **97**, 119 (1997).
[67] F. Weigend, J. Comput. Chem. **29**, 167 (2008).
[68] F. Weigend, Phys. Chem. Chem. Phys. **4**, 4285 (2002).
[69] F. Weigend, A. Köhn, and C. Hättig, J. Chem. Phys. **116**, 3175 (2002).
[70] C. Hättig, Phys. Chem. Chem. Phys. **7**, 59 (2005).
[71] M. W. Schmidt et al., J. Comput. Chem. **14**, 1347 (1993).
[72] T. Yanai, D. P. Tew, and N. C. Handy, Chem. Phys. Lett. **393**, 51 (2004).
[73] S. Maeda, K. Ohno, and K. Morokuma, J. Chem. Theory Comput. **6**, 1538 (2010).
[74] F. Neese, WIREs Comput. Mol. Sci. **8**, e1327 (2018).
[75] M. J. Frisch et al., Gaussian 16 revision a.03, 2016, Gaussian Inc. Wallingford CT.

[76] *BLOCK verion 1.5: An implementation of the density matrix renormalization group (DMRG) algorithm for quantum chemistry. https://github.com/sanshar/Block.*

[77] J. Finley, P.-Å. Malmqvist, B. O. Roos, and L. Serrano-Andrés, Chem. Phys. Lett. **288**, 299 (1998).

[78] Y. Kurashige, J. Chalupskỳ, T. N. Lan, and T. Yanai, J. Chem. Phys. **141**, 174111 (2014).

[79] J. W. Park and T. Shiozaki, J. Chem. Theory Comput. **13**, 2561 (2017).

[80] N. Minezawa and M. S. Gordon, J. Phys. Chem. A **113**, 12749 (2009).

[81] T. J. Lee and P. R. Taylor, Int. J. Quantum Chem. **36**, 199 (1989).

[82] H. Eyring, J. Chem. Phys. **3**, 107 (1935).

Chapter 4

Theoretical insight into the Effect of Phosphorus Oxygenation on the Nonradiative Decays: A Comparative Study on P-Bridged Stilbene Analogues

4.1 Introduction

Phosphorus is one of the atoms introduced into the organic π-skeleton to develop functionalized organic dye molecules. Yamaguchi et al. have synthesized phosphole-containing π-conjugated molecules and use them for various applications.[1–8] The molecules developed include the super-photostable dye molecules,[3,6,7] and the molecules with fluorescence at a near-infrared (NIR) region.[4,5,8] Yasuda et al. systematically symthesized a series of dye molecules with the thermally activated delayed fluorescence (TADF) containing a six-membered phosphacycle.[9] Because of these characteristic properties, phosphorus-containing organic dye molecules have attracted growing attentions.

One of the characteristic properties of the phosphorus atom is the functionalization arising at the phosphorus atom upon changing its oxidation state.[2,10] Phosphole has a lone pair on each phosphorus atom, which can play a role in coordination to Lewis acids or metallic atoms. The phosphorus atom of phosphole can be oxidized, such as oxygenation to phosphole-oxide. The previous studies showed that such coordination or oxygenation lowers the LUMO level.[10] Actually, oxygenation of bis-phosphanyl-bridged stilbene (**P-Ben** in Fig. 4.1) to bis-phosphoryl-bridged stilbene (**PO-Ben** in Fig. 4.1) caused a red-shift in absorption and fluorescence by lowering the LUMO level.[1] At the same time, it turned out to be that this oxygenation drastically increased the fluorescence quantum yield (Φ_F) from 0.07 to 0.98.

Later, Yamaguchi et al. synthesized the thiophene-fused analogues of the P-bridged stilbenes.[2] There, it turned out to be that the substitution of the stilbene skeleton in **P-Ben** into the thiophene-fuzed skeleton to produce **P-Thio′** in Fig. 4.1 also drastically increased

its Φ_F to 0.95. On the contrary, the oxigenation of **P-Thio′** to produce **PO-Thio′** turned out to drastically decrease the Φ_F from 0.95 to 0.04. Understanding the mechanism of the changes in Φ_F might give an insight into the fine-tuning of the phosphorus-containing π-conjugated molecules; however, it remained unclear to my best knowledge. To make it clear, understanding the excited-state dynamics should be essential.

Recently, various perturbative methods to predict the rate constants of electronic transitions have been proposed and developed. Barone and Santoro et al. simulated the absorption and radiative spectra including the vibronic effect, using time-independent and time-dependent formalisms.[11–17] Shuai et al. developed a time-dependent approach, which is called the thermal vibration correlation function (TVCF) formalism, to predict the rate constants of the radiative decay, internal conversion, and intersystem crossings.[18–21] To properly handle intersystem crossings in molecules mediated by small spin-orbit coupling matrix elements (SOCMEs), Shuai et al. employed a formalism based on 2nd-order perturbation theory,[21] which was employed in a recent study by Kim et al.[22,23] As another route, Marian et al. developed a method to use the 1st-order derivatives of SOCMEs in the framework based on the Herzberg–Teller expansion.[24–26] Recently, Neese et al. implemented some of the methods as mentioned above in their ORCA program.[27] These methods allow us to predict the rate constants of the electronic transitions in an effective but black-box manner. Nonetheless, there is a technological issue associated with the fact that, except FCClasses by Santoro, the accessibility to the source codes of the programs is limited.

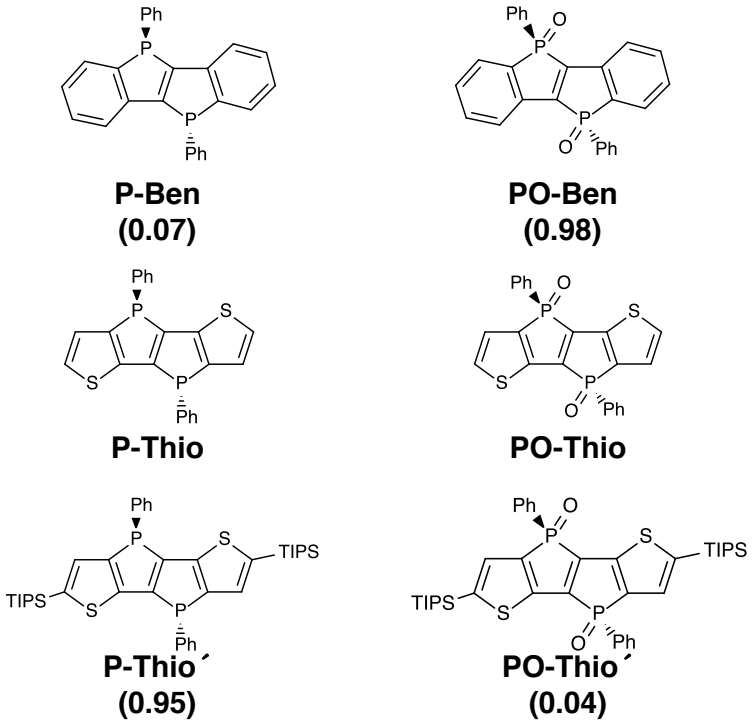

Fig. 4.1: Chemical structures of the molecules in this study. For experimentally obtained molecules, their fluorescence quantum yields[1,2] are shown in the parentheses. **P-Thio** and **PO-Thio** are the model structures employed in this study.

In this study, I exploit the rate constant calculations to gain some insight into the effect of oxygenation of the phosphorus atom in the P-bridged stilbene analogues on their nonradiative decay. The molecules to be studied can be consulted in Fig. 4.1. To mitigate the computational cost, we computed the model molecules **P-Thio** and **PO-Thio**, which are derived on the assumption that the TIPS moiety in the original molecules **P-Thio′** and **PO-Thio′** do not affect the decay processes. For enabling the rate constant calculations, I wrote a Python code based on the β version of FCClasses 3.0,[28] which was kindly provided by Prof. Santoro. After optimizing geometries of the S_1 and several triplet states for the molecules of interest, the rate constants for transitions from the S_1 state were computed to explain the effect on the nonradiative decays. The rate constants thus obtained turned out to be reasonable to explain the increase in Φ_F from **P-Ben** to **PO-Ben** and **P-Thio**; however, small Φ_F of **PO-Thio** cannot be explained reasonably. Then, by assuming energetic accessibility of **PO-Thio** to a conical intersection (CI), the minimal energy CI (MECI) geometry was optimized using the extended multireference quasi-degenerate perturbation theory (MR-QDPT). The computed MECI geometry seemed to be stable enough to explain a high nonradiative decay rate constant of **PO-Thio**. By employing both the perturbative method and MECI optimization, I achieved a comparative study among the P-bridged stilbene analogues.

4.2 Computational details

All calculations were conducted treating each molecule as a single isolated system in the gas phase. Geometry optimizations and Hessian calculations were performed at the standard TD-PBE0/cc-pVDZ level of theory[29–31] on the S_0, S_1 and several lowest-lying triplet states, where T_1 state was not computed due to the large energy gap relative to the S_1 state. The transition dipole moments, analytical derivatives of them, and nonadiabatic coupling elements were computed at the minimum of the S_1 state at the same computational level. The spin-orbit coupling matrix elements (SOCMEs) were computed at the ZORA-TD-PBE0/ZORA-def2-TZVP level of theory[32–34] using the Breit-Pauli type Hamiltonian with the mean-field approximation to the 2-electron term.[35] For this SOC calculations, the SARC/J basis[36] was employed for the density fitting to the Coulomb term, and the chain-of-sphere exchange was employed for the exchange term to accelerate the calculation (RIJCOSX).[37] The derivatives of the SOCMEs were estimated using the numerical differentiation method at the minimum of the S_1 state under the same computational condition. At the optimized geometries, the similarity transformed equation-of-motion coupled-cluster model at the singles and doubles with the approximation with the domain-based local pair natural orbital (DLPNO-STEOM-CCSD)[38–40] calculations were conducted with the cc-pVTZ basis set, where the density fitting approximation to the RHF calculation at the RIJCOSX level with the universal def2/J basis sets and that to the DLPNO-STEOM-CCSD calculation with the cc-pVTZ/C basis sets were applied, to validate the estimations of the relative energies at the TD-PBE0 level. DLPNO-STEOM-CCSD calculations were conducted using ORCA 5.0.1 program,[27] while SOCMEs were re-computed using ORCA 5.0.2 program to avoid a technical issue in version 5.0.1.

Other TD-DFT calculations were conducted using Gaussian 16 Rev. B01 program.[41]

The rate constants of electronic transitions were estimated using a perturbative method like Fermi's golden rule, where the time-dependent formalism was applied for numerical calculation, i.e. the correlation function formalism.[15,20,21,24–26] Transition dipole moment for fluorescence calculations and SOCMEs for intersystem crossing rate constant calculations were treated under the Franck–Condon (FC) and Herzberg–Teller (HT) approximation; whereas the method including intermediate states for intersystem crossing[21–23,26] was unused. The total rate constant of the intersystem crossing from S_1 to a triplet state was computed as a sum of those to each spin-sublevel of the triplet states.[26] The vibrational modes at the initial and final states were employed under the relation of the Duschinsky rotation,[42] where the shift vector and Duschinsky matrix were computed in the redundant internal coordinate space.[13,16,43] The scaling factor to the vibrational frequencies was unused. The vibrational state at the initial state was given by the Boltzmann distribution, where a temperature of 300 K was employed. The dephasing of the delta function in the Fermi's golden rule was expressed by a Gaussian function with its half-with-half-maximum (HWHM) of 50 cm^{-1}. The time range to compute the correlation function was set to be [0.05 fs, 10000.05 fs] with a time step of 0.1 fs. The correlation function at the negative time was inserted by the complex conjugate of the positive time region.

The rate constants of the fluorescent decay (k_r), $S_1 \rightarrow S_0$ internal conversion (k_{ic}) and intersystem crossing to each triplet state ($k_{isc}(T)$) were computed for the four molecules, **P-Ben**, **PO-Ben**, **P-Thio**, and **PO-Thio**. When the triplet state obtained is more unstable than the S_1 state by over 10.0 kcal/mol, it was not considered as the final state in the intersystem crossing. The adiabatic energy was first estimated at the TD-PBE0 level; then, a correction to it using the DLPNO-STEOM-CCSD theory was also considered when the predicted % active character resulted in an acceptable ratio.

The rate constants were computed using my Python code, where the module for building internal coordinates was imported from Psi4,[44] and the matrix operations related to internal coordinate space were coded in accordance with the code of FCClasses, which was kindly provided by Prof. Santoro.[28] The details of the methods to compute rate constants and their implementations are presented in Chapter 2.

The geometries of the minimum of the S_1 state and the minimal energy conical intersection (MECI) of **PO-Thio** were determined by the optimization procedure. To handle complicated electronic structures in the vicinity of the MECI geometry, we used the extended multistate complete-active-space second-order perturbation theory (XMS-CASPT2),[45] where all of the valence π-orbitals in the thiophene-fused skeleton were included in the active space, corresponding to the 14 electrons in the 12 orbitals, i.e. (14e,12o). The active space of **PO-Thio** was depicted in Fig. 4.2. In the geometry optimizations, three electronic states were computed by the state-averaged (SA-) CASSCF scheme in these active spaces. For these electronic states, the perturbative correction was considered in the so-called SS-SR contraction scheme, where an imaginary level-shift[46,47] at 0.3 Eh was employed whereas the IPEA shift[48] was unused. According to the original method,[45] the zeroth-order Hamiltonian for the pertur-

bative correction was constructed using the state-averaged density. In the MECI geometry optimization, the analytical interstate coupling[47,49] was employed. To avoid numerical instability in geometry optimization, the threshold for the overlap of the internally contracted basis was set to be 1.0×10^{-7}.[50] These geometry optimizations at the XMS-CASPT2 level were conducted using the QSimulate-QM program.[51]

After obtaining the minimum of the S_1 state and MECI geometries, a set of the linearly interpolated internal coordinates (LIIC) between them was prepared to compute the potential energy curves (PECs) from single-point calculations on them. For the LIIC geometries, the XMS-CASPT2/cc-pVDZ level calculations were conducted using ORZ program. The active space employed was the same as the geometry optimization using QSimulate-QM. I conducted 3SA- and 5SA-XMS-CASPT2 calculations at each geometry, where the 1st-order wavefunctions were expanded in the MS-MR contraction scheme. The activation energy to reach the MECI geometry was estimated using the computed PECs. The geometry optimization of the transition state was not conducted because the highest energy at the S_1 state was obtained at the MECI geometry.

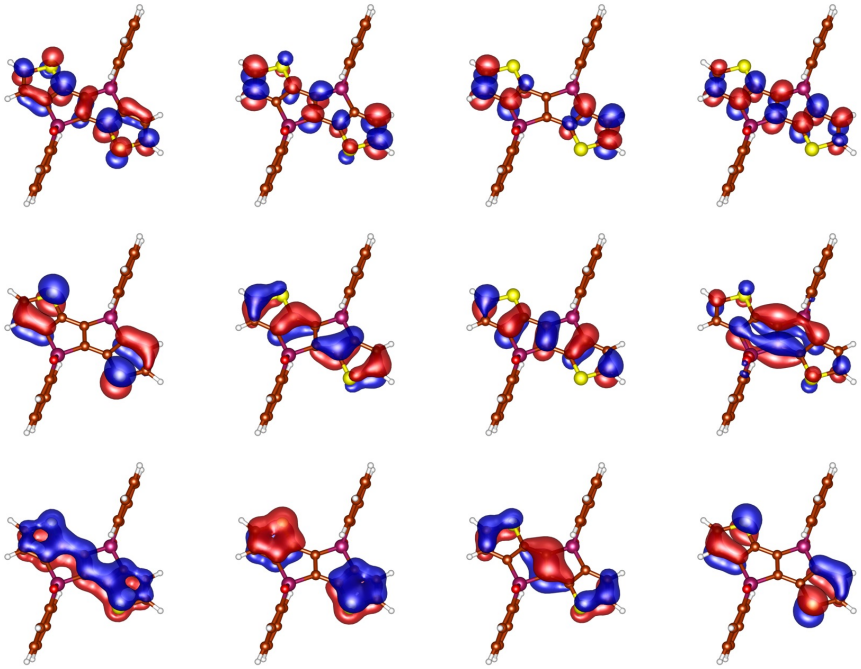

Fig. 4.2: The active orbitals in the XMS-CASPT2 calculations for **PO-Thio** at the optimized S_1 state geometry at the XMS-CASPT2 level. 14 electrons occupy these 12 orbitals (14e,12o).

4.3 Results and discussion

To discuss the effect of oxygenation of the phosphorus atom in the P-bridged stilbene analogues on their nonradiative decay, first, the absorption and fluorescence energies were compared with the experimental data to validate the level of the TD-DFT calculations in this study. Then, my prediction of the rate constants of the transition in **P-Ben**, **PO-Ben**, **P-**

Thio, and **PO-Thio** were presented to check whether or not it reproduced the experimental observation related to Φ_F in them. Using these computational results, the effect of the oxygenation of the phosphorus atom was analyzed using the energy levels of the Kohn-Sham orbitals. Finally, a discussion about the decay via CI in **PO-Thio** was presented.

4.3.1 Absorption and Fluorescence Energies

To check the validity of the computational methods employed, I compared the computed vertical absorption and fluorescence energies and resulting Stokes-shifts with experimentally obtained ones in Table 4.1. I estimated the energies at the TD-PBE0 and DLPNO-STEOM-CCSD level using the geometries optimized at the TD-PBE0 level. The TD-PBE0 calculations well reproduced both the absorption and fluorescence energies with a maximum absolute error of 0.16 eV. The single-point calculations at the DLPNO-STEOM-CCSD levels slightly overestimated the energies compared to the TD-PBE0 level predictions. Although both of the two computed results overestimated the Stokes-shift, it seems that the predicted PES at the S_1 state around the minimum was well described at these computational levels.

Table 4.1: Comparison of the computationally estimated energies of absorption, fluorescence and Stokes-shift with experimentally obtained ones in eV unit

Dye	PBE0[a]			STEOM[b]			Exp.[c]		
	Abs.	Ems.	Shift	Abs.	Ems.	Shift	Abs.	Ems.	Shift
P-Ben	3.59	2.92	-0.67	3.76	3.07	-0.70	3.53	2.99	-0.54
PO-Ben	3.20	2.42	-0.78	3.39	2.58	-0.80	3.14	2.58	-0.56
P-Thio	3.12	2.45	-0.66	3.27	2.57	-0.70	2.95	2.40	-0.55
PO-Thio	2.66	1.89	-0.77	2.85	2.03	-0.82	2.52	2.03	-0.49

[a] Energies and geometries at the TD-PBE0/cc-pVDZ level

[b] Geometries at the TD-PBE0/cc-pVDZ level and energies at the DLPNO-STEOM-CCSD/cc-pVTZ level

[c] Taken from Ref. 1 and 2

4.3.2 P-Ben

The optimized geometries were obtained at the S_1 state and two triplet states. The natural transition orbitals (NTOs)[52] mainly contributing to the states of interest for the optimized geometries were depicted in Fig. 4.3. The S_1 state was well characterized as the π-π^* transition in the stilbene skeleton, which was assigned to be the HOMO-LUMO transition relative to the S_0 state. I obtained two triplet state geometries close in energy to the S_1 state; the one is expressed by the n(P)-π^* transition, denoted as T(n-π^*), and the other is expressed by the π-π^* transition in the side phenyl ring, denoted as T(Ph-Ph). The relative energies of the T(n-π^*) and T(Ph-Ph) states against the S_1 state were estimated to be -7.1 and -2.1

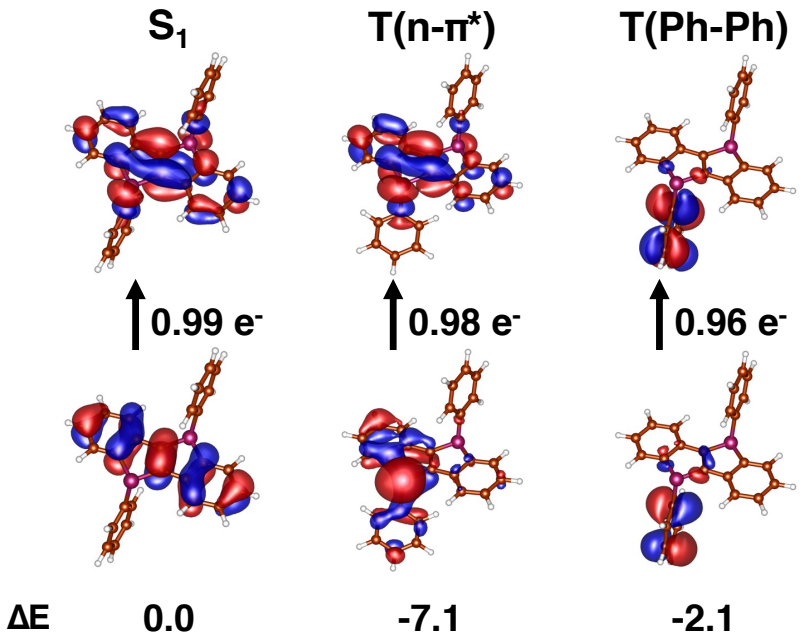

Fig. 4.3: The natural transition orbitals (NTOs) of **P-Ben** at each optimized geometry. The pictures in the higher line are the lowest unoccupied ones (LUNTO), while those in the lower line are the highest occupied ones (HONTO). The numbers between each HONTO and LUNTO represent their eigenvalues. The relative energies against the minimum of the S_1 state at the TD-PBE0 level are given below each HONTO.

kcal/mol, respectively at the TD-PBE0 level, while they were estimated to be -7.0 and -5.3 kcal/mol, respectively, at the STEOM level. Because the rate constant of the nonradiative transition tends to be large when the energy gap is small, I found it necessary to compute the rate constant of the intersystem crossing to these triplet states.

I computed the rate constants of the fluorescent decay (k_r), $S_1 \rightarrow S_0$ internal conversion (k_ic) and intersystem crossing to the T(n-π^*) state ($k_\mathrm{isc}(\mathrm{n}\pi)$) and to the T(Ph-Ph) state ($k_\mathrm{isc}(\mathrm{PP})$). Then, the nonradiative decay rate constant was estimated by $k_\mathrm{nr} = k_\mathrm{ic} + k_\mathrm{isc}(\mathrm{n}\pi) + k_\mathrm{isc}(\mathrm{PP})$. The estimated rate constants were compared with the experimentally estimated values[1] in Table 4.2. By assuming the lifetime of the S_1 state is 1.4 ns and the fluorescence quantum yield is 0.07, respectively, k_r and k_nr were estimated to be 5.0×10^7 and 6.6×10^8 s^{-1}, respectively. Note that this estimation was not given in Ref. 1, probably to avoid the treatment of the additional lifetime of 9.8 ns given there.

The computed rate constants and resulting fluorescence quantum yields were collected in Table 4.2. With the TD-PBE0 level calculations, the radiative decay rate was estimated to be 7.4×10^7 s^{-1}, which is in good agreement with that assumed using experimental data. Here, the major component is attributed to the FC term; the radiative decay rate constant at the FC level was estimated to be 6.7×10^7 s^{-1} according to the fact that this transition is dipole-allowed. The internal conversion rate constant was estimated to be 6.1×10^3 s^{-1}; it is much lower than the radiative one due to the large adiabatic energy, 3.26 eV.

The intersestem crossing rate constants $k_\mathrm{isc}(\mathrm{n}\pi)$ and $k_\mathrm{isc}(\mathrm{PP})$ were predicted to be 8.9×10^7

Table 4.2: Comparison of the computationally estimated rate constants and fluorescence quantum yield with experimentally estimated ones of **P-Ben** in s^{-1} unit.

	Cal.(PBE0)[a]	Cal.(STEOM)[b]	Exp.[c]
k_r	7.4×10^7	9.3×10^7	5.0×10^7
k_{ic}	6.1×10^3	9.0×10^2	—
$k_{isc}(n\pi)$	8.9×10^7	8.7×10^7	—
$k_{isc}(PP)$	1.6×10^8	4.8×10^8	—
k_{nr}	2.5×10^8	5.6×10^8	6.6×10^8
Φ_F	0.23	0.14	0.07

[a] Energies, geometries and Hessians at the TD-PBE0/cc-pVDZ level were employed.
[b] Geometries and Hessians at the TD-PBE0/cc-pVDZ level and energies at the DLPNO-STEOM-CCSD/cc-pVTZ level were employed.
[c] Estimated by assuming the lifetime of the S_1 state is 1.4 ns and the fluorescence quantum yield is 0.07, which were taken from Ref. 1. The additional lifetime of 9.8 ns given there was neglected.

and 1.6×10^8 s^{-1}, respectively. The major components of these intersystem crossing rate constants both arise from the FC term, in which their FC contributions were estimated to be 8.2×10^7 and 8.6×10^7 s^{-1}, respectively. The averaged SOC, which was computed by $||\text{SOCMEs}||/\sqrt{3}$, between the T(n-$\pi^*$) and S_1 states and between the T(Ph-Ph) and S_1 states were computed to be 1.77 and 1.11 cm^{-1}, respectively, at the minimum of the S_1 state. These large SOCs indicate that these intersystem crossings are dominantly driven by the FC term.

Based on these rate constants, the fluorescence quantum yield was estimated to be 0.23. Although the estimated value was larger than the experimentally obtained one, the present computations qualitatively reproduced the low Φ_F of **P-Ben**.

The correction of the relative energies at the DLPNO-STEOM-CCSD level slightly changed the rate constants. The S_1-S_0 adiabatic energy was estimated to be 3.48 eV, which was slightly larger than 3.26 eV at the TD-PBE0 level. Because the prefactor of the fluorescence spectrum contains ω^3 in its numerator, the integration of the enhanced fluorescence spectrum resulted in the slightly larger radiative decay rate constant. On the contrary, this increase of the adiabatic energy decreased the internal conversion rate constant. Because the S_1-T(n-π^*) adiabatic energy at the STEOM level was comparable to that at the TD-PBE0 level, the intersystem crossing rate constant was also comparable. The S_1-T(Ph-Ph) adiabatic energy at the STEOM was larger than that at the TD-PBE0 level, resulting in the larger rate constant. It is because the reorganization energy was large with its value at 0.67 eV; note that the energy gap low is true for the transitions with small displacement. Based on these rate constants, the fluorescence quantum yield was estimated to be 0.14. These results reflect that the rate constants are sensitive to the estimation of the adiabatic energies.

To sum up, my computations qualitatively reproduced the experimental observation that

the fluorescence quantum yield is much lower than unity. That should result from the efficient intersystem crossings from the S_1 state because the two triplet states are energetically close to the S_1 state and the SOCMEs between the triplet and S_1 states are large enough.

4.3.3 PO-Ben

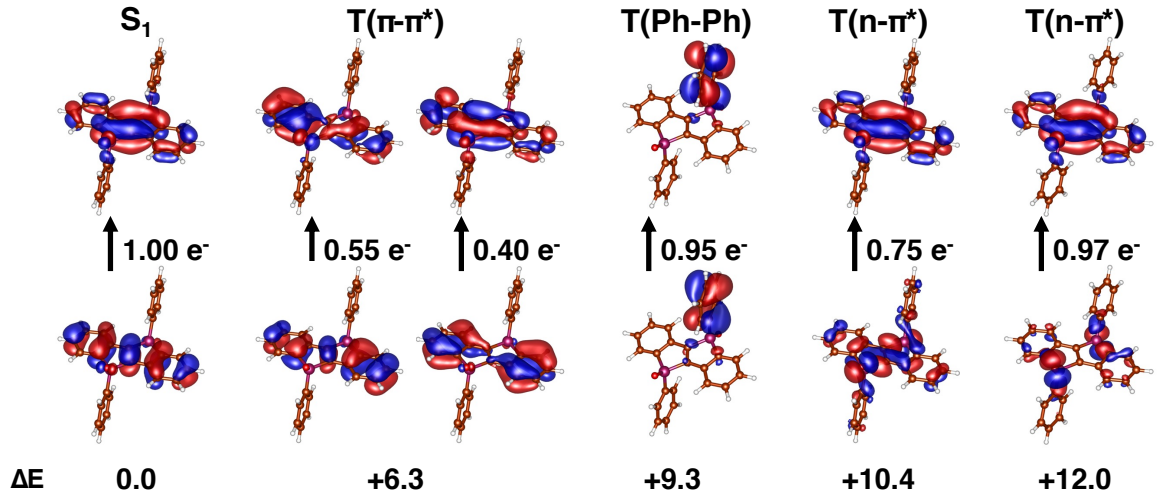

Fig. 4.4: The natural transition orbitals (NTOs) at each optimized geometry. The pictures in the higher line are the unoccupied ones while those in the lower line are the occupied ones. The numbers between each occupied and unoccupied NTOs represent their eigenvalues. The relative energies against the minimum of the S_1 state are given below occupied NTOs.

The geometries at the S_1 state and four triplet states were optimized. The NTOs which mainly contribute to the states of interest at each geometry were depicted in Fig. 4.4. The S_1 state was well characterized as the π-π^* transition in the stilbene skeleton, which was assigned to be the HOMO-LUMO transition from the S_0 state. On the contrary to the **P-Ben**, all of the triplet states obtained were more unstable than the S_1 state. A triplet state was 6.3 kcal/mol more unstable than the S_1 state. Because this triplet state was expressed by two π-π^* transitions, this state was denoted as T(π-π^*). As is found in **P-Ben**, a triplet state with the excitation in the phenyl ring was obtained, which was denoted as T(Ph-Ph). However, this state was turned out to be 9.3 kcal/mol more unstable than the S_1 state. The other triplet states were expressed by the n(O)-π^* transitions. Because these n-π^* type triplet states were more unstable than the S_1 state by over 10.0 kcal/mol, only the T(π-π^*) and T(Ph-Ph) states were included for intersystem crossing rate constant calculation; the resulting rate constant were denoted as $k_{\mathrm{isc}}(\pi\pi)$ and k_{isc}(PP), respectively.

I computed the rate constants of the fluorescent decay (k_{r}), $S_1 \rightarrow S_0$ internal conversion (k_{ic}) and intersystem crossings ($k_{\mathrm{isc}}(\pi\pi)$ and k_{isc}(PP)). Then, the nonradiative decay rate constant was estimated by $k_{\mathrm{nr}} = k_{\mathrm{ic}} + k_{\mathrm{isc}}(\pi\pi) + k_{\mathrm{isc}}(\mathrm{PP})$. The estimated rate constants were compared with the experimentally estimated values[1] in Table 4.3.

The radiative decay rate constant was estimated to be 3.9×10^7 s^{-1}, which was in good

Table 4.3: Comparison of the computationally estimated rate constants with experimentally estimated ones of **PO-Ben** in s^{-1} unit.

	Cal.(PBE0)[a]	Cal.(STEOM)[b]	Exp.[c]
k_r	3.9×10^7	5.2×10^7	6.2×10^7
k_{ic}	1.5×10^6	2.3×10^5	—
$k_{isc}(\pi\pi)$	1.4×10^5	3.7×10^6	—
k_{isc}(PP)	1.0×10^6	—[d]	—
k_{nr}	2.7×10^6	—	1.3×10^6
Φ_F	0.94	—	0.98

[a] Energies, geometries and Hessians at the TD-PBE0/cc-pVDZ level were employed.
[b] Geometries and Hessians at the TD-PBE0/cc-pVDZ level and energies at the DLPNO-STEOM-CCSD/cc-pVTZ level were employed.
[c] Taken from Ref. 1 [d] Failed to compute DLPNO-STEOM-CCSD result with reasonable % active character

agreement with the experimentally obtained value at 6.2×10^7 s^{-1}. Again, the major component was the FC term; radiative decay rate constant at the FC level was estimated to be 3.4×10^7 s^{-1} because this transition is dipole-allowed. The internal conversion rate constant was estimated to be 1.5×10^6 s^{-1}; this value was sensitive to the Duschinsky rotation because it was estimated to be 2.4×10^4 s^{-1} without including the Duschinsky rotation. Anyway, the large S_1-S_0 adiabatic energy at 2.81 eV partially made this decay slow.

The intersystem crossing rate constants $k_{isc}(\pi\pi)$ and k_{isc}(PP) were estimated to be 1.4×10^5 s^{-1} and 1.0×10^6 s^{-1}, respectively. The major component of the predicted $k_{isc}(\pi\pi)$ was the HT and FC/HT terms, where the FC term was estimated to be 4.9×10^{-3} s^{-1}. This was due to the negligible SOC values; the averaged SOC was estimated to be 2.46×10^{-5} cm^{-1} at the minimum of the S_1 state. The major component of the predicted k_{isc}(PP) was also the HT and FC/HT terms, where the FC term was estimated to be 6.7×10^4 s^{-1} despite the large SOCMEs; the averaged SOC between the T(Ph-Ph) and S_1 states was estimated to be 2.76 cm^{-1}. These results indicated that expansion of SOCMEs at the FCHT level was required to predict the intersystem crossing rate constants in **PO-Ben**.

Based on these rate constants, the Φ_F of **PO-Ben** was predicted to be 0.94, which was in good agreement with the experimentally obtained value at 0.98. This high value comes from small nonradiative decay rate constants, which is partially from the suppressed intersystem crossing due to the higher energy level of the triplet states than the S_1 state and lack of the lone pair of phosphorus atoms to produce the n-π^* type triplet states.

The correction to the adiabatic energy at the STEOM-DLPNO-CCSD level was conducted; however, I could not obtain the computational results with a reasonable % active character at the T(Ph-Ph) geometry. For the other rate states, the energy corrections slightly affected the rate constants.

4.3.4 P-Thio

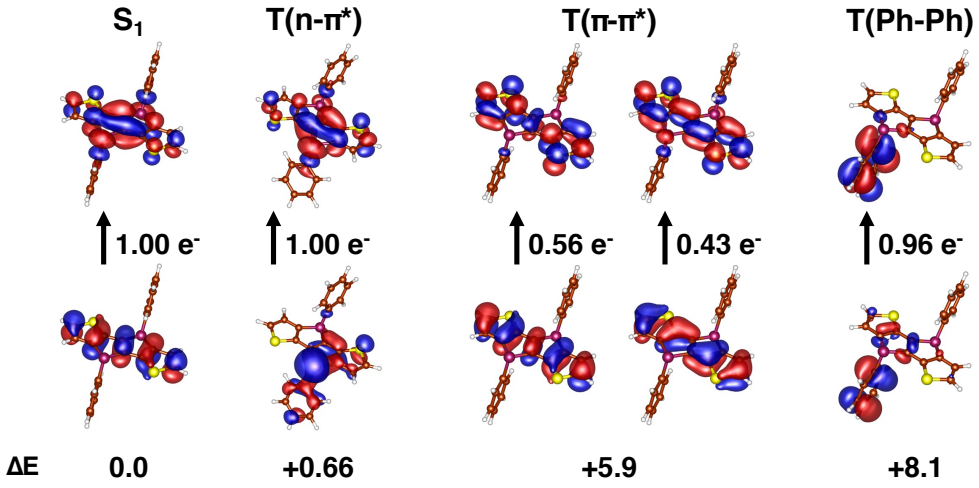

Fig. 4.5: The natural transition orbitals (NTOs) of **P-Thio** at the optimized geometries. The pictures in the higher line are the unoccupied ones while those in the lower line are the occupied ones. The numbers between each occupied and unoccupied NTOs represent their eigenvalues. The relative energies against the minimum of the S_1 state are given below occupied NTOs.

The geometries at the S_1 state and three triplet states were optimized. The NTOs which mainly contribute to the states of interest at each geometry were depicted in Fig. 4.5. Again, the S_1 state was well characterized as the π-π^* transition, which was assigned to be the HOMO-LUMO transition from the S_0 state. The triplet states obtained were characterized by the n-π^* transition, π-π^* transitions at the main skeleton, and π-π^* transitions at the phenyl ring, respectively; hence, they were denoted as T(n-π^*), T(π-π^*), and T(Ph-Ph), respectively. On the contrary to **P-Ben**, all of the triplet states optimized were more unstable than the S_1 state. Because the destabilization energy against the S_1 state was less than 10 kcal/mol, all of the three triplet states were included in the intersystem crossing rate constant calculations.

I computed the rate constants of the fluorescent decay (k_r), $S_1 \rightarrow S_0$ internal conversion (k_{ic}) and intersystem crossing to the T(n-π^*) state ($k_{isc}(n\pi)$), that to the T(π-π^*) state ($k_{isc}(\pi\pi)$), and that to the T(Ph-Ph) state ($k_{isc}(PP)$). Then, the nonradiative decay rate constant was estimated by $k_{nr} = k_{ic} + k_{isc}(n\pi) + k_{isc}(\pi\pi) + k_{isc}(PP)$. The estimated rate constants were compared with the experimentally estimated values of the original molecule[2] in Table 4.4.

The radiative decay rate constant was estimated to be 5.3×10^7 s^{-1}, which was in good agreement with the experimentally obtained value at 1.3×10^8 s^{-1}. Again, the major component was the FC term; radiative decay rate constant at the FC level was estimated to be 4.3×10^7 s^{-1} because this transition is dipole-allowed. The internal conversion rate constant was estimated to be 1.4×10^5 s^{-1}, which was much lower than that of the radiative decay.

The intersestem crossing rate constants $k_{isc}(n\pi)$, $k_{isc}(\pi\pi)$, and $k_{isc}(PP)$ were predicted to be 2.8×10^5, 1.1×10^6, and 7.2×10^5 s^{-1}, respectively. The major component of $k_{isc}(n\pi)$

Table 4.4: Comparison of the computationally estimated rate constants with experimentally estimated ones of **P-Thio** in s^{-1} unit.

	Cal.(PBE0)[a]	Cal.(STEOM)[b]	Exp.[c]
k_r	5.3×10^7	6.9×10^7	1.3×10^8
k_{ic}	1.4×10^5	2.1×10^5	—
$k_{isc}(n\pi)$	2.8×10^5	4.3×10^6	—
$k_{isc}(\pi\pi)$	1.1×10^6	—[d]	—
$k_{isc}(PP)$	7.2×10^5	1.9×10^7	—
k_{nr}	2.2×10^6	—	6.7×10^6
Φ_F	0.96	—	0.95

[a] Energies, geometries and Hessians at the TD-PBE0/cc-pVDZ level were employed.

[b] Geometries and Hessians at the TD-PBE0/cc-pVDZ level and energies at the DLPNO-STEOM-CCSD/cc-pVTZ level were employed.

[c] Taken from Ref. 2

[d] Failed to compute DLPNO-STEOM-CCSD result with reasonable % active character

and $k_{isc}(PP)$ were the FC term, whereas FC contribution of $k_{isc}(\pi\pi)$ was negligible; FC contributions of $k_{isc}(n\pi)$, $k_{isc}(\pi\pi)$, and $k_{isc}(PP)$ were predicted to be 2.0×10^5, 1.9×10^{-3} and 4.8×10^5 s^{-1}, respectively. The averaged SOC between the T(n-π^*) and S_1 states and that between the T(Ph-Ph) and S_1 states were estimated to be 3.57 and 5.54 cm^{-1} respectively, at the minimum of the S_1 state. Because of the large SOCMEs, the FC term became dominant in these intersystem crossings. Although the norm of these SOCMEs was larger than those of **P-Ben**, the intersystem crossing rate constants were smaller than those of **P-Ben**. This may come from the fact that the triplet states were more unstable than the S_1 state in the case of **P-Thio**. On the other hand, the averaged SOC between the T($\pi\pi^*$) and S_1 states was predicted to be 3.36×10^{-5} cm^{-1}, resulting in the negligible FC contribution.

Based on these rate constants, the Φ_F of **P-Thio** was predicted to be 0.96, which was quite in good agreement with the experimentally obtained value at 0.95. This high value comes from the slower intersystem crossings to the more unstable triplet states despite the larger SOCMEs than those of **P-Ben**.

I tried to conduct the single-point calculations at the DLPNO-STEOM-CCSD level; however, I failed to obtain the energy of the T(π-π^*) state with a reasonable % active character. Although the correction increased the rate constant of the radiative decay and other intersystem crossings, the main decay was still predicted to be the radiative decay.

4.3.5 PO-Thio

The geometries at the S_1 state and three triplet states were optimized; however, all of the three triplet states were located at more than 10 kcal/mol higher energy levels. Hence, I

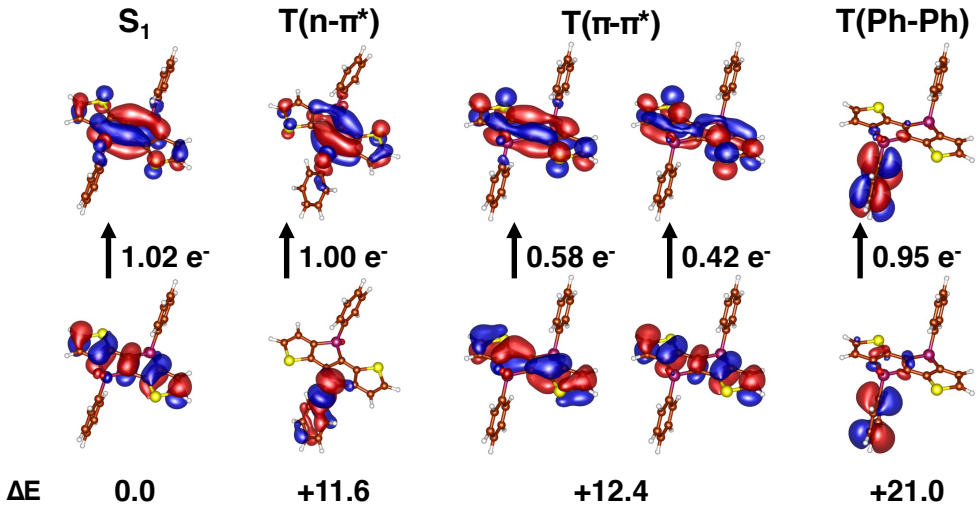

Fig. 4.6: The natural transition orbitals (NTOs) of **PO-Thio** at the optimized geometries. The pictures in the higher line are the unoccupied ones while those in the lower line are the occupied ones. The numbers between each occupied and unoccupied NTOs represent their eigenvalues. The relative energies against the minimum of the S_1 state are given below occupied NTOs.

concluded that transition from S_1 to triplet states do not occur efficiently.

Table 4.5: Comparison of the computationally estimated rate constants with experimentally estimated ones of **PO-Thio** in s^{-1} unit.

	Cal.(PBE0)[a]	Cal.(STEOM)[b]	Exp.[c]
k_r	2.1×10^7	3.0×10^7	4.0×10^7
k_{ic}	1.2×10^8	1.6×10^7	—
k_{nr}	1.2×10^8	1.6×10^7	9.6×10^8
Φ_F	0.14	0.65	0.04

[a] Energies, geometries and Hessians at the TD-PBE0/cc-pVDZ level were employed.
[b] Geometries and Hessians at the TD-PBE0/cc-pVDZ level and energies at the DLPNO-STEOM-CCSD/cc-pVTZ level were employed.
[c] Taken from Ref. 2

I computed the rate constants of the fluorescent decay (k_r), and $S_1 \rightarrow S_0$ internal conversion (k_{ic}). Then, the nonradiative decay rate constant was assumed to be the same as k_{ic}. The estimated rate constants were compared with the experimentally estimated values of the original molecule[2] in Table 4.5, assuming that the TIPS moiety do not affect the rate constants.

The radiative decay rate constant was estimated to be 2.1×10^7 s^{-1}, which was in good agreement with the experimentally obtained value at 4.0×10^7 s^{-1}. Again, the major component was the FC term; radiative decay rate constant at the FC level was estimated to be

2.0×10^7 s^{-1} because this transition is dipole-allowed. The internal conversion rate constant was estimated to be 1.2×10^8 s^{-1}, which was higher than the predicted k_r. Based on these rate constants, the Φ_F was predicted to be 0.14. This estimation may qualitatively reproduce the experimental observation that the Φ_F of **PO-Thio** was much smaller than unity. However, this estimation was sensitive to the Duschinsky rotation; k_{ic} was predicted to be 9.7×10^6 s^{-1} without the Duschinsky rotation.

The correction to the S_1-S_0 adiabatic energy was considered at the DLPNO-STEOM-CCSD level. The adiabatic energy was predicted to be 2.54 eV at this level, which was larger than 2.28 eV at the TD-PBE0 level. This increase in the adiabatic energy slightly increased the predicted k_r, while it decreased the k_{ic} by a factor of 0.13. As a result, the Φ_F was predicted to be 0.65, which was considerably different from the experimental observation. These results may indicate that the small Φ_F of **PO-Thio** may be explained by the high k_{ic}; however, the k_{ic} was so sensitive to the model that this computation might be insufficient.

4.3.6 Comparison among the molecules

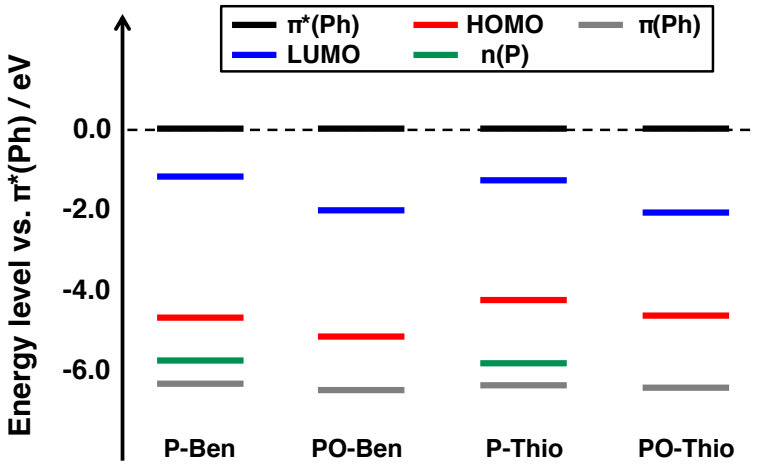

Fig. 4.7: The energy levels of the specific Kohn–Sham orbitals of the molecules in this study. The relative energy levels against the π^* orbital in the phenyl ring at the side of the main skeleton were depicted in eV unit for each molecule. Values were taken from the PBE0/cc-pVDZ level calculation at the optimized S_1 state geometry. The level of the lone pair of phosphorus atoms was not shown for **PO-Ben** nor **PO-Thio** because they do not have any lone pair on the phosphorus atoms.

The computed rate constants indicated that the oxygenation of the phosphorus atoms and the substitution by thiophene rings both increased the Φ_F by decreasing the rate of the intersystem crossing. This decrease was seemingly produced by the loss of the lone pair by oxygenation and destabilized triplet states against the S_1 state.

To analyze the origin of the relative destabilization of the triplet states, the energy levels of the Kohn–Sham orbitals related to the triplet states discussed at the minimum of the S_1 state were collected in Fig. 4.7, where the relative energies against the π^* orbital in the side

phenyl rings were shown by assuming that this MO level was similar among the P-bridged stilbene analogues. The oxygenation of the **P-Ben** to **PO-Ben** effectively stabilized the LUMO energy, as discussed in previous studies.[1,10] This stabilization of the LUMO reduced the HOMO-LUMO gap from 3.53 to 3.16 eV, resulting in the stabilization of the S_1 state. On the other hand, the energy level of the π and π^* orbitals of the phenyl ring in **PO-Ben** were similar to those in **P-Ben**, resulting in a similar energy level of the T(Ph-Ph) state. Therefore, the T(Ph-Ph) state of **PO-Ben** became more unstable against the S_1 state than that of **P-Ben** did.

The effect of the substitution by thiophene rings can be discussed in a similar manner. **P-Thio** as well as **P-Ben** has a lone pair on the phosphorus atoms, and the energy level of the lone pair was comparable. Moreover, the levels of the π and π^* orbitals of the phenyl ring, and LUMO were comparable. On the contrary, the level of HOMO in **P-Thio** was more unstable than **P-Ben**, Hence, the HOMO-LUMO gap decreased from 3.53 to 3.0 eV, resulting in the relative stabilization of the S_1 state in **P-Thio**, Due to the stabilization of the S_1 state, the triplet states of **P-Thio** became more unstable against the S_1 state than that of **P-Ben** did.

Because both of the oxygenation of the phosphorus atom and substitution by the thiophene-fused skeleton stabilized the S_1 state against the triplet states, the triplet states of **PO-Thio** became more unstabler against the S_1 state than **PO-Ben** or **P-Thio** was. From the energy levels of the molecular orbitals, the relative energies of the triplet states against the S_1 state were explained among the four P-bridged stilbene analogues.

4.3.7 Decay of PO-Thio through CI

Because the conducted rate constant calculations did not include the thermally activated decay through the CI, I searched the MECI geometry of the **PO-Thio** at the 3SA-XMS-CASPT2 level. The optimized geometries of the minimum of the S_1 state (S_1min) and S_0-S_1 MECI were compared in Fig. 4.8, and some of the characteristic changes in the internal coordinates were collected in Table 4.6. It turned out to be that **PO-Thio** had an S_1-S_0 MECI which was 3.5 kcal/mol more unstable than the S_1min at the XMS-CASPT2 level employed. While the thiophene-fused skeleton was almost planar at the S_1min, where the dihedral angle of C1-C13-C14-C10 was -180.0°, that at the MECI geometry was far from planar, where the dihedral was -117.3°. Moreover, the bond length of the C13-C14 became longer from 1.413 to 1.565 Å, i.e. elongation of 0.15 Å. Due to these large changes in internal coordinates, this MECI geometry seemed to be characterized as the twisting of the polyene chain assuming that a thiophene ring can be seen as a bridged diene.

To discuss the rate constant of the decay through this MECI using the Eyring's equation,[53] the activation energy to reach it should be estimated. To obtain an upper limit of the activation energy, the PECs along the LIIC between the S_1min and MECI geometry were computed at the 3SA-XMS-CASPT2 and 5SA-XMS-CASPT2 levels. The PECs plotted as a function of the dihedral C1-C13-C14-C10 were shown in Fig. 4.9. The PECs at the 3SA-XMS-

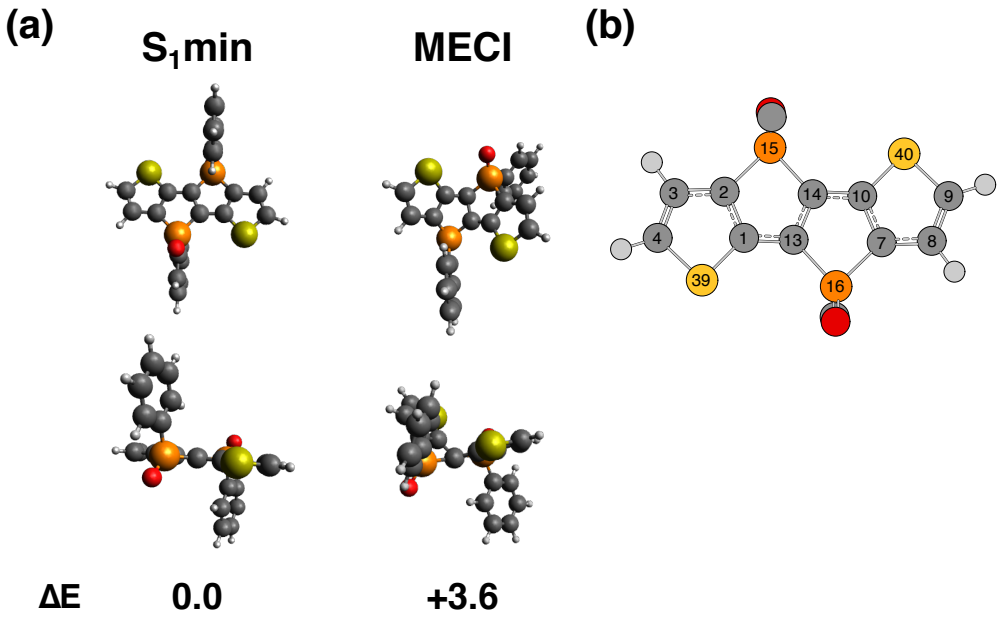

Fig. 4.8: (a)The XMS-CASPT2-level optimized S_1 and S_1-S_0 MECI geometries and (b)atom labeling of **PO-Thio**. The pictures on the upper and lower lines are the top and side views of the geometries. The side view was depicted so that atom 13 overlaps 14. The relative energies at the S_1 state were shown below the pictures. Atom labelings were shown only for the thiophene-fused skeleton, where the labels for hydrogen atoms were omitted.

Table 4.6: Some of the characteristic changes in internal coordinates from the minimum of the S_1 state (S_1min) to the MECI geometry.

Bond				Dihedral angle			
	S_1min	MECI	Δ / Å		S_1min	MECI	Δ / deg
B(1-39)	1.702	1.748	+0.045	D(1,13,14,10)	-180.0	-117.3	+62.7
B(2-15)	1.813	1.857	+0.044	D(7,10,14,13)	-0.8	-24.3	-23.5
B(3-4)	1.367	1.398	+0.031	D(14,13,7,6)	177.9	132.9	-44.9
B(7-10)	1.433	1.472	+0.039	D(13,14,2,15)	-177.9	172.9	-9.3
B(10-40)	1.702	1.754	+0.051				
B(13-14)	1.413	1.565	+0.153				

CASPT2 level were similar to those at the 5SA-XMS-CASPT2 level. While the contraction scheme was changed from the SS-SR to MS-MR, the energy gaps at the MECI geometry were similarly small. These results indicated that the existence of the MECI geometry in this region was not unique to the method employed in the geometry optimization.

The PECs gave the highest energy at the S_1 state in LIIC at the MECI geometry, suggesting that there was no rate-determining transition state in higher energy level than the MECI. The S_1 state at the MECI geometry were predicted to be 4.5 and 5.6 kcal/mol more unstable than the S_1min at the 3SA and 5SA-XMS-CASPT2 levels, respectively; these values were comparable to the one obtained in the geometry optimization at 3.6 kcal/mol. These relative

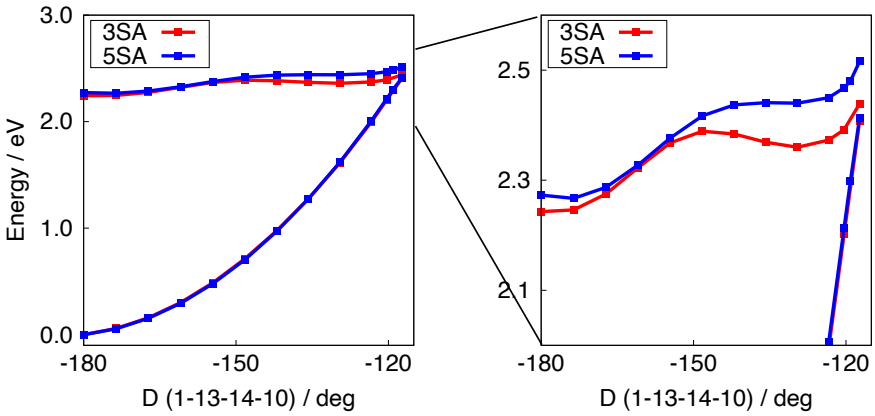

Fig. 4.9: The PECs of the S_0 and S_1 states along the LIIC connecting the S_1min and MECI geometries. The energies were computed at the 3SA- (red) and 5SA-(blue) XMS-CASPT2/cc-pVDZ level. The left figure showed the whole PECs while the right one focused on the S_1 PECs.

energies can be regarded as the activation energy to reach MECI geometry. Suppose that **PO-Thio** must move to the S_0 state when it reaches the MECI geometry, the k_{nr} at 9.6×10^8 s^{-1} implies the activation free energy at 5.2 kcal/mol. Although the activation free energy cannot be estimated from PECs due to the difficulty in obtaining the free energy at the MECI geometry, my prediction of the activation energy seemingly suggested that the decay through this MECI be energetically possible.

Note that both of the S_1 PECs in Fig. 4.9 showed small barrieres. These barriers possibly come from the use of the LIIC. The relaxed scan along this dihedral angle may remove these small barriers.

Then, the electronic states at the S_1min and the CI region were analyzed to gain insight into the character of the CI. To clearly distinguish the ground and excited states at CI region, a geometry near the MECI in the LIIC (n-MECI), where the dihedral 1-13-14-10 was -120.3°, was used for the analysis of the electronic state instead of the MECI geometry itself.

The XMS-CASPT2 rotation matrix indicated that the XMS-CASPT2 S_0 and S_1 states at the S_1min were mainly composed of the CASSCF S_0 and S_2 states, respectively, while those at the n-MECI geometry were mainly composed of the CASSCF S_0 and S_1 states, respectively. The S_0 and S_2 CASSCF natural orbitals at the S_1min were shown in Fig. 4.10 and 4.11, respectively, while the S_0 and S_1 CASSCF natural orbitals at the n-MECI were shown in Fig. 4.12 and 4.13, respectively. The occupation numbers of the natural orbitals at the S_1min indicated that the S_0 state was well described by the closed-shell single determinant, where the occupation numbers are in a range from 0 to 0.25 or that from 1.75 to 2.0, and the S_2 state was well characterized as the HOMO-LUMO transition from the S_0 state. On the contrary, at the n-MECI geometry, the S_0 state was the open-shell singlet state while the S_1 state was almost the closed-shell. The singly occupied S_0 natural orbitals are the bonding and anti-bonding orbitals of the central C-C bond, suggesting the decreased bond order of

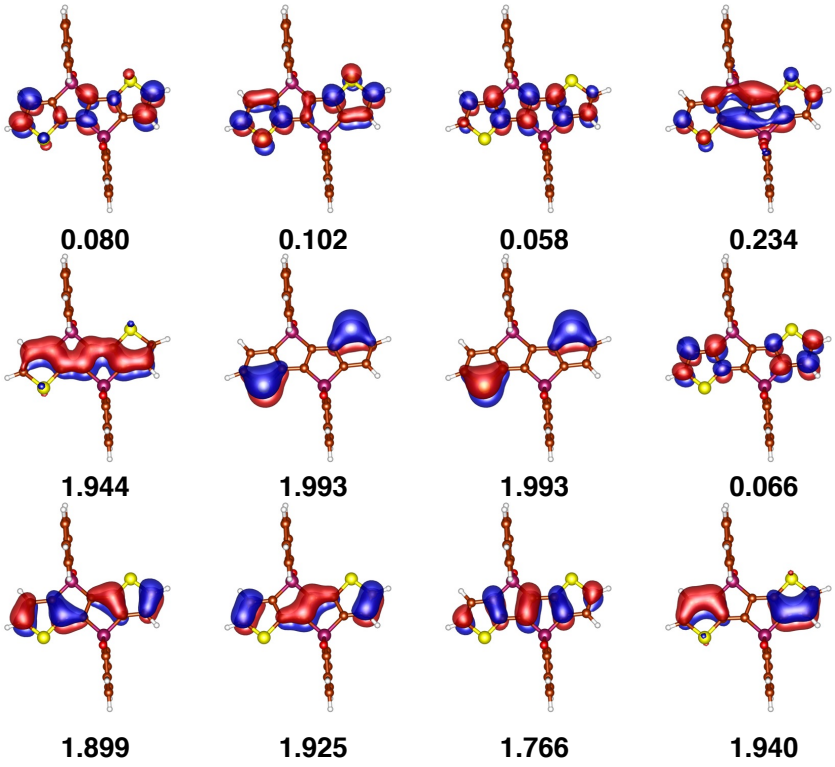

Fig. 4.10: The S_0 CASSCF natural orbitals and their occupation numbers at the S_1min. The orbitals were obtained by the 3SA-CASSCF calculation.

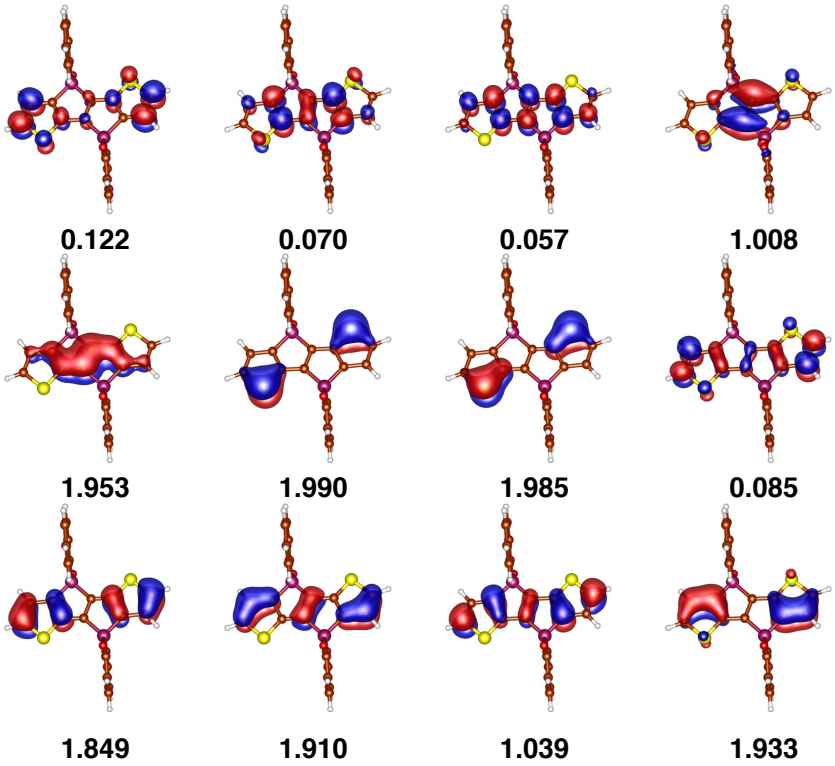

Fig. 4.11: The S_2 CASSCF natural orbitals and their occupation numbers at the S_1min. The orbitals were obtained by the 3SA-CASSCF calculation.

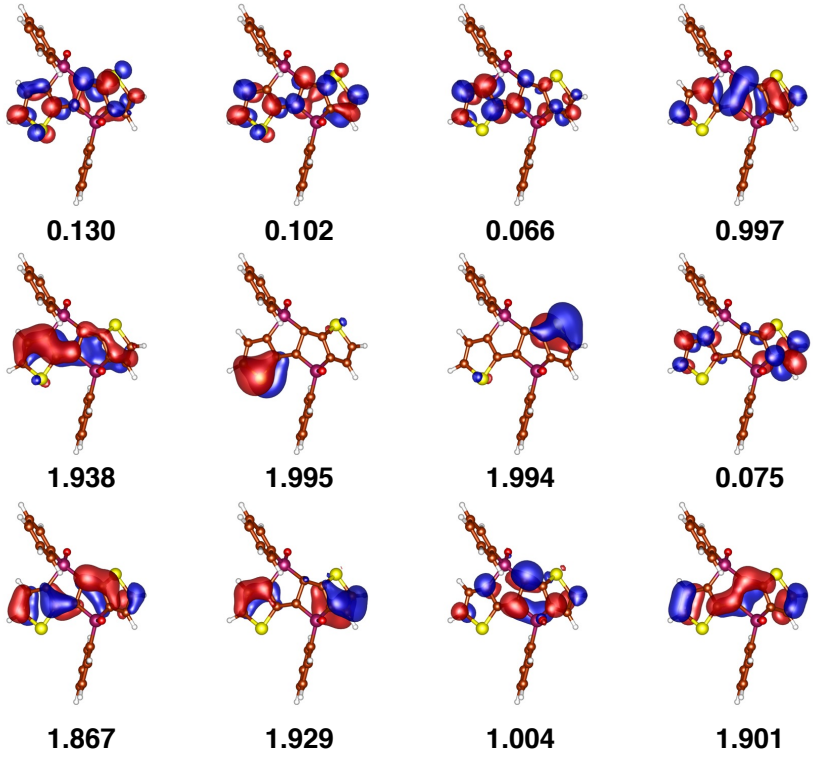

Fig. 4.12: The S_0 CASSCF natural orbitals and their occupation numbers at the n-MECI geometry. The orbitals were obtained by the 3SA-CASSCF calculation.

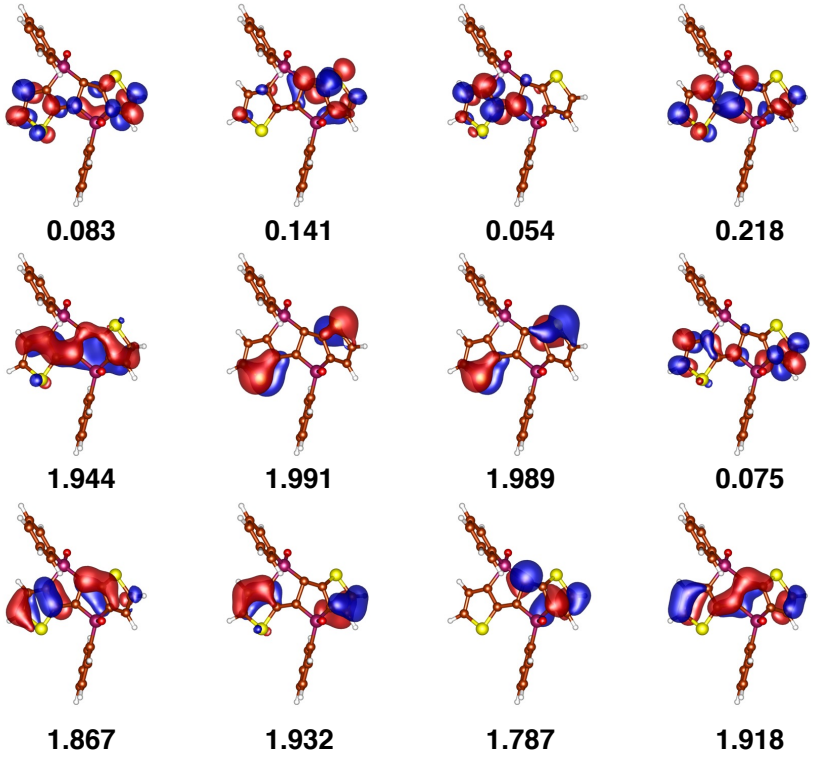

Fig. 4.13: The S_1 CASSCF natural orbitals and their occupation numbers at the n-MECI geometry. The orbitals were obtained by the 3SA-CASSCF calculation.

this bond. The occupation numbers of these orbitals were clearly different in the CASSCF S_1 state; there a closed-shell electronic state was predicted. Note that the excitation of the lone pairs of the sulfur atoms slightly contributed to the electronic states at both of the S_1min and n-MECI geometries.

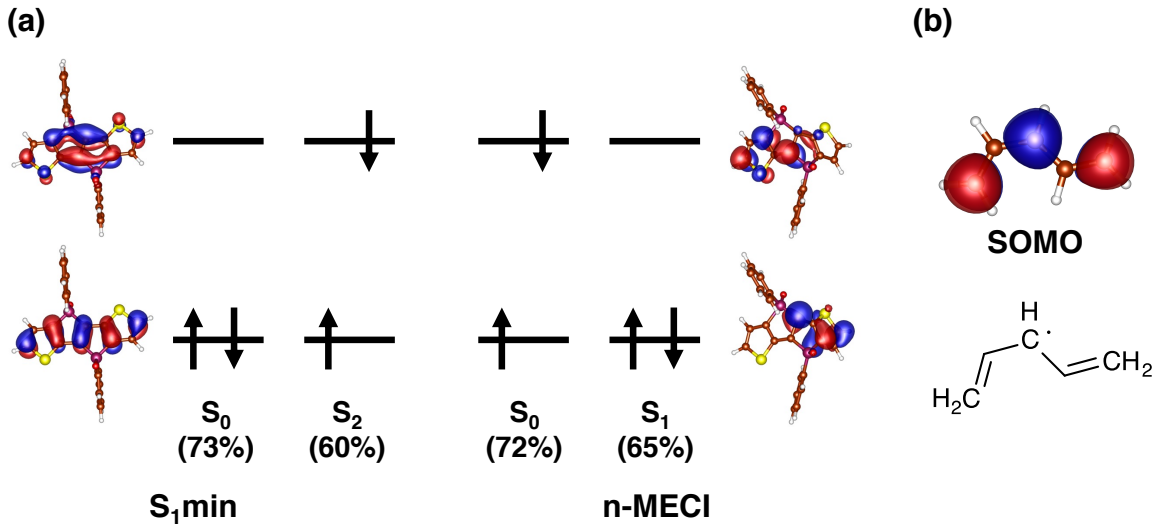

Fig. 4.14: (a)The major determinants in the CASSCF states at the S_1min and n-MECI geometries and (b) SOMO and chemical structure of pentadienyl radical. (a)The weight of the determinant was shown in the parenthesis. The corresponding quasi-canonical orbitals obtained by the 3SA-CASSCF calculations were depicted. (b) SOMO of the pentadienyl radical was computed at the UPBE0/cc-pVDZ level using the optimized geometry.

To qualitatively understand the character of the CI, the major determinant in the CASSCF states and corresponding quasi-canonical orbitals were depicted in Fig. 4.14(a). While the quasi-canonical HOMO and LUMO at the S_1min were delocalized around the thiophene-fused skeleton, those at the n-MECI geometry were localized at the right or left side of the skeleton. In addition, the HOMO and LUMO at the n-MECI geometry were quite similar to the SOMO of the pentadienyl radical in Fig. 4.14(b). This implied that at the n-MECI geometry the S_0 state was composed of two pentadienyl radicals while the S_1 state was separated into the pentadienyl cation and its anion, forming a zwitter-ionic state. This separation of the quasi-canonical HOMO and LUMO on the thiophene-fuzed skeleton was considered to be one of the elements to give a CI, as discussed by Nakai et al.[54]

Moreover, the pentadienyl anion at the right side of the skeleton was seemingly stabilized by the electron-withdrawing phosphole-oxide group. Actually, 3SA-XMS-CASPT2 calculation suggested that the removal of the two O atoms at the n-MECI geometry increased the S_0-S_1 gap from 0.19 to 0.93 eV, implying the stabilization of the zwitter-ionic S_1 state by the phosphole-oxide groups. This stabilization of the S_1 state might be one of the reasons to give a relatively small energy to reach the MECI point.

4.4 Conclusions

In this chapter, a comparative study of the decays from the S_1 state in the P-bridged stilbene analogues was presented. I computed the rate constants for the transitions from the S_1 state in the P-bridged stilbene analogues using the perturbative approach to gain some insight into the effect of the oxygenation of the phosphorus atom on the photophysical properties. The TD-PBE0 calculations reasonably estimated the absorption and fluorescence energies of the **P-Ben**, **PO-Ben**, **P-Thio**, and **PO-Thio** molecules. The fluorescence of these molecules was characterized as the dipole-allowed LUMO-HOMO transition. My calculations reasonably reproduced the radiative decay rate constants, where the Franck–Condon terms were dominant.

My calculations qualitatively reproduced the low fluorescence quantum yield of **P-Ben**; there the intersystem crossings to the two triplet states, which were characterized by the n(P)-π^* and π(Ph)-π^*(Ph) transitions, respectively, were predicted to be effective. These triplet states were predicted to be stabler than the S_1 state in the case of **P-Ben**.

By oxidizing the phosphorus atom to produce **PO-Ben**, the lone pair to reach the n-π^* type triplet states vanished, resulting in the suppression of the intersystem crossing to that state. At the same time, another triplet state with an effective intersystem crossing in **P-Ben** became more unstable than the S_1 state, resulting in the suppressed intersystem crossing. Hence, the experimentally obtained high fluorescence quantum yield of **PO-Ben** can be explained by the suppression of the intersystem crossings which were effective in **P-Ben**.

The previous experimental study showed that the substitution of the stilbene skeleton in **P-Ben** into the thiophene-fuzed skeleton to produce **P-Thio** raised the fluorescence quantum yield to 0.95. My calculations suggested that the destabilization of the triplet states lowered the rate constant of the intersystem crossings which were effective in **P-Ben**, although the SOCMEs to enable that were larger than it.

On the contrary to the oxygenation of **P-Ben** into **PO-Ben**, that of **P-Thio** into **PO-Thio** was experimentally shown to reduce the fluorescence quantum yield. My calculations predicted that the intersystem crossings were ineffective due to the higher energy level of the triplet states against the S_1 state; instead, $S_1 \rightarrow S_0$ internal conversion might be effective.

The relative energies of the triplet states against the S_1 state were discussed using the energy levels of the Kohn–Sham molecular orbitals. By checking which orbital was stabilized/destabilized by the substitution, the relative destabilization of the triplet states against the S_1 state was explained.

Because the computed internal conversion rate constant was sensitive to the model of PESs, I tried to optimize the minimal energy conical intersection geometry. Optimization at the 3SA-XMS-CASPT2 level suggested that **PO-Thio** had a MECI geometry which was 3.6 kcal/mol more unstable than the minimum of the S_1 state. The optimized MECI geometry had a largely elongated central C-C bond and largely distorted dihedral, implying the break of the π-conjugated system by the twist at the central C-C bond.

The PECs along the LIIC connecting the S_1min and MECI geometries were computed at the XMS-CASPT2 level using the MS-MR contraction scheme to discuss the activation energy to reach the MECI geometry. It turned out to be that there was no rate-determining transition state in the S_1 state PEC, suggesting that the activation energy was given as the relative energy of the MECI against the S_1min. The predicted relative energies were reasonable to the experimentally predicted activation free energy at 5.2 kcal/mol, although the correction from energy to the Gibbs free energy was not considered.

In the CI region, the S_0 and S_1 states were characterized as the open-shell and closed-shell electronic structures, respectively. The closed-shell S_1 state contained the zwitter-ionic character, where the anion on the right was seemingly stabilized by the electron-withdrawing phosphole-oxide group.

Through these computations, I comparatively studied the difference in the fluorescence quantum yield of the P-bridged stilbene analogues. While the major nonradiative decay pathway in **P-Ben** was predicted to be the intersystem crossing, that in **PO-Thio** was predicted to be the internal conversion via conical intersection. This finding might give a clue to control the nonradiative decays in phosphorus-containing π-conjugated molecules.

Bibliography

[1] A. Fukazawa et al., Org. Lett. **10**, 913 (2008).

[2] A. Fukazawa, T. Murai, L. Li, Y. Chen, and S. Yamaguchi, C. R. Chim. **13**, 1082 (2010).

[3] C. Wang et al., Angew. Chem. Int. Ed. **127**, 15428 (2015).

[4] A. Fukazawa et al., Chem. Commun. **52**, 1120 (2016).

[5] M. Grzybowski, M. Taki, and S. Yamaguchi, Chem. Eur. J. **23**, 13028 (2017).

[6] C. Wang et al., J. Am. Chem. Soc. **139**, 10374 (2017).

[7] C. Wang et al., Chem.–Asian J. **13**, 1616 (2018).

[8] Y. Sugihara et al., Chem. Sci. **12**, 6333 (2021).

[9] J. Lee, N. Aizawa, and T. Yasuda, J. Mater. Chem. C **6**, 3578 (2018).

[10] Y. Matano and H. Imahori, Organic & biomolecular chemistry **7**, 1258 (2009).

[11] F. Santoro, A. Lami, R. Improta, J. Bloino, and V. Barone, J. Chem. Phys. **128**, 224311 (2008).

[12] V. Barone, J. Bloino, M. Biczysko, and F. Santoro, J. Chem. Theory Comput. **5**, 540 (2009).

[13] J. Cerezo, J. Zuniga, A. Requena, F. J. Avila Ferrer, and F. Santoro, J. Chem. Theory Comput. **9**, 4947 (2013).

[14] J. Cerezo and F. Santoro, J. Chem. Theory Comput. **12**, 4970 (2016).

[15] A. Baiardi, J. Bloino, and V. Barone, J. Chem. Theory Comput. **9**, 4097 (2013).

[16] A. Baiardi, J. Bloino, and V. Barone, J. Chem. Phys. **144**, 084114 (2016).

[17] A. Humeniuk et al., J. Chem. Phys. **152**, 054107 (2020).

[18] Q. Peng, Y. Yi, Z. Shuai, and J. Shao, J. Chem. Phys. **126**, 114302 (2007).

[19] Y. Niu, Q. Peng, and Z. Shuai, Sci. China Ser. B-Chem. **51**, 1153 (2008).

[20] Y. Niu, Q. Peng, C. Deng, X. Gao, and Z. Shuai, J. Phys. Chem. A **114**, 7817 (2010).

[21] Q. Peng, Y. Niu, Q. Shi, X. Gao, and Z. Shuai, J. Chem. Theory Comput. **9**, 1132 (2013).

[22] I. Kim et al., J. Chem. Theory Comput. **16**, 621 (2020).

[23] I. Kim et al., JACS Au **1**, 987 (2020).

[24] M. Etinski, J. Tatchen, and C. M. Marian, J. Chem. Phys. **134**, 154105 (2011).

[25] M. Etinski, V. Rai-Constapel, and C. M. Marian, J. Chem. Phys. **140**, 114104 (2014).

[26] T. J. Penfold, E. Gindensperger, C. Daniel, and C. M. Marian, Chem. Rev. **118**, 6975 (2018).

[27] F. Neese, F. Wennmohs, U. Becker, and C. Riplinger, J. Chem. Phys. **152**, 224108 (2020).

[28] *FCclasses 3.0 beta release*, http://www.pi.iccom.cnr.it/fcclasses.

[29] C. Adamo and V. Barone, J. Chem. Phys. **110**, 6158 (1999).

[30] T. H. Dunning Jr, J. Chem. Phys. **90**, 1007 (1989).

[31] D. E. Woon and T. H. Dunning Jr, J. Chem. Phys. **98**, 1358 (1993).

[32] F. Weigend and R. Ahlrichs, Phys. Chem. Chem. Phys. **7**, 3297 (2005).

[33] E. v. Van Lenthe, J. Snijders, and E. Baerends, J. Chem. Phys. **105**, 6505 (1996).

[34] C. van Wüllen, J. Chem. Phys. **109**, 392 (1998).

[35] F. Neese, J. Chem. Phys. **122**, 034107 (2005).

[36] F. Weigend, Phys. Chem. Chem. Phys. **8**, 1057 (2006).

[37] F. Neese, F. Wennmohs, A. Hansen, and U. Becker, Chem. Phys. **356**, 98 (2009).

[38] C. Riplinger and F. Neese, J. Chem. Phys. **138**, 034106 (2013).

[39] R. Berraud-Pache, F. Neese, G. Bistoni, and R. Izsák, J. Chem. Theory Comput. **16**, 564 (2019).

[40] R. Izsák, Int. J. Quantum Chem. **121**, e26327 (2021).

[41] M. J. Frisch et al., Gaussian 16 Revision B.01, 2016, Gaussian Inc. Wallingford CT.

[42] F. Duschinsky, Acta Physicochim. URSS **7**, 551 (1937).

[43] V. Bakken and T. Helgaker, J. Chem. Phys. **117**, 9160 (2002).

[44] D. G. A. Smith et al., J. Chem. Phys. **152**, 184108 (2020).

[45] T. Shiozaki, W. Győrffy, P. Celani, and H.-J. Werner, J. Chem. Phys. **135**, 081106 (2011).

[46] N. Forsberg and P.-Å. Malmqvist, Chem. Phys. Lett. **274**, 196 (1997).

[47] J. W. Park, R. Al-Saadon, N. E. Strand, and T. Shiozaki, J. Chem. Theory Comput. **15**, 4088 (2019).

[48] G. Ghigo, B. O. Roos, and P.-Å. Malmqvist, Chem. Phys. Lett. **396**, 142 (2004).

[49] J. W. Park and T. Shiozaki, J. Chem. Theory Comput. **13**, 2561 (2017).

[50] J. W. Park, J. Chem. Theory Comput. **17**, 6122 (2021).

[51] *QSimulate-QM. Quantum Simulation Technologies, Inc. 2020*, https://qsimulate.com/.

[52] R. L. Martin, J. Chem. Phys. **118**, 4775 (2003).

[53] H. Eyring, J. Chem. Phys. **3**, 107 (1935).

[54] H. Nakai, M. Inamori, Y. Ikabata, and Q. Wang, J. Phys. Chem. A **122**, 8905 (2018).

Chapter 5

Concluding Remarks

Herein, my investigations into the decay processes in the photo-excited organic dye molecules were summarized. As a technological aspect, I employed two methods; the one is derived by the perturbation to the time-dependent Schrödinger equation, and the other is Eyring's equation using the activation energy to reach a conical intersection (CI) point at the excited state PES. To employ the perturbative method, I developed a computer implementation related to FCClasses 3.0, which was kindly provided by Santoro, as a reference code. Calculations using high-level wavefunction theory or multireference quasi-degenerate perturbation theory (MR-QDPT) play important roles in adequately describing the complicated electronic state around the CI. This is particularly pronounced when optimizing the geometries as well as evaluating the energies at the given geometry. The geometric search of the CI requires a distinguishing projection method. These theories were summarized in Chapter 2, where illustrative comparisons of the computational results with the references and application to the characteristic thermally activated delayed fluorescence (TADF) molecules are shown. The application to the TADF molecule demonstrated that a reliable estimation of the adiabatic energy as well as the treatment of the spin-orbit coupling matrix elements (SOCMEs) at the higher level than the Franck–Condon level is essential for reliably estimating the rate constant of the reverse intersystem crossing (rISC).

In Chapter 3, an investigation of the thermally activated decay through the CI in silepin molecules was presented. The use of the MR-QDPT calculations enabled to handle the gradual change in the complicated electronic structure from the minimum of the S_1 state (S_1min) to the minimal energy CI (MECI) geometry. This reasonable description of the electronic states predicted the existence of the activation barrier in the reaction path. The XMS-CASPT2 level optimization of the transition state as well as the S_1min and MECI geometries for the small silepin resulted in the reasonable estimation of the activation free energy. This study indicated that the geometry optimizations and energy evaluations at the MR-QDPT level may give a reasonable description of the energetics in the thermally activated decay through the CI for organic dye molecules.

In Chapter 4, a comparative study of the decays from the S_1 state in the P-bridged stilbene analogues was presented. By computing the rate constants of the transitions from the S_1 state using the Python code I wrote, the fluorescence quantum yields Φ_F of these molecules were

qualitatively reproduced. The low Φ_F of the bis-phosphanyl-bridged stilbene (**P-Ben**) was explained by the effective intersystem crossings to the two triplet states; there, one of them was characterized by the n(P)-π^* transition and the other was by the π-π^* transition in the phenyl rings at the side of the stilbene skeleton. The oxygenation of **P-Ben** to form **PO-Ben** decreased the rate constant of the intersystem crossing by removing the lone pair on the phosphorus atom and stabilizing the S_1 state. The substitution of the stilbene skeleton in **P-Ben** into thiophene-fused skeleton to form **P-Thio** also decreased the rate constant of the intersystem crossing by stabilizing the S_1 state. Conducting both of the oxygenation and introduction of the thiophene-fuzed skeleton to **P-Ben** to form **PO-Thio** similarly decreased the rate constant of the intersystem crossing; however, internal conversion was accelerated instead. While the suppression of the intersystem crossings was explained by the energy levels of the Kohn-Sham orbitals, the $S_1 \rightarrow S_0$ internal conversion in **PO-Thio** was explained by the decay through CI. The XMS-CASPT2 level geometry optimizations suggested that **PO-Thio** had a MECI geometry at 3.6 kcal/mol higher energy level than the minimum of the S_1 state. This CI was described as the separation of the π-conjugation in the thiophene-fused skeleton by the twisting of the central C-C bond, where the electron-withdrawing phosphole-oxide group seemingly stabilized the zwitter-ionic S_1 state. A comparative study was achieved using the perturbative method and MECI optimization at the MR-QDPT level.

Through the studies in Yanai group, I got a part of the skill to investigate the decay processes of the organic dye molecules. The understanding and my Python code are potentially useful for studying those processes in the future in Yanai group. For example, the geometry, Hessian, and coupling terms at the higher-level quantum mechanical methods can be applied by using my Python code. Because the computation of the derivatives of the SOCMEs was computationally demanding, the development of their analytical gradient should effectively accelerate the use of this method. The extension of my code is also possible. Implementation of the reduced-dimension scheme by Barone et al. should be useful to analyze the effect of the specific vibrational mode. The SOCMEs at the FCHT level might be applied to the intersystem crossing rate constant calculations derived from the 2nd-order perturbation theory. Furthermore, application to other characteristic molecules should be also an interesting topic. When some fast nonradiative decays disturb the application of the molecule, detection of the pathways using these methods may give a clue to suppress the decays. Theoretical prediction of molecules with efficient TADF may be possible by theoretically determining the factors to accelerate the rISC, as is already tackled by other groups. I hope we can gain further insight into the molecular design of the functional organic dye molecules through the theoretical investigations of their decay processes in the future.

Acknowledgements

I would like to express my gratitude to my supervisor Professor Takeshi Yanai for his lots of help in a wide range in my three years. I would like to express my appreciation to Associate Professor Kazuhiro J. Fujimoto and Assistant Professor Masaaki Saitow for fruitful discussions in our seminars. I also express my appreciation to my previous supervisor Associate Professor Daisuke Yokogawa for discussions and suggestions in collaborative research. I thank current and former members of Yanai group for their help and discussions in my daily life. I would like to thank Professor Shigehiro Yamaguchi, Ms. Mika Sakai, and Mr. Yoshiaki Sugihara for interesting discussions about the excited-state dynamics and related collaborative reserches. I thank Professor Aiko Fukazawa, Professor Hiroshi Miyasaka, Assistant Professor Hikaru Sotome, Professor Hiroshi Shinokubo, and Ms. Asahi Takiguchi for collaborative researches. I thank Dr. Yukihiro Okuno, my double-mentor in GTR program, and Mr. Atsuro Nomoto for discussions about researches and related collaborative researches.

I thank Dr. Toru Shiozaki and Assistant Professor Jae Woo Park for technical support for conducting geometry optimization at the XMS-CASPT2 level using BAGEL program. I thank Dr. Fabrizio Santoro and Professor Jefferey R. Reimers for providing me with source codes of their programs, which were used for writing my Python code as a reference.

I thank the staff and members of the "Graduate Program of Transformative Chem-Bio Research" at Nagoya University, supported by MEXT (WISE Program) for financial supports and exciting events. Finally, I express my gratitude to members of my family for their supports in daily life.

List of Publications

Subpaper

[1] N. Inai, D. Yokogawa, and T. Yanai, J. Phys. Chem. A **125**, 559 (2021).

Other publications

[1] Y. Sugihara, N. Inai, M. Taki, T. Baumgartner, R. Kawakami, T. Saitou, T. Imamura, T. Yanai, S. Yamaguchi, Chem. Sci. **12**, 6333 (2021).

[2] A. Nomoto, N. Inai, T. Yanai, Y. Okuno, J. Phys. Chem. A, *in press.*

[3] A. Fukazawa, N. Kimura, C. Wang, M. Hayakawa, H. Sotome, H. Miyasaka, N. Inai, D. Yokogawa, S. Yamaguchi, *manuscript in preparation.*

[4] A. Takiguchi, N. Inai, S. Kang, M. Hagai, S. Lee, T. Yanai, D. Kim, H. Shinokubo, *submitted.*